Power Oscillation Damping Using Expandable VSC-HVDC Transmission System

10th sem. project
Group PED4-1046
Energy engineering
Aalborg University
June 1st 2018

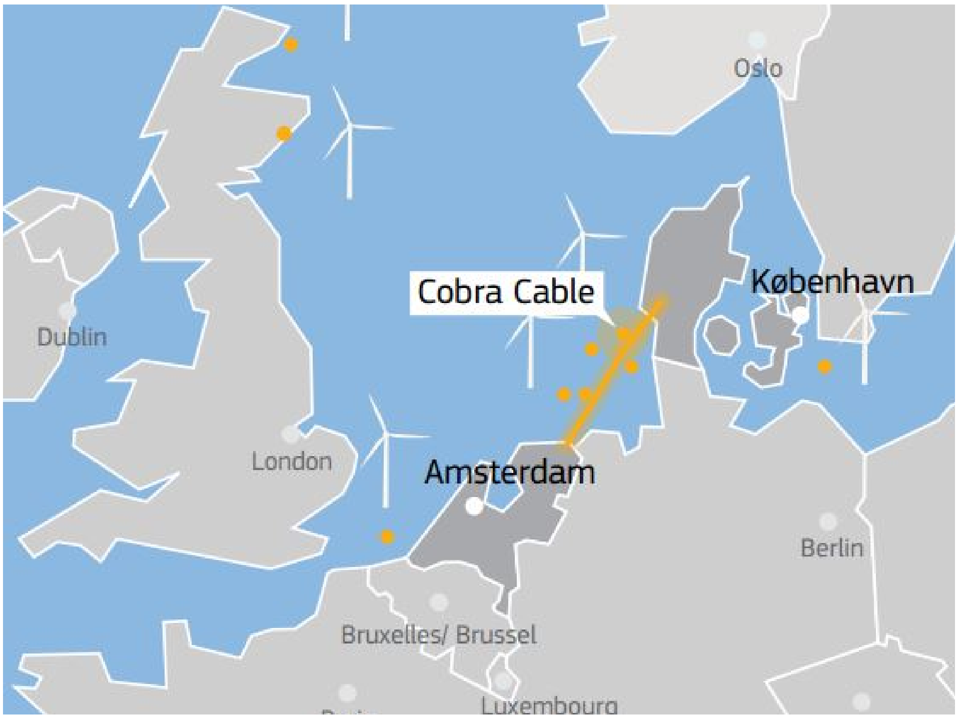

The School of Engineering and Science
Study Board of Energy Engineering
Sohngårdsholmsvej 57, 9000 Aalborg
Phone 96 35 80 80
Fax 98 14 25 55
http://www.bsn.aau.dk

AALBORG UNIVERSITY
STUDENT REPORT

Title:

Power Oscillation Damping Using Expandable VSC-HVDC Transmission System

Project:

10th semester

Project period:

February 2018 - June 2018

Project group:

PED4-1046

Participants:

Hun Heo
Ioannis Mexis

Supervisors:

Filipe Faria da Silva
Roni Irnawan

Report pages: 59
Appendix pages: 5
Completed: 01-06-2018

Synopsis:

This thesis refers to the expansion of the COBRAcable by adding an offshore wind farm converter into the existing point–to–point HVDC link, as envisioned by Cigre. The focus is placed on the examination of the influence of the added terminal into the existing power oscillation damping control function and the tuning of the latter for the expanded three–terminal system. Initially, a simple two–area AC system modelled in DIgSILENT PowerFactory is utilized in order to excite inter–area oscillations in it. The HVDC system is modelled as a half-bridge modular multilevel converter based voltage-sourced converter system. The POD control function is added on top of the converters' main control configuration and the HVDC link is connected to the AC system. The latter is subjected to a disturbance and the POD performance is assessed. Subsequently, the additional offshore terminal is added to the existing PtP configuration with the onshore converters operating under two different control modes, i.e. master–slave and DC voltage droop control mode and its influence into the POD function is examined by varying the output power profiles of the wind farm. Finally, the output of the POD controller is compensated with the aim of improving the damping performance when the converters operate in DC voltage droop control mode.

Preface

This report is composed by a group of 10th semester students at Aalborg University as a part of the master programme in Power Electronics and Drives. The theme of the project is *Power Oscillation Damping Using Expandable VSC-HVDC Transmission System*.

Prerequisites for reading the report is basic knowledge regarding Power Systems, Power Electronics and Control Theory.

The project group would like to address great thanks to the supervisors of the project. Thanks is given to Filipe Faria da Silva for inspiring supervision and constructive criticism during the project period.

Reading guide

Through the report source references in the form of the IEEE method will appear and these are all listed at the back of the report.

Figures and tables in the report are numbered according to the respective chapter. In this way the first figure in chapter 3 has number 3.1, the second number 3.2 and so on. Explanatory text is found under the given figures and tables. Figures without references are composed by the project group.

Ioannis Mexis

Hun Heo

Table of contents

ABBREVIATIONS

AC .... Alternating Current

ASM .... Asynchronous Machine

DC .... Direct Current

HVDC .... High Voltage Direct Current

LCC .... Line Commutated Converter

MMC .... Modular Multilevel Converter

MTDC .... Multiterminal Direct Current

PI .... Proportional–Integral

PLL .... Phase–Locked Loop

POD .... Power Oscillation Damping

PSS .... Power System Stabilizer

PtP .... Point–to–Point

PWM .... Pulse Width Modulation

VSC .... Voltage Source Converter

XLPE .... Extruded cross-linked polyethylene

1 Introduction

In today's era, HVDC transmission is a widely recognized and well-established technology used for long-distance bulk power transmission, offering a potential for connecting the renewable generation sources to the traditional load centers which are located far from them. Under certain circumstances, HVDC systems present a series of advantages cormpared to their AC counterparts in terms of technical, economic and environmental aspects. Among the most important are the lower total investment and fewer losses over a break–even distance as well as the increased controllability.

At present, the majority of HVDC transmissions are point–to–point schemes, i.e. they comprise of two terminals. Nevertheless, multiterminal HVDC grids are expected to be built in the future since they allow improved energy trading, integration of renewable energy sources such as distant offshore wind farms and potential for increased system stability. For the realization of such grids, VSC–HVDC systems are more favorable compared to their more established LCC–HVDC counterparts. More specifically, the polarity of the DC voltage has to be reversed in LCCs in order to reverse the power flow, whereas the latter can be achieved by reversing the current flow in VSCs, thus resulting in faster power control. Moreover, since the converters can reverse the direction of the power flow without the inversion of the voltage polarity, the problem of a decrease in insulation performance such as space charge influences, can be reduced and thus light weight and economical cross–linked polyethylene (XLPE) cables can be used [1]. Additional advantages of VSCs over LCCs are [2]:

- The independent control of active and reactive power.
- The less strict requirements of short–circuit ratio (SCR) for the AC system to which they are connected. The use of VSC technology enables the control of reactive power and hence the control of the grid voltage. In other words, VSCs can be connected to weak grids, i.e. grids with low SCR, since they are able to support the voltage.
- The forced commutation which allows black start.
- The smaller converter station footprint.

An additional feature of HVDC systems is that they can be utilized for damping power oscillations. Since they can be connected in parallel with long distance onshore AC transmission corridors, they can affect the power system modes. These modes refer to frequencies in which oscillations appear in a power system when the latter is subjected to a disturbance. They can be obtained by applying small–signal analysis to a power system model which can be done faster with the use of modern power system simulation softwares. Therefore, having linearized the model around its operating point, its eigenvalues can be plotted and thus the information about the frequency and the damping of the oscillations can be obtained from the imaginary and real part of the eigenvalues respectively. By adding a supplementary level of control to the main converters' control level, the active power of the VSC–HVDC terminals can be modulated resulting in damping the inter–area electromechanical oscillations, as will be explained below. Regarding the fundamental nature of these types of oscillations, they are caused by inadequate damping of the system's oscillatory modes when the latter experiences a transient event. The inadequate damping torque of a generator's rotor results in oscillations of active power flow. The oscillations are inherent to electric power systems with their frequencies ranging from 0.1 to 2 Hz. They can be categorized based on the system components that they affect. More specifically, the different types are presented below [3]:

- Intraplant mode oscillations: Machines on the same power generation site oscillate against each other at frequencies from 2 to 3 Hz.
- Local plant mode oscillations: A single generator swings against the rest of the system at 1 to 2 Hz.
- Control mode oscillations: These include instability of modes associated with controls of generator excitation systems, HVDC converters and static var compensators. The insufficient tuning of the control systems is the cause of such oscillations.
- Torsional modes: They appear due to the interaction of the aforementioned controls with the dynamics of the turbine–generator shaft system at 10 to 46 Hz.
- Interarea mode oscillations: These oscillations occur between a group of generators in one area swinging against a group of generators in another area of the power system with a frequency range from 0.1 to 0.8 Hz.

The latter ones are affected by a series of factors which include the system structure, the operating conditions, the excitation systems, the type of loads and the DC links [4]. Moreover, they can have very negative consequences on the large interconnected systems such as instabilities, cascading events and system blackouts [5]. The traditional power system stabilizers (PSS) can be utilized in order to achieve satisfactory damping of these kind of oscillations from a generator's point of view. Alternatively, supplementary power oscillation damping (POD) controllers can be added to the main VSC–HVDC control level in order to damp the inter–area oscillations from inter–area transmission point of view. The most common approach for designing the POD controller follows that of a conventional power system stabilizer (PSS), as it will be explained later. It has been previously integrated in PtP HVDC systems in order to modify their active power reference and has been proved to provide effective damping of the inter–area oscillations [5], [6].

In addition to the control in steady–state conditions, HVDC systems often include auxiliary control functions such as frequency control, emergency power control and power modulation control. Regarding the latter, HVDC systems are required to work together with the auxiliary control function of POD which is to modulate the transferred power through the HVDC link typically in the range of 0.8 to 5 Hz in order to provide damping to low frequency power oscillations appeared in the interconnected AC systems [7]. However, there is still room for further research regarding the applications of the POD controllers in multiterminal DC (MTDC) systems, since the expansion of the PtP systems creates challenges in the design and tuning of the POD function. For example, when a PtP system is to be connected to an offshore wind terminal, as it is expected to be the case in North

Sea within the next years, the effect of the different output power profiles of the offshore wind turbines on the power oscillation damping effectiveness has to be investigated. More specifically, conclusions regarding the damping of the oscillations can be drawn by varying the control modes of the onshore converters as well as the number of POD controllers applied to them (either in one of the onshore converters or in both of them) for each wind turbine production pattern. The examination of the wind power production influence on the POD capability and the proposal of a new way of tuning the POD function are included within the scope of this thesis work.

1.1 Project background and problem formulation

In the context of this project, the feasibility of expanding the existing point-to-point (PtP) HVDC link between Denmark and Netherlands in the North Sea region into a multi-terminal HVDC (MTDC) transmission system is examined. This could be implemented in two ways, i.e. by adding a new converter into the existing link or by interconnecting neighbouring HVDC links. A possible solution is to tie–in an offshore wind farm converter to the existing COBRAcable. Since the current configuration incorporates parallel long distance onshore AC transmission corridors, it could be an effective solution for Power Oscillation Damping (POD) within the Continental Europe area. These oscillations are very unlikely to happen within the European power systems since the grids are interconnected by strong AC interties which are not heavily loaded as in case of e.g. the North American systems. However, the expandability of COBRAcable into an MTDC system could introduce challenges in terms of the control design and tuning of the existing POD function from PtP configuration.

The main objectives within this thesis work include:

- The development of the PtP as well as MTDC VSC-HVDC models.
- The implementation and tuning of the POD control function for the PtP configuration.
- The examination of the influence of the added offshore converter to the POD control strategy.
- The proposal of a new way of tuning the POD controller for the expanded system in order to damp the power oscillations effectively, depending on the output power profile of the wind turbines.

1.2 Limitations

The main limitations and simplifications made in the context of this thesis are presented below:

- Lower level controls are not implemented since the focus of the thesis is put on the study of slow transient (electromechanical) phenomena.
- Radial configuration is implemented for the three–terminal HVDC system while ring topology is not considered within the context of this study.
- Variations for the tie–in point of the offshore wind farm converter to the existing HVDC PtP cable are not considered.

- The modelling of the wind farm was simplified representing its operation through the use of an aggregated ASM model, consisting of 100 asynchronous machines in parallel.
- The power oscillations were arised by the introduction of a three–phase symmetrical short–circuit whereas no other kinds of fault situations were studied, e.g. asymmetrical faults.
- In order to simulate the cases under study, a simplified version of the power system was used. A more realistic modelling of the power system with the use of more generators and buses introduces more challenges, e.g. the choice of the input signal for the POD controller is not straightforward but has to be done according to observability criteria [8].

1.3 Thesis outline

Initially, a simple two–area AC test system used in the context of this thesis is simulated in DIgSILENT PowerFactory. Modal analysis is performed in order to record the locations of the eigenvalues associated with the inter–area modes. The system is perturbed by means of a symmetrical three–phase short–circuit which is introduced in one of the test system lines with the aim of observing the resulting inter–area oscillations by means of nonlinear time–domain simulations.

An existing example model of PowerFactory, consisting of an HVDC system which connects an offshore wind farm to the onshore grid, is modified appropriately in order to end up with a PtP VSC–HVDC link connecting two onshore terminals. The model is properly tuned in order to ensure its stable operation. Additionaly, the POD controller scheme is added into the main control strategy of the VSC–HVDC system and the latter is integrated into the AC system. Modal analysis followed by time-domain simulations are realized with the aim of testing the effectiveness of the POD controller into damping the inter-area oscillations.

Subsequently, the PtP link is expanded into a three-terminal network with the addition of an offshore wind farm converter terminal. The wind farm is modelled using an aggregated asynchronous machine model, consisting of 100 machines connected in parallel. The influence of the offshore wind terminal to the existing POD control behaviour is examined by varying the active power output of the machines. Finally, a new way of POD control tuning for the expanded MTDC system is proposed.

PtP VSC–HVDC system 2

This chapter gives a brief overview of the components constituting a typical VSC–HVDC system and its control structure. The modeling of the HVDC link and the tuning of the converters' controllers with the use of PowerFactory are presented. Finally, the implementation of the supplementary POD controller is provided.

2.1 Components of a VSC–HVDC station

Within this section the main components of a VSC–HVDC station are listed and their operating purpose is briefly explained. Figure 2.1 illustrates the configuration of a common VSC–HVDC system comprising of two terminals.

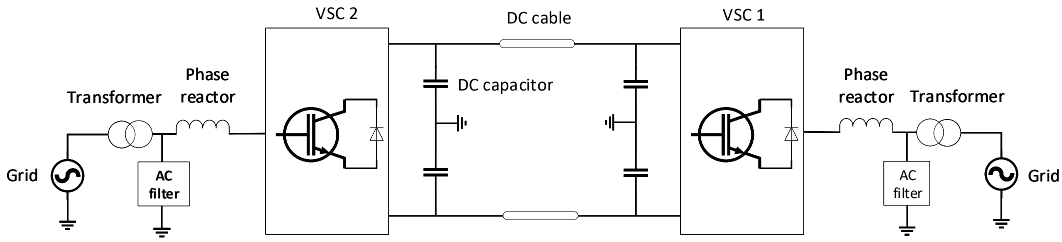

Figure 2.1. Typical configuration of a point–to–point VSC–HVDC system.

The main components of this topology include the converter, the interface transformer, the phase reactor, the AC filter, the DC capacitor and the DC line. A brief description of each component follows.

Converter

The converter is the core component of the VSC–HVDC system and it is controlled via a pulse–width modulation(PWM) technique in order to output an AC voltage of desired magnitude and frequency. It can be operated either in rectifier or inverter mode. Among the different types of voltage–source converters, the modular multilevel converters (MMC) are becoming nowdays attractive for applications such as VSC–HVDC schemes and FACTS due to their inherent advantages, i.e. the built–in redundancy, the higher efficiency, the lower switching losses and the reduction of the low order harmonics compared to two– and three–level VSC–HVDC [9], [10]. Within this thesis, the VSC converters are chosen as half–bridge MMC type, since this is the type of converters used in the context of the COBRAcable project. Further details about the converter model are given in the next section.

Transformer

The main function of the interface transformer is to transform the voltage of the AC system to a value suitable to the converter. It also provides reactance between the grid and the converter side in order to control the AC output current. Additionally, it is equipped with an on-load tap-changer which can regulate the voltage and optimize the VSC operation by reducing the power losses [11].

Phase Reactor

The phase reactors are used for controlling the active and reactive power flow as well as filter the high frequency switching harmonics generated by the converters [12]. Moreover, they limit the short-circuit current in case of a fault.

AC filter

The AC filters are installed in order to suppress the high frequency harmonic content of the AC voltage due to the converter's switching operation and prevent the harmonic components from being injected into the AC grid [12].

DC capacitor

The DC capacitor is used to keep the DC voltage constant by removing the ripple. It acts as an energy storage in the DC side and the DC voltage can be controlled by exchanging active power between the AC and DC sides. The choice of the capacitance value is a matter of trade-off between the voltage ripple and the dynamic performance.

DC line

Either overhead lines or cables can be used for HVDC transmission and the choice depends on many factors. Overhead lines are mostly used for bulk power transmission over long distances because of the lower installation costs. Cables are utilized in submarine applications in order to connect offshore wind farms to the land or for subsea transmission of electricity [13].

2.2 VSC–HVDC control structure

Two possible strategies can be applied for the implementation of the control in VSC–HVDC systems, i.e. the direct control and the vector control schemes [14]. The latter is the most widely employed since it enables the independent control of active and reactive power, as will be shown later. In this type of control, the three–phase quantities are transformed into the static $\alpha\beta$ stationary reference frame through the Clark transformation and then they are represented into the synchronous rotating dq–reference frame through the use of Park transformation. Next, the dynamic model equations are derived according to Figure 2.2 which presents the diagram of a VSC connected to the grid.

The dynamics of the AC side can be expressed in the $\alpha\beta$ stationary reference frame as follows:

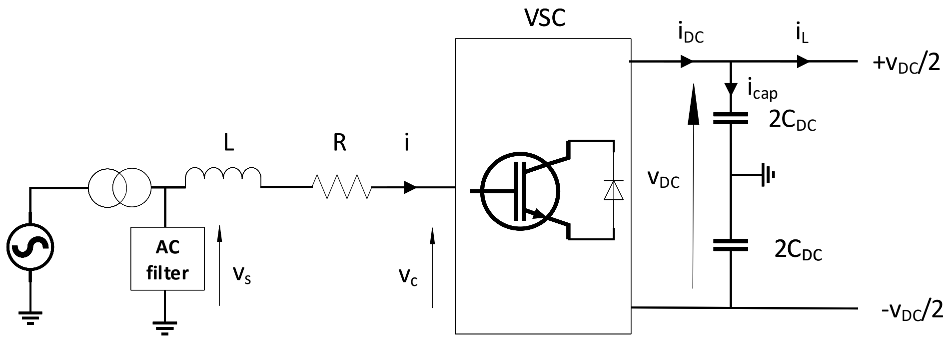

Figure 2.2. Single line diagram of a VSC–HVDC system.

$$L\frac{di_{\alpha\beta}}{dt} = v_{s,\alpha\beta} - v_{c,\alpha\beta} - Ri_{\alpha\beta} \tag{2.1}$$

In the dq reference frame, the former equation can be formulated as:

$$L\frac{di_{dq}}{dt} = v_{s,dq} - v_{c,dq} - (R + j\omega L)i_{\alpha\beta} \tag{2.2}$$

which can be further split into real and imaginary parts:

$$L\frac{di_{d}}{dt} = v_{s,d} - v_{c,d} - Ri_{d} + \omega Li_{q} \tag{2.3}$$

$$L\frac{di_{q}}{dt} = v_{s,q} - v_{c,q} - Ri_{q} - \omega Li_{d} \tag{2.4}$$

If the dq system is chosen in such a way that $v_d = v_s$ and $v_q = 0$, the active and reactive power can be expressed as:

$$p = v_{sd}i_d \tag{2.5}$$

$$q = -v_{sd}i_q \tag{2.6}$$

The following two equations can describe the DC side:

$$p_{DC} = v_{DC}i_{DC} \tag{2.7}$$

$$C\frac{dv_{DC}}{dt} = i_{DC} - i_L \tag{2.8}$$

Equations 2.5 and 2.6 lead to the intuitive conculsion that the active and reactive power can be controlled independently by controlling the -d and -q components of the current respectively. The vector control diagram for a VSC is given below and a brief explanation of its components follows.

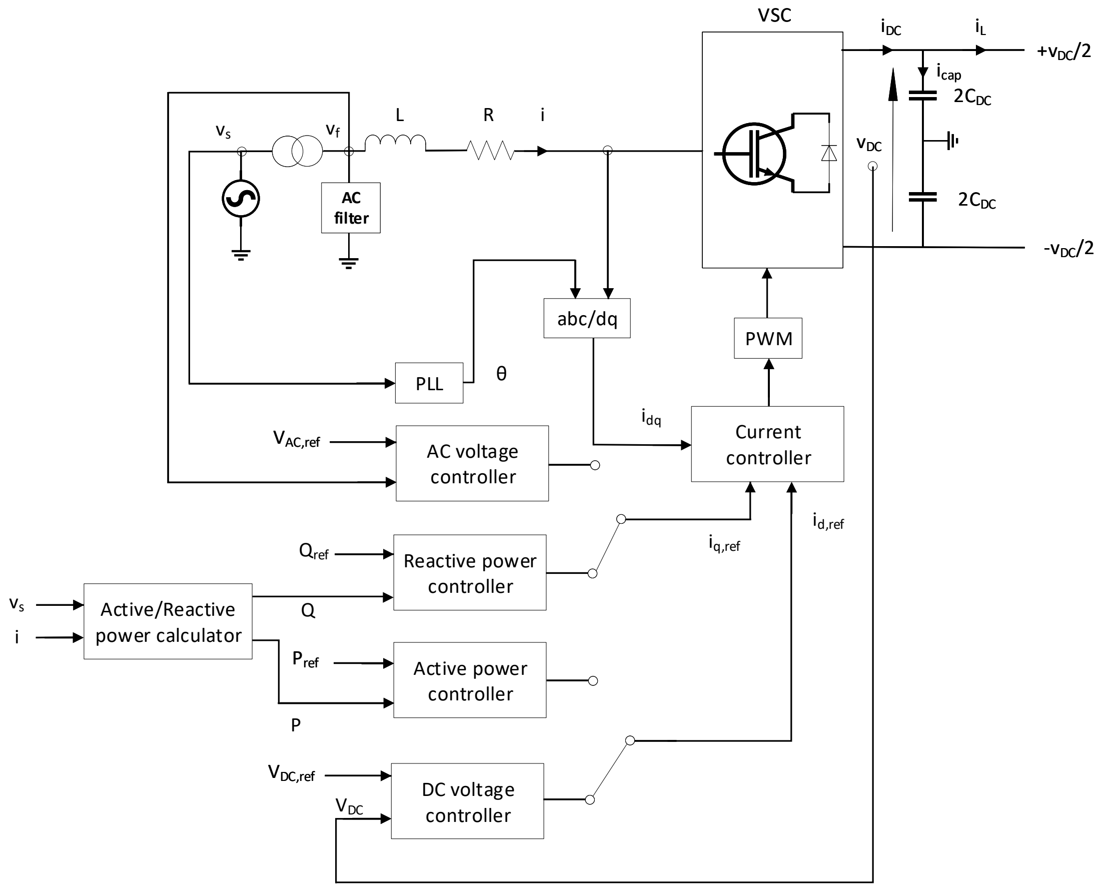

Figure 2.3. Vector control diagram.

2.2.1 PLL

The phase–locked loop (PLL) is used for detecting the grid voltage angle θ and locking the dq axis to this angle. As mentioned before, the d-axis voltage vector can be aligned with the grid voltage vector so that $v_d = v_{s,d}$ and $v_q = 0$. The latter can be implemented by considering v_q as an error and using it as an input for a PI controller. The simplified control diagram of a PLL is given in Figure 2.4. More detailed representation will be given in the next section.

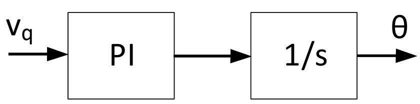

Figure 2.4. Block representation of PLL.

2.2.2 Current controller

The block diagram of the current controller is given below:

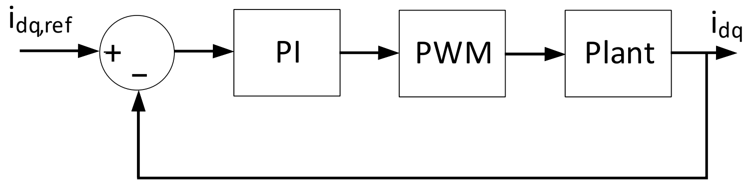

Figure 2.5. Block representation of the current controller.

The PI controller outputs the voltage references $v_{d,ref}$ and $v_{q,ref}$. For the PWM operation it can be written that $v_{dq} = v_{dq,ref}$, assuming that the converter voltage follows the reference without any delay and the switching harmonics are filtered out. The system plant is described by equations 2.3, 2.4 and its transfer function is expressed as $H(s) = \frac{1}{Ls+R}$. By observation of these equations, it can be seen that there is a cross–coupling between the currents i_d and i_q due to the existence of a frequency induced term in each of them. Furthermore, the currents are affected by disturbances of the grid voltage. By applying current cross–coupling and voltage feedforward compensation, the control performance can be improved. The equivalent block diagram of the current controller is modified as depicted in Figure 2.6, where these compensating terms can be observed:

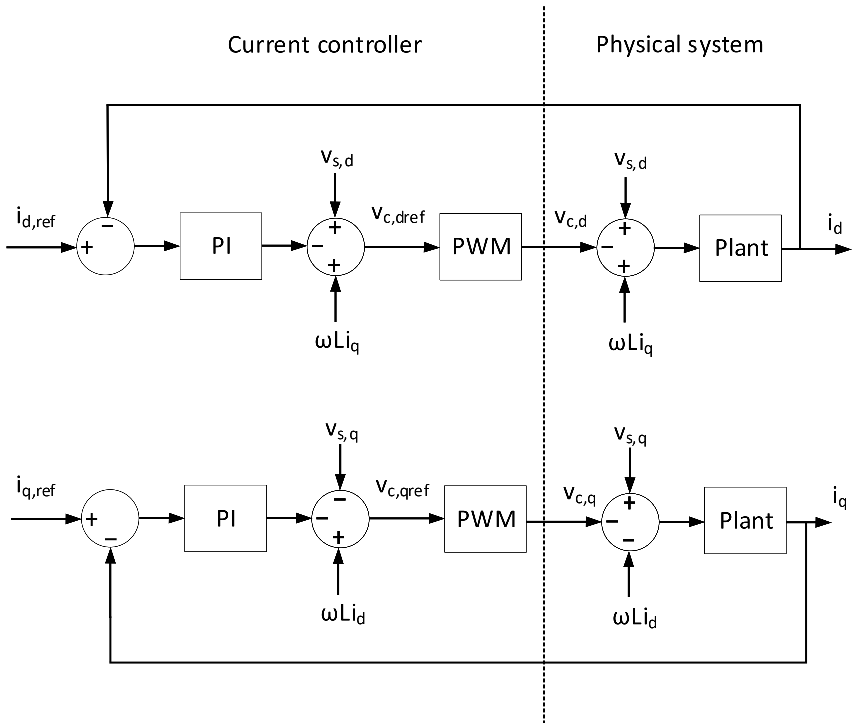

Figure 2.6. Block representation of current controller with the compensating terms added.

2.2.3 Outer controller

Regarding the outer control loop, four different control modes can be implemented, as shown in Figure 2.3:

- DC voltage control
- AC voltage control
- active power control
- reactive power control

When referring to active grids, there are four different possible types of control for each converter, i.e. P–Q, P–V_{AC}, V_{DC}–V_{AC} and V_{DC}–Q [15].

2.2.3.1 DC voltage controller

The output of the PI for this type of controller is the d–axis current, i.e.:

$$i_{d,ref} = (k_p + \frac{k_i}{s})(v_{DC,ref} - v_{DC}) \tag{2.9}$$

Equating the DC and AC side power(Equations 2.5, 2.7), the DC current can be written as:

$$i_{DC} = \frac{v_{s,d} i_d}{v_{DC}} \tag{2.10}$$

Furthermore, taking the Laplace transform of Equation 2.8, the DC voltage can be expressed as:

$$v_{DC} = \frac{i_{DC} - i_L}{Cs} \tag{2.11}$$

Based on the above Equations, the block diagram of the DC voltage controller can be derived as shown in Figure 2.7:

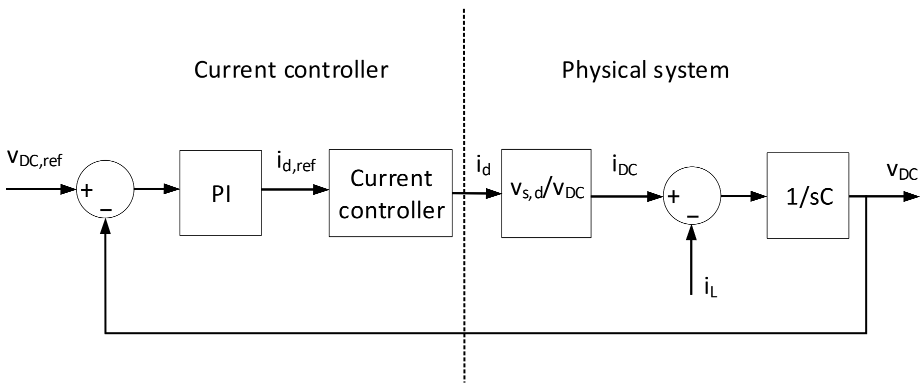

Figure 2.7. Block representation of the DC voltage controller.

2.2.3.2 AC voltage controller

The AC voltage is regulated via the q–axis current which modifies the reactive power magnitude and flow with the aim of keeping the voltage at the reference value(Figure 2.8). The q–axis reference current equals:

$$i_{q,ref} = (k_p + \frac{k_i}{s})(v_{AC,ref} - v_{AC}) \tag{2.12}$$

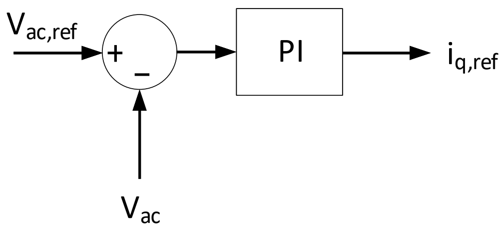

Figure 2.8. Block representation of the AC voltage controller.

2.2.3.3 Active and reactive power controllers

Figures 2.9 and 2.10 show the implementation of active and reactive power controllers respectively. The active power is controlled via the regulation of the i_d current while the i_q current determines the reactive power. It is also worth of mentioning that there is an anti–wind up limiter in each controller in order to limit the converter current within the allowable range.

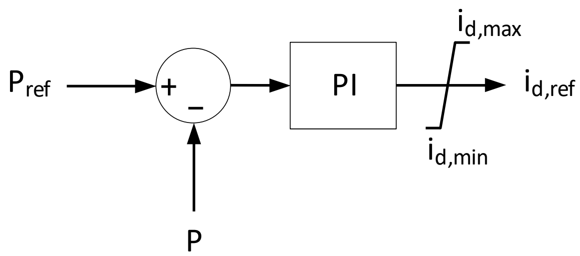

Figure 2.9. Block representation of the active power controller.

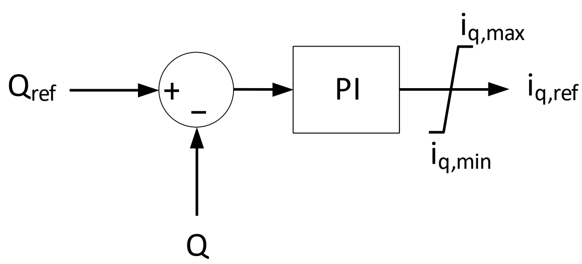

Figure 2.10. Block representation of the reactive power controller.

2.2.4 Current limiter

In contrast to electromechanical devices, e.g. generators, the VSCs do not have inherent overload capability. It might happen that the outer controller sets the current reference higher than the current capability which can result in the damage of the valves. Thus, a current limiter has to be implemented in the control system. Its function is to compare the total current $\sqrt{i_d^2 + i_q^2}$ to the maximum one and if the former is bigger, the current limiter limits one or both reference currents, depending on the implemented limiting strategy, as presented in Figure 2.11.

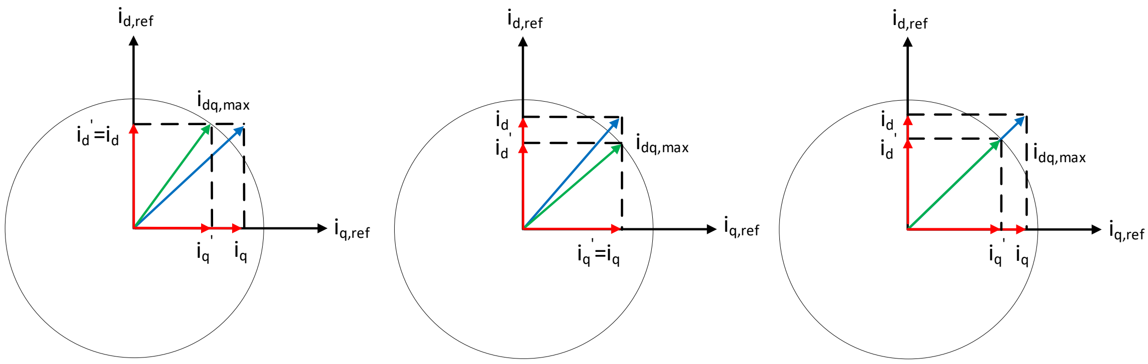

Figure 2.11. Current limiter strategies.

In the first strategy, the d–component of the current is prioritized with the q–component being limited. This strategy is applied in case that the converter is connected to a strong grid and it needs to produce more active power. On the contrary, in case of connection to a weak grid or supply of an industrial plant, i_q is prioritized in order to control the injected or absorbed reactive power and thus support the AC voltage, e.g. allow the converter increase its reactive power provision equal to its rating when a voltage dips occurs. In the third strategy, the angle of the current magnitude is kept constant by reducing both components [16].

2.3 Model development in PowerFactory

Several types of computational models have been developed for the simulation of voltage source converters and their applicability depends on the purpose of power system study that has to be performed [13]. In the context of this thesis the focus is put on the analysis of the slow dynamic interaction between the HVDC and its interconnected AC system. Thus, the phasor model (also known as RMS or fundamental frequency model) is utilized for the representation of the MMC–VSC–HVDC in DIgSILENT PowerFactory. Depending on the range of transient phenomena, there are three different simulation functions available in PowerFactory. Among them, the balanced RMS simulation function is chosen since low transient phenomena are simulated in this thesis and thus the dynamic behaviour of the passive network components is not taken into account (in contrast to the three–phase EMT simulation function), increasing the simulation speed. It uses a symmetrical, steady–state representation of the passive electrical network and it considers only the fundamental components of voltages and currents, allowing the insertion of symmetrical faults only.

Throughout the rest of the section, an insight into the modelling of the whole HVDC system is given.

2.3.1 MMC–VSC–HVDC PtP system implementation

Within this subsection, a brief overview of the model used for simulations in PowerFactory is given initially. The model was implemented based on the "HVDC Connected Offshore Wind Farm" example which is incorporated into the Application Examples of PowerFactory. This model consists of an HVDC connection between an offshore wind farm and an onshore grid and it was modified such that a PtP VSC–HVDC system between two onshore terminals is obtained. Moreover, the example's data was used for the various components of the HVDC system. Subsequently, the way of modelling for the different parts of the system is presented.

2.3.1.1 An overview of the HVDC topology used in PowerFactory

Figure 2.12 presents the point–to–point configuration used within this thesis for simulation purposes. The system consists of two Half–Bridge MMCs which are in symmetrical monopole configuration since they are connected via DC cables of positive and negative polarity without ground or metallic return. The converters are connected to identical AC grids via interface transformers. Converters 1 and 2 were set in P–Q and V_{DC}–V_{AC} control mode respectively.

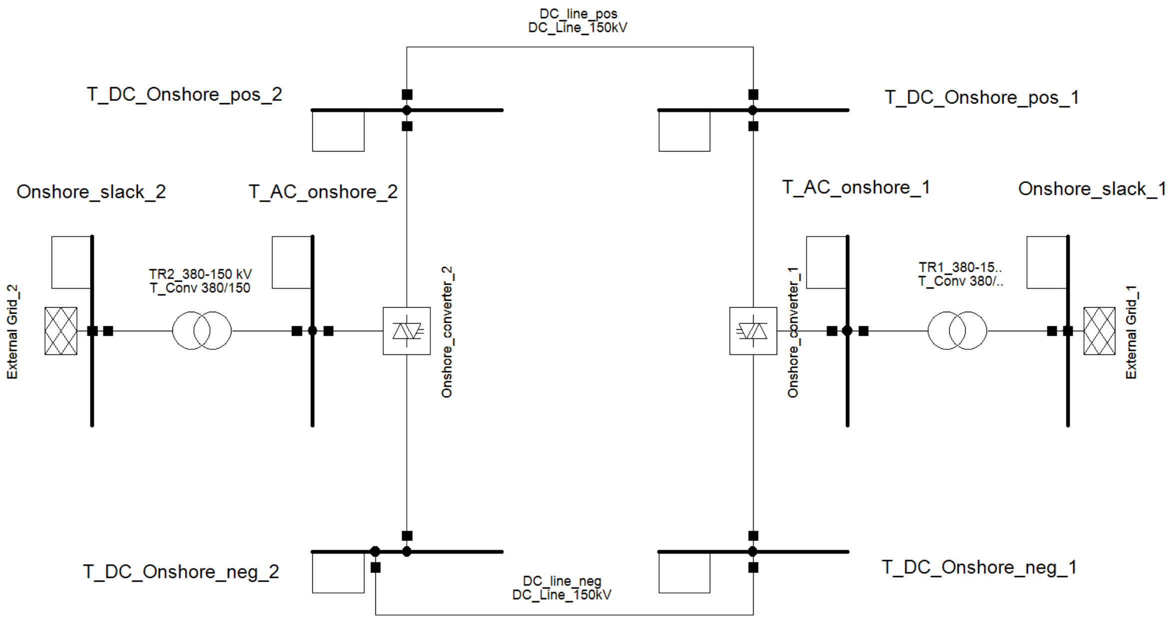

Figure 2.12. HVDC topology used for simulations in PowerFactory.

At this point, the composite model frame for the VSC controllers is presented in Figure 2.13. This is an overview diagram that shows the interconnections between the slots. Multiple instances (called composite models) which inherit the structure of this frame can be created depending on the number of the modelled converters. It consists of the measuring blocks for the active and reactive power as well as the AC and DC voltage. Also, it contains the main (outer) controller, the current (inner) controller, the PLL and the converter unit. This frame is built–in in PowerFactory. However, the outer and inner controller blocks were modified, as will be shown in the next paragraphs.

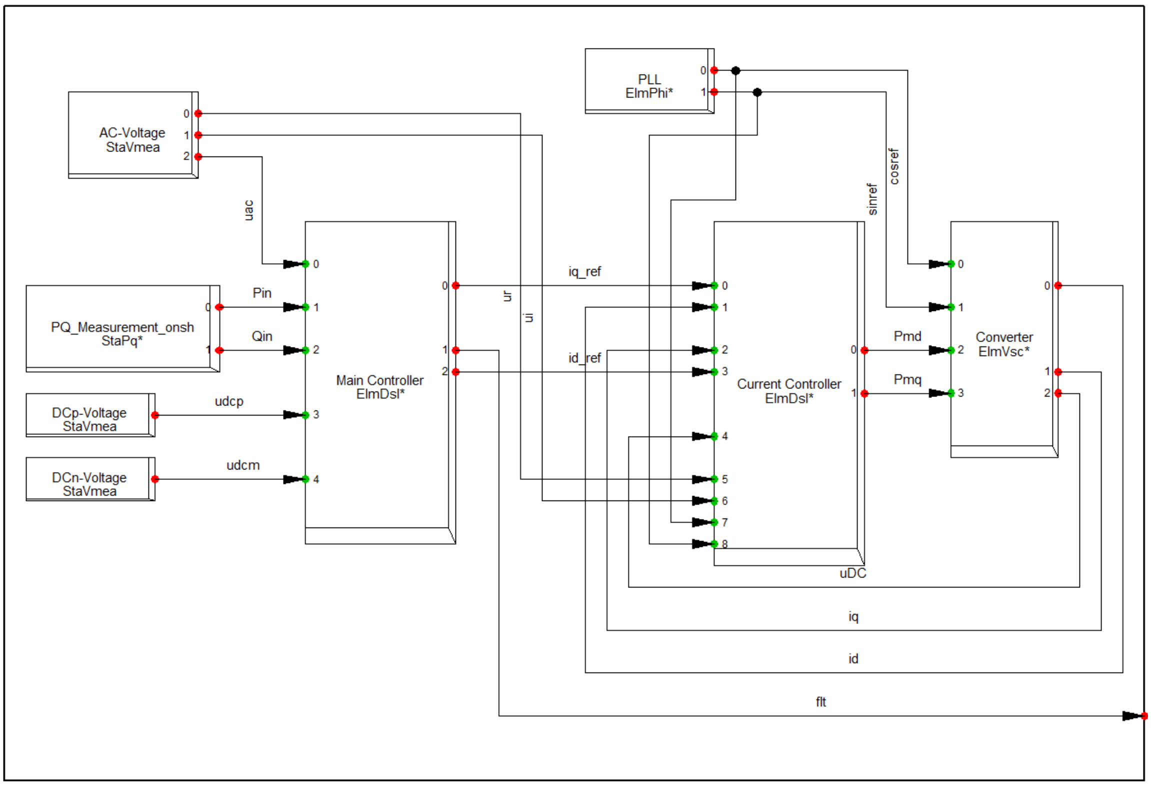

Figure 2.13. Composite model frame for each VSC controller.

2.3.1.2 Grid model

The External Grid Element was used to represent the two AC grids. The model used for the Load Flow calculation depends on the choice of the bus type which was selected as SL(slack). This means that the grid controls the voltage, the angle and the frequency of the bus to which is connected. Furthermore, the external grid is modelled as a synchronous generator for the simulation part.

2.3.1.3 PWM converter model

The RMS model of the PWM converter in Powerfactory lies on a fundamental frequency approach, meaning that the converter output voltage is purely sinusoidal. The converter is modelled by a DC voltage controlled three–phase AC voltage source in the AC–side and the DC–side can be seen as current–controlled source conserving active power balance between the two sides.

The phase–to–phase RMS positive sequence voltage of the converter is calculated as [17]:

$$\overline{V_C} = K_0 P_m V_{DC}(cosphi + jsinphi) \tag{2.13}$$

where:

- $K_0 = \frac{\sqrt{3}}{2 \cdot \sqrt{2}}$ for sinusoidal modulation.
- $P_m = \sqrt{P_{md}^2 + P_{mq}^2}$ is the modulation index, with P_{md} and P_{mq} being the outputs of the current controller that are given as inputs to the converter.
- V_{DC} is the DC side voltage.
- $cosphi = \frac{P_{md}cos\theta - P_{mq}sin\theta}{P_m}$ and $sinphi = \frac{P_{md}sin\theta + P_{mq}cos\theta}{P_m}$, with $cos\theta$ and $sin\theta$ being the PLL outputs which are given as inputs to the converter and θ is the angle of the grid voltage phasor.

The equivalent RMS circuit of the VSC is given in Figure 2.14:

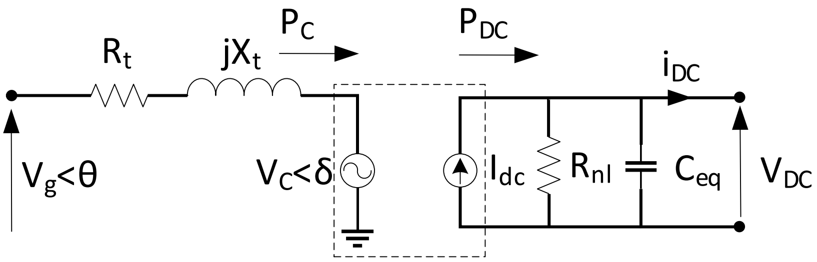

Figure 2.14. Equivalent RMS circuit of the VSC.

According to the Figure, the following equations apply for the AC side, written in the dq–frame:

$$V_{C,d} = V_{g,d} - I_d R_t + I_q X_t \tag{2.14}$$

$$V_{C,q} = V_{g,q} - I_q R_t - I_d X_t \tag{2.15}$$

where R_t and X_t are the total resistance and reactance of the AC side resprectively. Their values can be calculated according to Equations 2.16, 2.17:

$$R_t = R_{tr} + \frac{R_{arm}}{2} \tag{2.16}$$

$$X_t = X_{tr} + \frac{X_{arm}}{2} \tag{2.17}$$

where:

- R_{tr}, X_{tr} are the resistance and leakage reactance of the converter transformer respectively.

- R_{arm} is the arm resistance and X_{arm} its reactance.

The DC side can be coupled to the AC side by using the active power balance between them, as mentioned previously, i.e. $P_C = P_{DC}$. Thus, the equivalent DC current source can be expressed as:

$$i_{dc} = \frac{V_{C,d}I_d + V_{C,q}I_q}{V_{DC}} \tag{2.18}$$

Regarding the converter losses, the most important type are the no-load losses resulting from periodically recharging the transistor capacitances and they are modelled by adding the resistance R_{nl} between the DC terminals. Furthermore, given the submodule capacitance C_{sm} and the number of submodules per arm n, the equivalent DC side capacitance is calculated as [9]:

$$C_{eq} = \frac{6 \cdot C_{sm}}{n} \tag{2.19}$$

2.3.1.4 DC cable model

The lumped parameters (PI) model was used for the purpose of the DC cable modelling since it provides sufficient results for short lines, i.e. 100 km in the case under study.

2.3.1.5 PLL model

Figure 2.15 presents the way of modelling the PLL for RMS simulations, as can be found in the technical reference documentation of PowerFactory [18]. As can be seen, the real and imaginary components of the grid voltage phasor are given as inputs to the PLL which determines its phase angle. The q–axis component of the voltage is fed as an error to a PI controller, thus the d–axis is aligned to the voltage phasor when $v_q = 0$. The PLL outputs are *cosθ* and *sinθ* and they are used as inputs for the PWM converter.

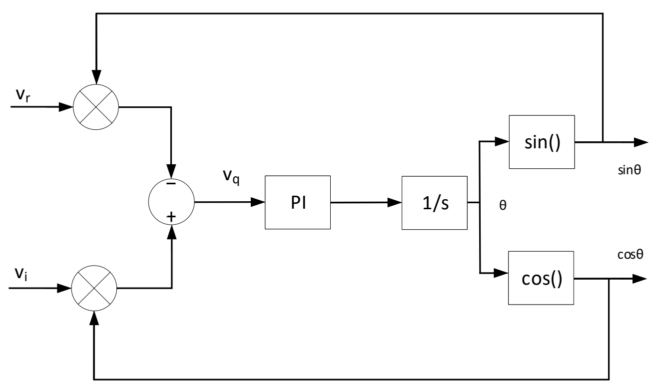

Figure 2.15. DIgSILENT PLL block diagram (RMS simulation).

2.3.1.6 Outer controllers

Figure 2.16 presents the Model Definition of the outer controller. The Model Definition is essentially the design or blueprint for a piece of equipment (in this case the controller) in PowerFactory and in order to link it to the actual controllers with specific parameter settings, two Common Models were created, one for each of the two converter controllers.

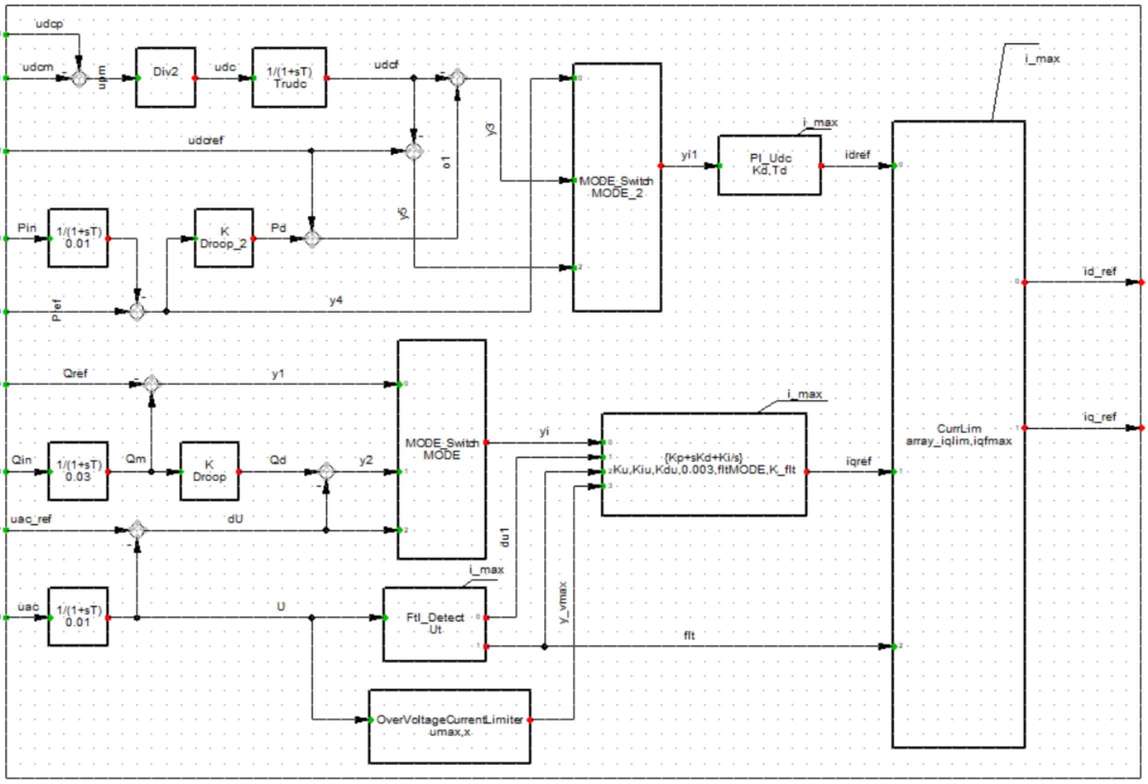

Figure 2.16. VSC main control structure

From Figure 2.16, it can be observed that there are four outer loops which are related to the active power, reactive power, AC voltage and DC voltage. There are also two droop control loops, i.e Q–V_{AC} and P–V_{DC} . It should be mentioned that the Model Definition had to be modified in order to include the P–V_{DC} droop control scheme as well as the active power control loop. Depending on the chosen MODE value inside the MODE switch block, the control mode for each converter can be determined, as depicted in Table 2.1:

Table 2.1. Control mode selection due to MODE switch block value

upper MODE	**Control mode**
0	P control
1	P–V_{DC} droop control
2	V_{DC} control
lower MODE	**Control mode**
0	Q control
1	Q–V_{AC} droop control
2	V_{AC} control

2.3.1.7 Current controller

The current controller was implemented using an existing User Defined Model as a starting point. The compensating terms had to be added, as it was explained in subsection 2.2.2. The obtained diagram can be seen in Figure 2.17.

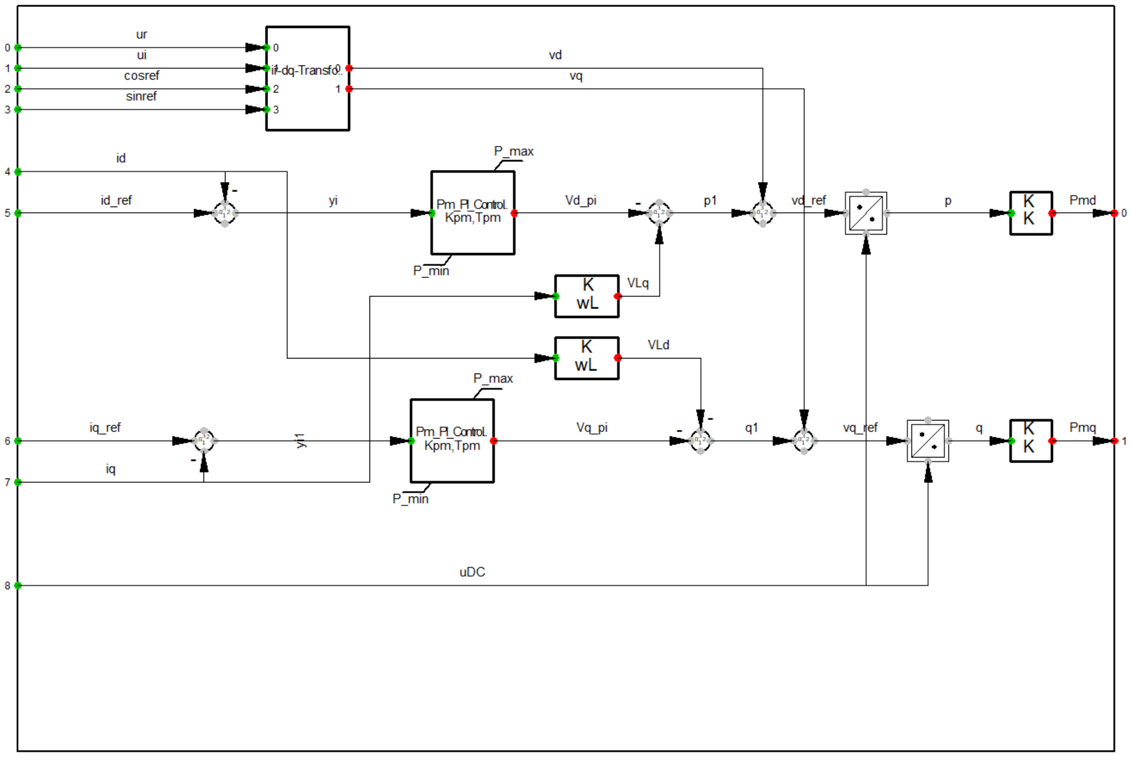

Figure 2.17. VSC current control structure

As it has already been presented in Figure 2.13, the implementation of the current controller in PowerFactory is done such that it outputs the modulation indexes and not the voltage references. Therefore, in order to obtain the desired $v_{d,ref}$ and $v_{q,ref}$, Equation 2.13 can be utilized in order to obtain the expressions of the PWM indexes as shown below:

$$P_{md} = \frac{V_{cd,ref}}{V_{DC}} \cdot \frac{2 \cdot \sqrt{2}}{\sqrt{3}} \tag{2.20}$$

$$P_{mq} = \frac{V_{cq,ref}}{V_{DC}\cdot} \cdot \frac{2 \cdot \sqrt{2}}{\sqrt{3}} \tag{2.21}$$

Since the controllers were implemented in pu, the above expressions can be rewritten as:

$$P_{md} = \frac{v_{cd,ref} V_{d,base}}{v_{DC} V_{DC,base}} \cdot \frac{2 \cdot \sqrt{2}}{\sqrt{3}} \tag{2.22}$$

$$P_{mq} = \frac{v_{cq,ref} V_{q,base}}{v_{DC} V_{DC,base}} \cdot \frac{2 \cdot \sqrt{2}}{\sqrt{3}} \tag{2.23}$$

where $V_{d,base} = 110\,\text{kV}$ and $V_{DC,base} = 300\,\text{kV}$

The final expressions for the modulation indexes are:

$$P_{md} = \frac{v_{cd,ref}}{v_{DC}} \cdot 0.6 \tag{2.24}$$

$$P_{mq} = \frac{v_{cq,ref}}{v_{DC}} \cdot 0.6 \tag{2.25}$$

2.3.2 Tuning of the PI controllers for the HVDC system

Within this subsection, the tuning of control loops for the two voltage source converters is presented. It should be highlighted that the aim of the tuning process was to ensure the stable performance of the HVDC system such that it does not introduce any instabilty into the two–area test system due to improper choice of PI parameters. The specifications set for tuning are summarized below:

- The integral time constant of the PI controllers should be adequately larger than the integration step size used by PowerFactory to perform its calculations. The choice of smaller values for the step size leads to increased accuracy of the simulation results but slows down the convergence. For the simulation of electromechanical transients (which is the case under study), the step size is typically chosen equal to 0.01 s [19]. In this case, the step size was chosen equal to 0.001 s and the current controller integral time constant, i.e. the smallest time constant of the system, was chosen equal to 0.007 s. Thus, both good accuracy and convergence were achieved.
- The overshoot of the outer loop variables, i.e. active power, reactive power, DC voltage and AC voltage should be lower than 5%.
- The inner(current) loop should be faster than the outer loop in order to decouple the dynamics between them. This is an important requirement that has to be fulfilled when choosing the PI parameters for a cascase control structure so that stable operation is achieved [20].
- At the same time, the current loop bandwidth should be five times lower than the converter switching frequency, as it will be explained below.
- The outer loop should be faster than the POD controller dynamics.

Figure 2.18 presents the different dynamics that appear in the AC and HVDC grids and their associated time constants compared to the fundamental period of the AC grid voltages and currents.

In order to determine the bandwidth of the current loop, the MMC switching frequency is chosen equal to $f_{sw} = 250\,\text{Hz}$. Normally, in order to ensure proper system performance, the system bandwidth is recommended to be chosen such that it fulfills the following requirement [21]:

$$a_c \leq \frac{2\pi f_s}{10} \tag{2.26}$$

where f_s is the sampling frequency. By choosing $f_s = 2f_{sw}$, the closed–loop bandwidth of the current controller was chosen as:

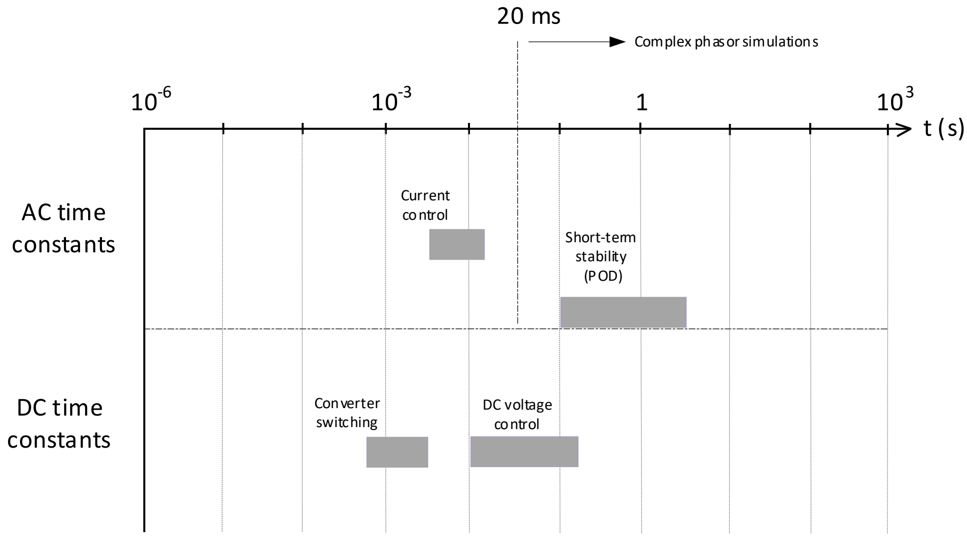

Figure 2.18. AC and HVDC grid dynamics

$$a_c = \frac{2\pi f_{sw}}{5} \tag{2.27}$$

Furthermore, in order to avoid any possible interferences between the cascaded control loops, the response time of the outer control loops must be much longer compared to the inner control loops, as mentioned previously. Typically, it is chosen such that it is at least ten times slower. Therefore, the closed–loop bandwidth of the outer controllers was selected as:

$$a_o = \frac{a_c}{10} \tag{2.28}$$

Given these bandwidth specifications, the rise time for the inner and outer control loops can be calculated based on the following formula:

$$t_r = \frac{ln(9)}{a} \tag{2.29}$$

Equation 2.29 relates the rise time (t_r) to the bandwidth (a) of a first–order system but it can also be used for the rise time calculation of higher order systems. By substituting the inner and outer loop bandwidth values to Equation 2.29, the resulting rise times are $t_{r,i} = 7\,\text{ms}$ and $t_{r,o} = 70\,\text{ms}$ respectively.

In the case under study, the PI parameters were chosen by trial and error with the aim of meeting the aforementioned specifications. The system was tested under step inputs, i.e. the step responses for both the inner and outer loops were measured. Initially, the current loop was tuned. Figures 2.19, 2.20 present the responses of the d and q–axis currents of converter 1 under step changes in the references at $t = 0.1\,\text{s}$. It can be seen that the current rise time is approximately equal to 7 ms.

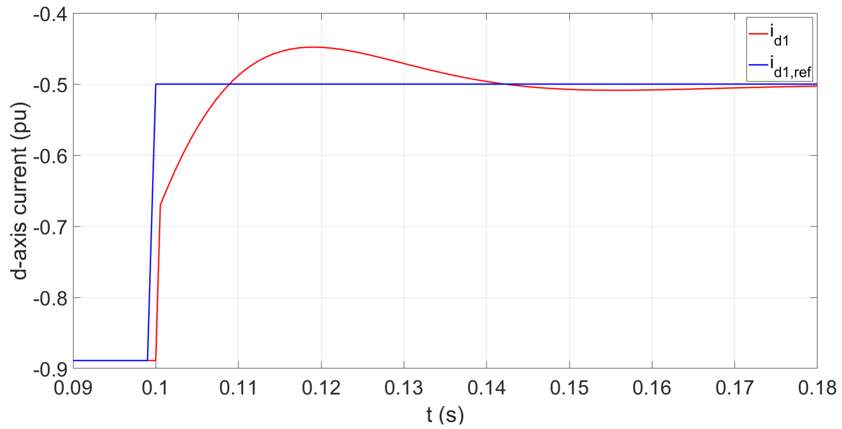

Figure 2.19. Measured d–axis current of converter 1 under a step change in the reference equal to $i_{d1,ref} = -0.5$ pu.

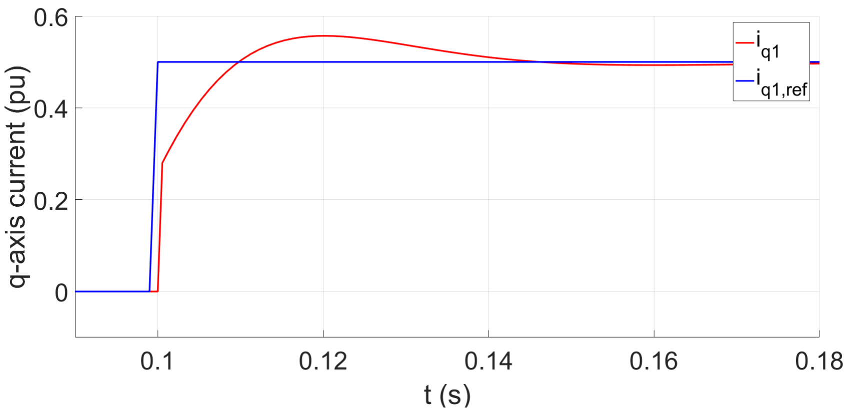

Figure 2.20. Measured q–axis current of converter 1 under a step change in the reference equal to $i_{q1,ref} = 0.5$ pu.

Subsequently, the outer loop of converter 1 is tuned. First, the resulting active power response is presented in Figure 2.21, when the active power reference changes from -1 to 0 pu at $t = 0.1$ s. The active power rise time is around 70 ms. The reactive power response of converter 1 is also given in Figure 2.22 for a step change in the reactive power. The rise time is almost 70 ms and it presents an overshoot of approximately 4%.

At this point, the measured reactive power at Onshore slack 1 is also presented in Figure 2.23 for the step change in active power of converter 1. When the step change is applied, the reactive power experiences a small undershoot equal to -0.11 pu but it restores to its reference of 0 pu within 0.3 s, showing that the active power change does not affect the reactive power, i.e. they are controlled independently.

Regarding converter 2, only the outer loop responses are plotted since the inner loop gain values are chosen the same as converter 1. Figures 2.24 and 2.25 present the AC and DC voltage responses when the reference value changes from the nominal to 0.95 pu at 0.1 s. It can be observed that the rise time for both DC and AC voltages is within the range of 70 ms. Furthermore, the DC voltage experiences an undershoot of 4%, whereas it settles to the reference within 1 s.

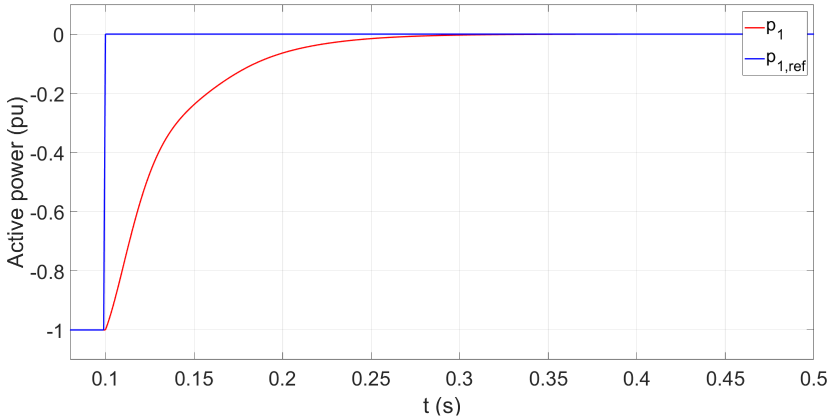

Figure 2.21. Measured active power at Onshore slack 1 under a step change in the reference equal to $p_{1,ref} = 0$ pu.

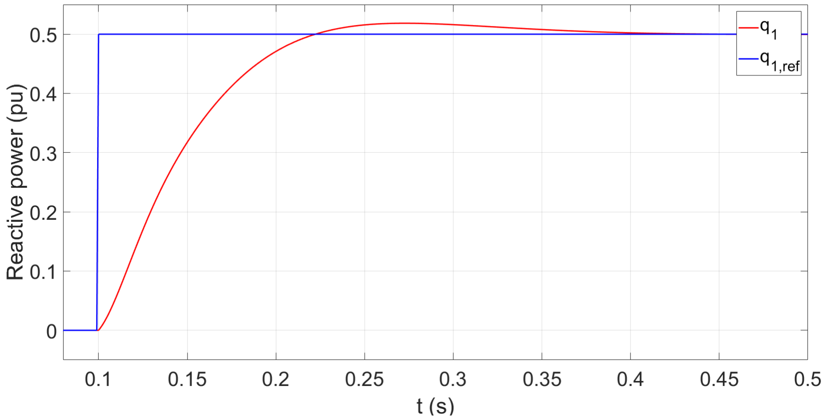

Figure 2.22. Measured reactive power at Onshore slack 1 under a step change in the reference equal to $q_{1,ref} = 0.5$ pu.

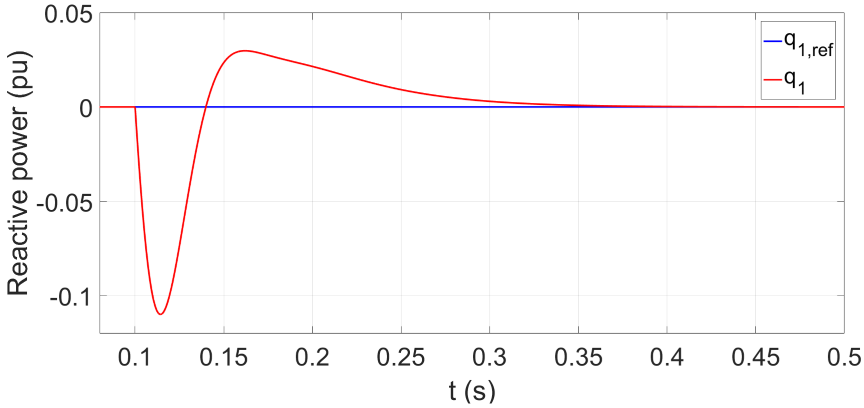

Figure 2.23. Measured reactive power at Onshore slack 1 under a step change in the reference equal to $p_{1,ref} = 0$ pu.

Table 2.2 summarizes the chosen PI parameters for the inner and outer control loops of controllers 1 and 2.

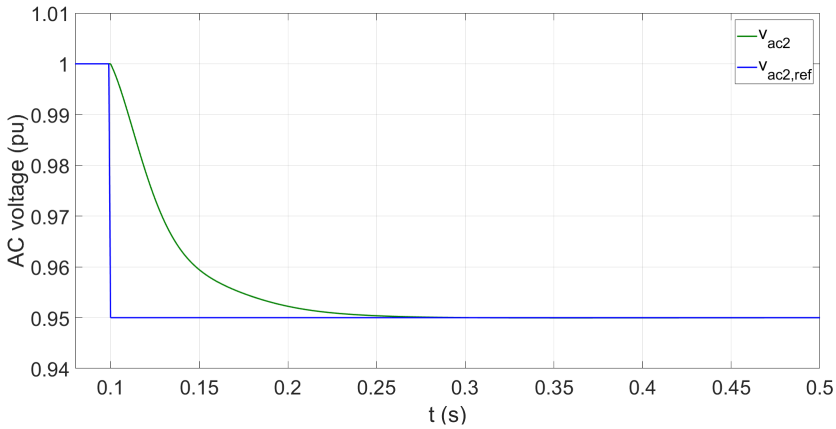

Figure 2.24. Measured AC voltage at the AC onshore slack terminal 2 for a step change in the reference equal to $v_{ac2,ref} = 0.95$ pu.

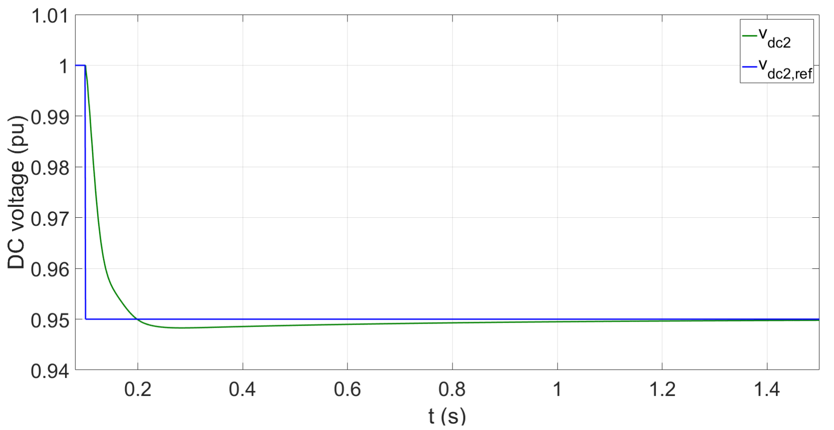

Figure 2.25. Measured DC voltage at the DC onshore slack terminal 2 for a step change in the reference equal to $v_{dc2,ref} = 0.95$ pu.

Table 2.2. PI parameters for the PtP HVDC system

Parameters	Symbol	Value
Current proportional gain (d and q–axis)	$k_{p,cc}$	1 pu
Current integral time constant (d and q–axis)	$T_{i,cc}$	0.007 s
Active power proportional gain	$k_{p,p}$	0 pu
Active power integral time constant	$T_{i,p}$	0.04 s
Rective power proportional gain	$k_{p,q}$	0 pu
Rective power integral time constant	$T_{i,q}$	0.08 s
DC voltage proportional gain	$k_{p,vdc}$	4 pu
DC voltage integral time constant	$T_{i,vdc}$	0.15 s
AC voltage proportional gain	$k_{p,vac}$	0 pu
AC voltage integral time constant	$T_{i,vac}$	0.0066 s

2.3.3 POD controller implementation

This section presents the implementation of the POD controller which acts in a supplementary way to the main HVDC control strategy in order to damp the oscillations appeared in power systems. Its design follows that of a conventional PSS, i.e. it consists of a washout filter, a gain and a number of lead–lag filters, as can be seen in Figure 2.26 from left to right.

The POD controller takes as an input the active power. In the case under study, the active power of line 7-8-1 (Figure 3.2) was used as an input. However, in practice, the selection of the input is not unique since alternative oscillatory signals can be used. These include the power angles, the currents flowing through the AC inter-tie lines, the voltages or phase angles at the ends of the AC inter-tie lines, the rotor angles or the generator speeds. The washout filter is essentially a high–pass filter which allows signals related with oscillations in active power to pass unchanged. This means that during steady state, i.e. when the active power flow is constant, the output of this controller is zero. The time constant T_{sw} is normally chosen in the rage of 1–20 seconds. The gain K_d determines the amount of damping, whereas the purpose of the lead–lag filter is to compensate the phase lag between the controller's input and output. In practice, two or more first–order blocks can be used to provide the necessary phase compensation [22]. The output of the controller ΔP is added to the reference active power of the converter, modulating the DC link active power flow and thus contributing to the damping of the power oscillations of the AC side. Moreover, it is limited within ΔP_{min} and ΔP_{max} values.

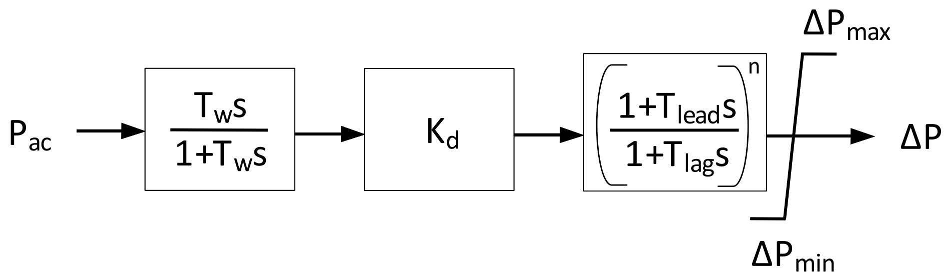

Figure 2.26. PSS–based POD controller for HVDC.

The POD controller was implemented in Powerfactory using pre–built blocks for the washout filter, the gain and the lead–lag filter, located inside its Global Library. The controller configuration was added in the Model Definition of the main controller (Figure 2.16) which is given again below, including the POD function. More details regarding the choice criteria of the parameters will be given in Chapter 4.

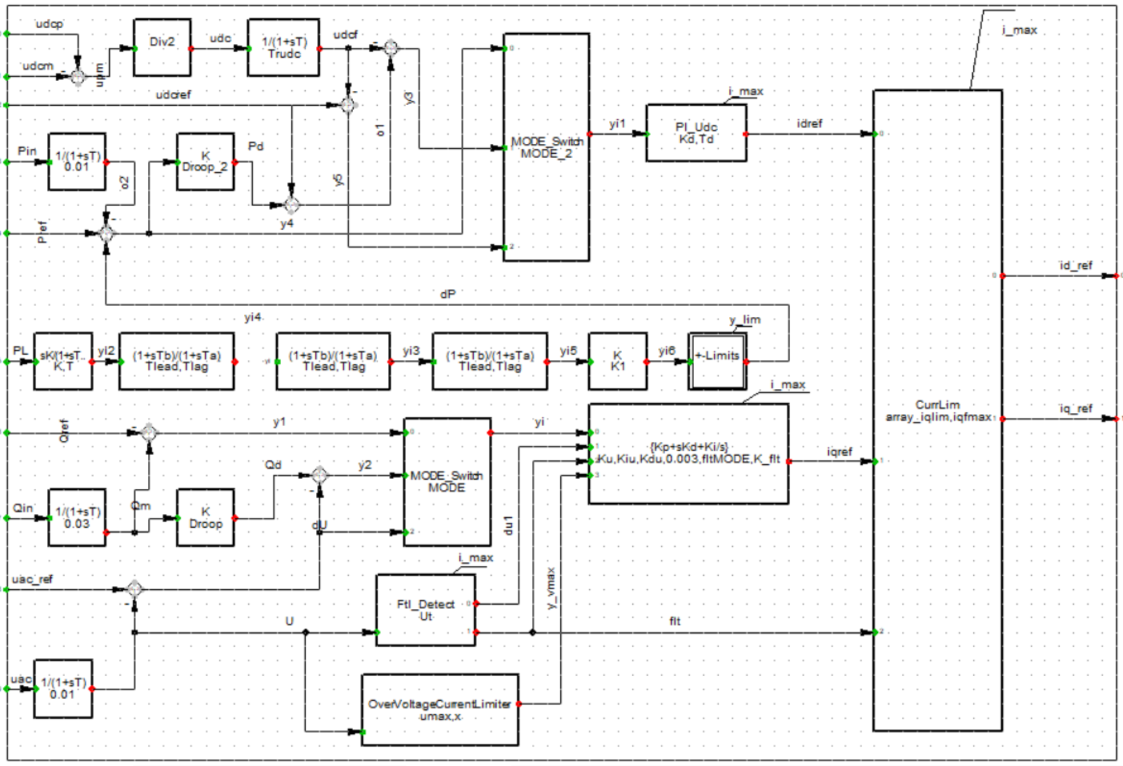

Figure 2.27. VSC main control structure including the POD funtion

3 Outline and parameters of the test systems

The scope of this chapter is to provide the outline and the main parameters of the three systems under test. The explicit systems' parameters and the dynamic data of their components used for the realization of the simulations throughout the next chapter are then given in detail in Appendix A.

3.1 Two–area test system

In the context of this thesis, the focus is put on the damping of the inter-area power oscillations. The operational test platform which is utilized in order to introduce such oscillations is presented in Figure 3.1:

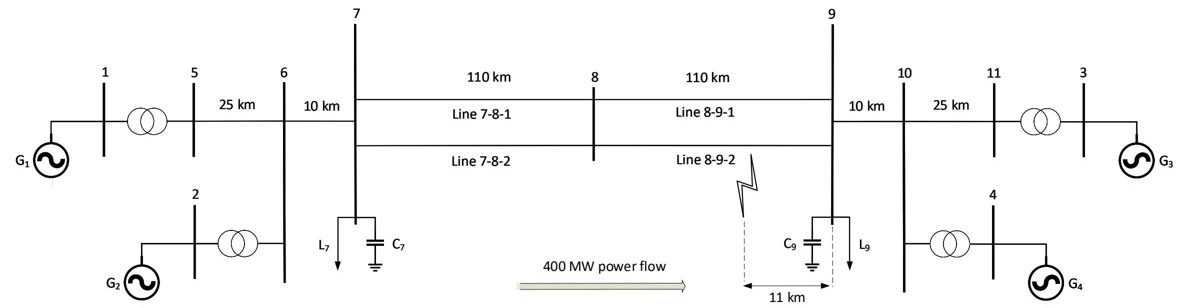

Figure 3.1. Two–area test system.

The above configuration is a benchmark system frequently used in inter-area oscillation studies. It was originally designed by Ontario Hydro with the aim of exhibiting the different types of oscillations appeared in interconnected power systems and studying the fundamental nature of inter–area oscillations [4]. It lacks of complexity and thus it can provide a systematic way for studying the inter–area oscillation modes and applying the appropriate control techniques in order to damp them. Therefore, it was used as a basis within this thesis work for introducing transient events.

As can be seen from the above Figure, the two–area system consists of two identical areas connected by weak tie lines with total length equal to 220 km. Each area comprises of two generators with nominal ratings $S_n = 900\,\mathrm{MVA}$ and $V_n = 20\,\mathrm{kV}$. The generator units are equipped with automatic voltage regulators (IEEE type AC4 excitation system), power system stabilizers (IEEE type PSS1) and speed governors (IEEE type 1 speed-governing model). They are connected to the transmission level through 20/230 kV transformers.

The generators supply two loads connected at buses 7 and 9, whereas shunt capacitors are connected to the the same buses. In steady–state, area 1 exports 400 MW to area 2. For all the cases under study, a three–phase short–circuit was introduced at Line 8-9-2, 11 km from BUS 9. The two–area system, excluding the HVDC link, was initially tested and the values of its components and control parameters are listed in Table A.1 of Appendix A.

3.2 Two–area test system incorporating the VSC-HVDC link

The second system that was tested is the two–area system incorporating the HVDC link (Figure 3.2).

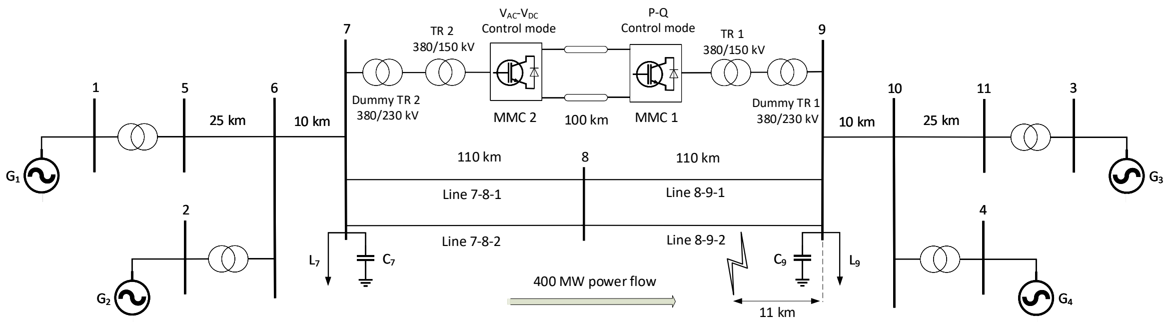

Figure 3.2. Two–area test system incorporating the HVDC link.

Table A.2 summarizes the parameters of the different components that constitute the point–to–point HVDC topology (Figure 2.12). These include the external grid elements (which are essentially stiff AC voltage sources connected to both sides of the HVDC link, as described in subsection 2.3.1.2), the converter transformers, the modular multilevel converters and the DC cables. Also, the data of dummy transformers is given. Once the PtP system was tuned, the external grid elements of Figure 2.12 were removed and these type of transformers were connected instead, with the purpose of connecting the HVDC link with Buses 7 and 9 (Figure 3.2). Their resistance was specified to zero and their reactance was also considered negligible.

3.3 MTDC system

The third system under study is the two–area system incorporating the expanded three–terminal system, as depicted in Figure 3.3. An offshore converter was connected to the DC terminals T_p and T_n via cables of 70 km length. The terminals are located at a distance of 30 km from the DC terminals of converter 2 and 70 km from those of converter 1. The wind farm was modelled by using the Standard Asynchronous Machine type of PowerFactory and choosing 100 asynchronous machines connected in parallel. An aggregated model consisting of 100 0.69/33 kV step up transformers with nominal rating of 5.6 MVA and a 33/155 kV dummy transformer rated at 450 MVA were used to connect the offshore converter MMC 3 to the wind farm. The parameters for each asynchronous machine, the offshore converter, the transformers and the DC cables are given in Table A.3.

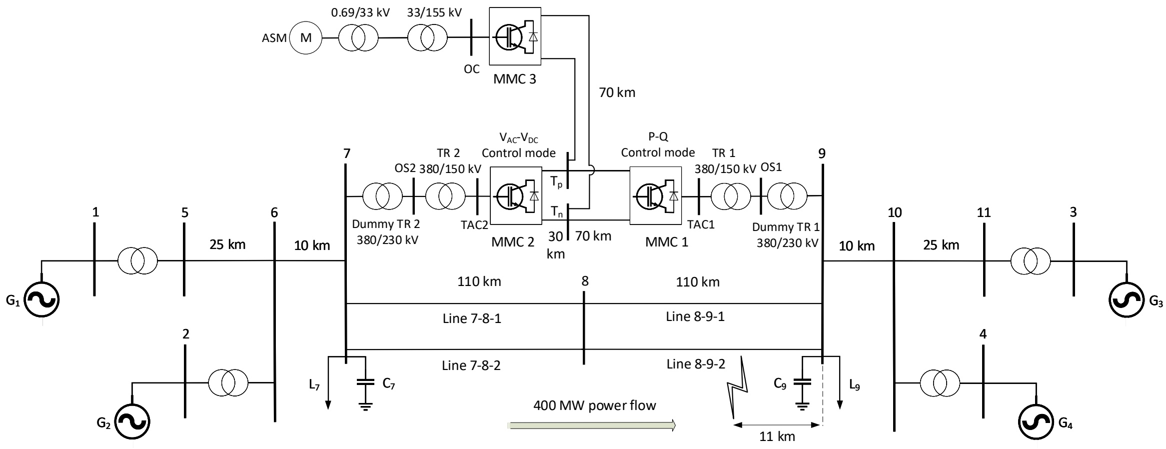

Figure 3.3. Two–area test system incorporating the three terminal HVDC system.

Simulation results of the test systems 4

This chapter begins with the simulation of the two–area system which is perturbed by means of a three–phase short–circuit in order to excite the inter–area oscillation modes. Afterwards, the VSC–HVDC link is integrated into the two–area system and the POD controller is properly tuned with the aim of damping the interarea oscillations. In the final section of this chapter, the influence of the offshore converter into the existing POD control behaviour is analyzed by considering different simulation scenarios. Additionally, a compensation method of tuning the POD controller for the MTDC system is applied.

4.1 Test system 1: Two–area system

Within this section, the test system was subjected to a disturbance by means of a three–phase short–circuit in order to excite the inter–area modes of oscillation. The gains of the PSS for all four generators were significantly reduced by a factor of ten, i.e. $K = 20$, with the aim of highlighting the stability provided by the auxiliary POD controller when the HVDC link is connected to the AC test system. Before proceeding with the time–domain simulation, a modal analysis was performed in order to record the locations of the eigenvalues associated with the inter–area modes.

Modal analysis, also referred in the literature as eigenvalue analysis or small signal stability, outputs the eigenvalues of the linearized system. Among them, the complex eigenvalues reflect the system's oscillatory behaviour, always appearing in the form of complex conjugates. Their real and imaginary part represent the damping factor and the frequency of the corresponding mode respectively. A measure for the damping of the oscillations is the damping ratio which is defined as:

$$\zeta = \frac{-\sigma}{\sqrt{\sigma^2 + \omega^2}} \tag{4.1}$$

where σ and ω are the real and imaginary part of the corresponding eigenvalue $\lambda = \sigma + j\omega$ respectively. In order to operate the power systems within adequate stability margins, the damping ratio of the oscillatory modes should be bigger than 5% [5]. For most power systems, a damping ratio value between 5% to 10% is acceptable. However, the 10% value is recommended for secure system operation [23]. The modes that present lower damping ratio are defined as critical oscillatory modes and they can have negative consequences for the power systems including lack of stability, cascading events and detrimental system blackouts.

The results of the modal analysis are presented in Figure 4.1. The inter–area oscillatory modes are those whose eigenvalues are in the frequency range of 0.2 to 1 Hz, where the frequecy of the i^{th} eigenvalue is calculated as $f_i = \frac{\omega_i}{2 \cdot \pi}$.

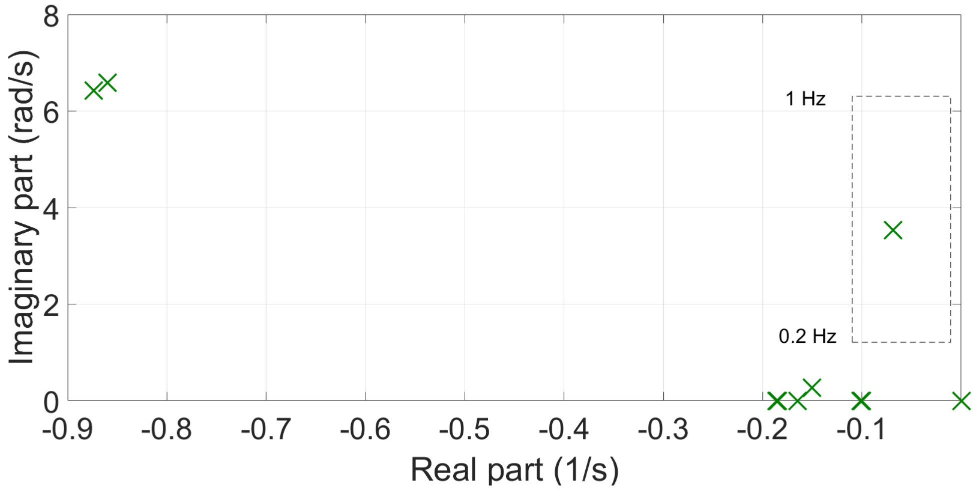

Figure 4.1. Eigenvalues of the linearized power system model.

Figure 4.1 shows that among the oscillatory modes, there is one inter–area mode with its corresponding eigenvalue being equal to $\lambda = -0.068 + j3.53$. The frequency of this mode is $f_{int} = 0.56$ Hz and it has a damping ratio of $\zeta = 1.93\%$.

Subsequently, simulation of the test system under a fault condition was realized. In steady state, area 1 exports 400 MW to area 2 and the tie–lines are equally loaded with $P_{7-8-1} = P_{7-8-2} = 200$ MW. Regarding the operating mode of the generator buses, generator 3 is the reference machine, i.e. it operates in PV mode whereas the rest operate in PQ mode. A worst–case scenario was implemented with the introduction of a three–phase short–circuit at line 8-9-2 at a distance of 11 km from BUS 9 (Figure 3.2) at $t_1 = 0.1$ s which was self–cleared at $t_2 = 0.25$ s without isolating the fault line. The resulting speeds of the four generators are plotted below:

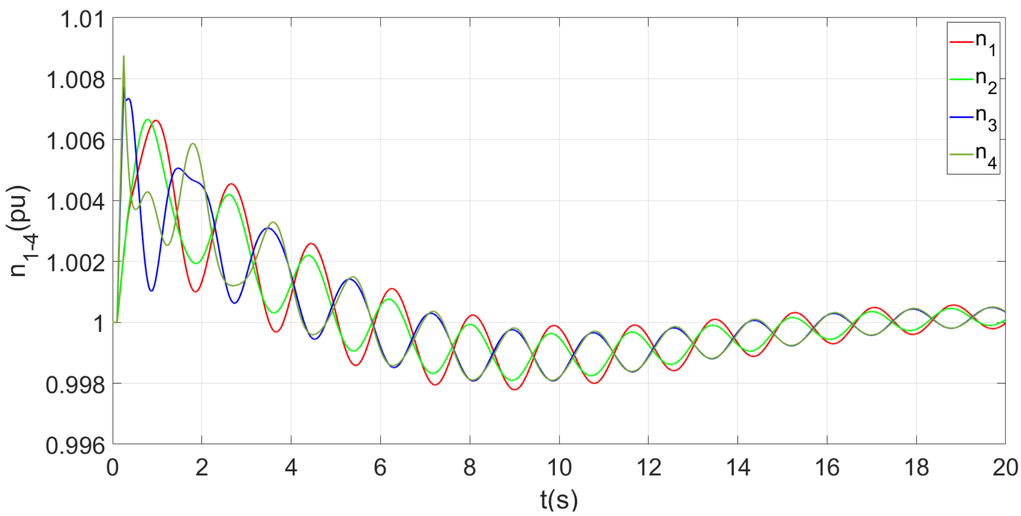

Figure 4.2. Generator speeds following the disturbance.

The presence of inter–area mode can be clearly observed from Figure 4.2, where the per unit speeds of the four generators are plotted. More specifically, the generator speeds n_1 and n_2 are almost in anti-phase with n_3 and n_4, meaning that the generators of area 1 oscillate against those of area 2. The frequency of the inter-area oscillations is $f = 0.56\,\text{Hz}$, a result that coincides with the one obtained from the modal analysis.

The transient stability performance of the system is also depicted in Figures 4.3 and 4.4, where the active power of tie–line 1 P_{7-8-1} and the rotor angle of generator 1 relative to generator 3 δ_{13} are presented. It can be seen that the oscillations decay after a long period of almost 50 s due to the low value chosen for the PSS units of the four generators.

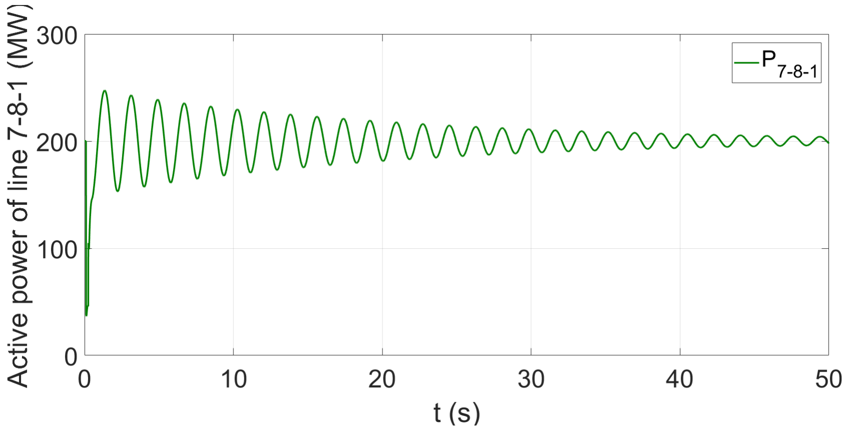

Figure 4.3. Active power flow of the AC tie–line 1 following the disturbance.

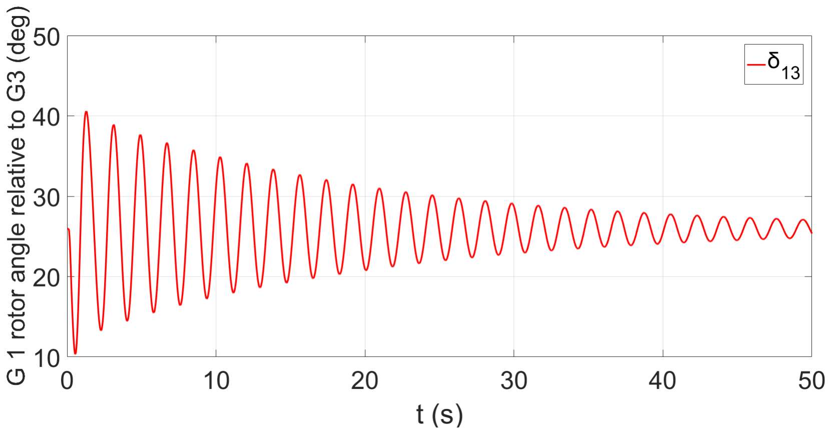

Figure 4.4. Generator 1 rotor angle (relative to generator 3) following the disturbance.

Next, an HVDC system incorporating the supplementary POD controller was connected in parallel with the two–area system in order to improve the damping of the inter–area oscillations.

4.2 Test system 2: Two–area system incorporating the HVDC link

This section presents the two–area test system incorporating the HVDC link. Initially, the POD controller design was done through the utilization of modal analysis and afterwards its performance was tested via time–domain simulations.

4.2.1 POD design

The PtP HVDC system was initially connected in parallel with the two–area test system without the POD control functionality activated and modal analysis was performed. In this case, the frequency of the interarea mode is equal to $f_{int} = 0.6\,\text{Hz}$. It slightly differs from the one recorded previously for the two–area test system because the topology characteristics have changed with the addition of the HVDC link. Nevertheless, the damping ratio is still low, i.e. $\zeta = 2.4\%$, highlighting the need for the use of the supplementary controller.

The design procedure of the auxiliary POD controller utilizes the residue based tuning method with the aim of choosing the optimum controller parameters, as analyzed in [5]. Based on Equation 4.1, it is evident that as long as the modes are shifted further to the left half–plane, i.e. the more negative their real part is, the more damping is achieved for a certain frequency. To this end, the POD controller is employed and ideally it should shift the eigenvalue to the left and at the same time maintain the frequency at a constant value in order to damp the mode of interest. To achieve this, the design procedure that was followed is given next.

Initially, the POD controller block (Figure 2.26) was integrated into the main control without the lead–lag blocks. The washout filter constant was set equal to $T_w = 10\,\text{s}$, meaning that the frequency components which are higher than 0.6 Hz pass unchanged (Figure 4.5). The damping gain was set equal to $k_d = 0$. For $k_d = 0$, by applying modal analysis, the respective eigenvalue was found equal to $\lambda_1 = -0.093 + j3.8$, whereas by increasing the gain to $k_d = 0.1$, $\lambda_2 = -0.085 + j3.85$ was obtained. The eigenvalues are plotted in Figure 4.6 and based on their values, the residue angle was calculated equal to $\theta_R = -82^o$. Thus, the compensating angle that needs to be provided by the lead–lag filters can be calculated as:

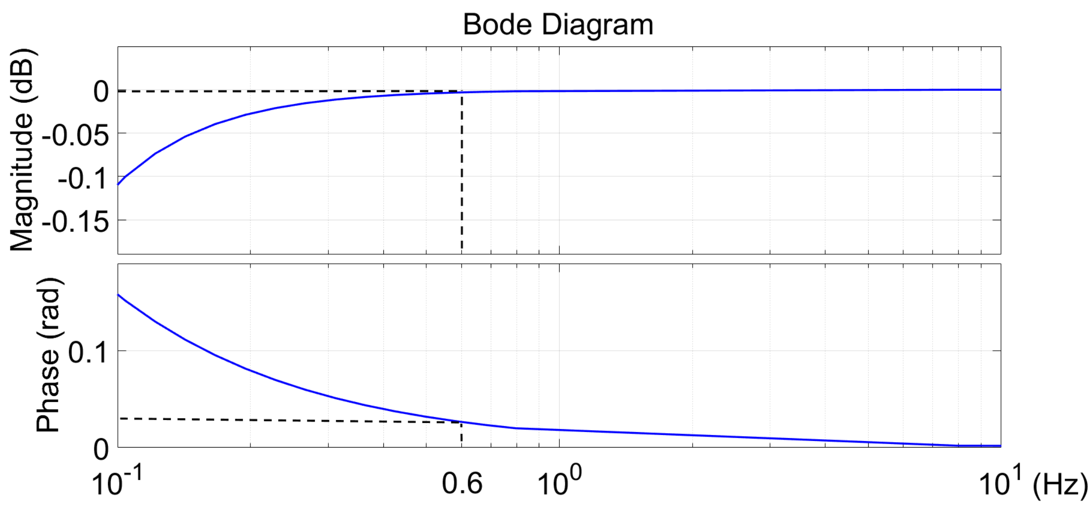

Figure 4.5. Bode diagram of the washout filter.

$$\theta_C = -180^o - \theta_R \tag{4.2}$$

which yields $\theta_C = -98^o$. The number of needed compensation stages (lead–lag filters) N depends on this angle, as suggested in [5]:

$$\begin{cases} N = 1 & \theta_C \leq 60^o \\ N = 2 & \theta_C \leq 140^o \end{cases}$$

Since $\theta_C = -98^o = 262^o$, N=3 is chosen. Therefore, the parameters of the lead–lag filter blocks were calculated based on Equations 4.3, 4.4, 4.5 [5]:

$$a = \frac{1 - sin(\frac{\theta_C}{N})}{1 + sin(\frac{\theta_C}{N})} \tag{4.3}$$

$$T_{lag} = \frac{1}{\omega_{int}\sqrt{a}} \tag{4.4}$$

$$T_{lead} = aT_{lag} \tag{4.5}$$

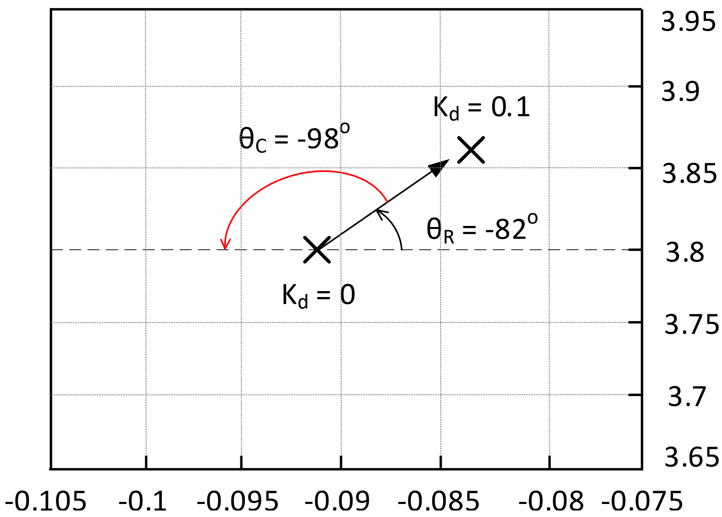

Figure 4.6. Residue's phase angle estimation for POD controller design.

By substituting N=3, $\omega_{int} = 2\pi f_{int}$ (where $f_{int} = 0.6\,\text{Hz}$) and $\theta_C = -98^o$ into the above Equations, the lead and lag time constants were found equal to $T_{lead} = 0.144\,\text{s}$ and $T_{lag} = 0.482\,\text{s}$ respectively. Next, by introducing the lead–lag blocks (with the calculated parameters) into the POD controller and applying modal analysis again, the new eigenvalue was found equal to $\lambda_3 = -0.48 + j3.78$, with the damped frequency equal to 0.6 Hz and a damping ratio of 12.53%. This means that the POD controller has shifted the eigenvalue to the left half of the complex plane, providing increased damping and preserving constant frequency.

Next, in order to choose the proper damping gain value, $k_d = 0.1$ was used as a starting point and its value was gradually increased. The shifting of the eigenvalue was monitored through modal analysis. As long as the gain was increasing, the eigenvalue was shifted to the left leading to increased damping but at the same time its frequency was observed to be slightly decreased. Therefore, the selected value for the damping gain was $k_d = 0.25$

which corresponds to an eigenvalue equal to $\lambda_3 = -1.23 + j3.56$ with a damped frequency equal to 0.57 Hz and a damping ratio of 33.2%. At the same time, the effect of the increase in k_d was observed through time domain simulations under the fault condition that was described in the previous section. More specifically, by observing the active power flow of line 7-8-1, it was concluded that further increase from this value did not have significant effect on the damping of the oscillations, thus leading to the choice of $k_d = 0.25$.

4.2.2 Simulation studies for the assesment of the POD performance

The time domain simulations are next presented. They were realized in addition to the modal analysis in order to assess the performance of the designed POD controller regarding the damping of the inter-area oscillations. Similar to the previous case, area 1 exports 400 MW to area 2, with the total active power of the HVDC link being equal to $P_{DC} = 200\,\text{MW}$ at converter 1 terminal, whereas the tie–lines are equally loaded with $P_1 = P_2 = 100\,\text{MW}$. Figures 4.7, 4.9 and 4.11 present the active power output of the POD controller as well as the active power flows in the positive pole of the DC line and line 7-8-1, with and without the use of the designed POD controller. For comparison purposes, Figures 4.8, 4.10, 4.12 are also given with the aim of highlighting the impact of the POD damping gain.

Figures 4.7 and 4.8 show that when the short–cicuit occurs, the POD controller detects the variation of the active power P_{7-8-1} (which is used as an input to the controller) and modifies its active power output ΔP appropriately.

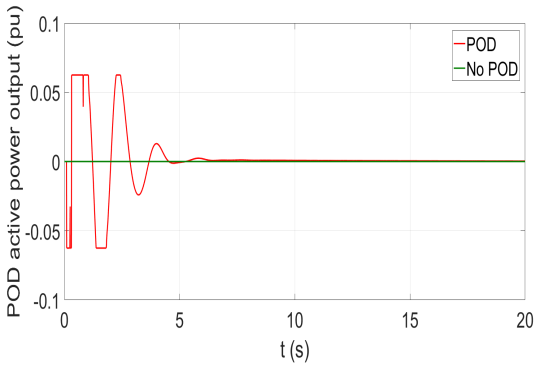

Figure 4.7. Active power output of the POD controller for $k_d = 0.25$.

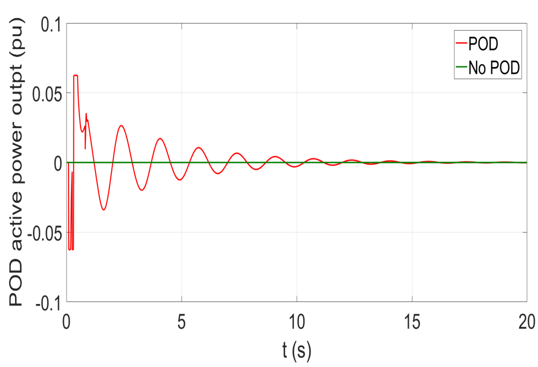

Figure 4.8. Active power output of the POD controller for $k_d = 0.05$.

The POD active power output oscillates with the frequency of the interarea oscillations, whereas it limits were set to 0.0625 pu (i.e. 25 MW with $P_{base} = 400\,\text{MW}$), thus allowing high level of contribution from the supplementary controller, as suggested in [22]. Therefore, the active power reference of converter 1 is modified by the amount of ΔP, thus resulting in the modification of the DC link active power flow, as Figures 4.9 and 4.10 depict. This results in an improved damping for the oscillations of the active power in the AC inter–tie lines copared to the situation in which no POD was applied, as can be clearly concluded from Figures 4.11 and 4.12. For the two different damping gain values, i.e. $k_d = 0.25$ and $k_d = 0.05$, it can be seen that the power oscillations are damped and the active power returns to each pre–disturbance value within almost 5 s and 15 s respectively.

Finally, the generator speeds are plotted in Figure 4.13 for the case of $k_d = 0.25$. By comparing it to Figure 4.2, it can be seen that the addition of the POD leads to faster

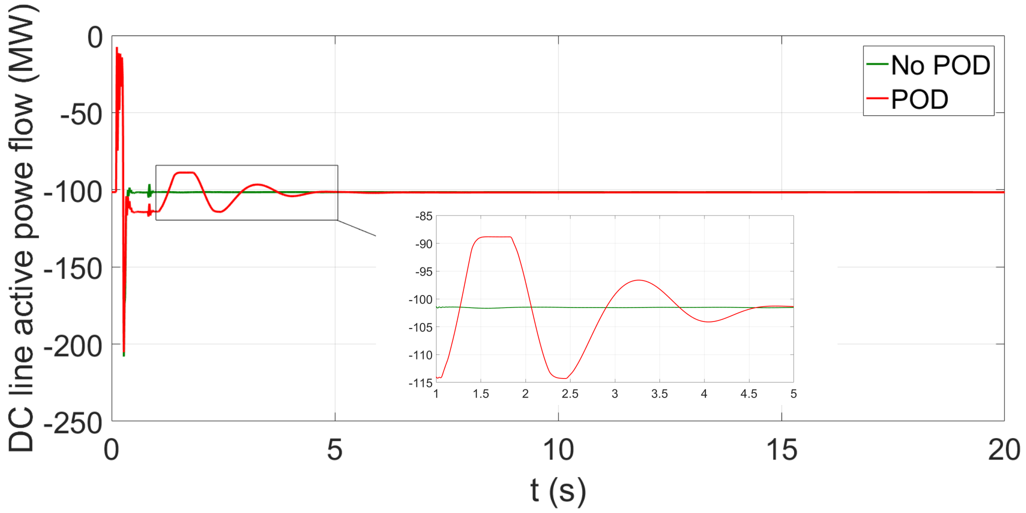

Figure 4.9. Active power flow at the positive DC onshore bus of converter 1 for $k_d = 0.25$

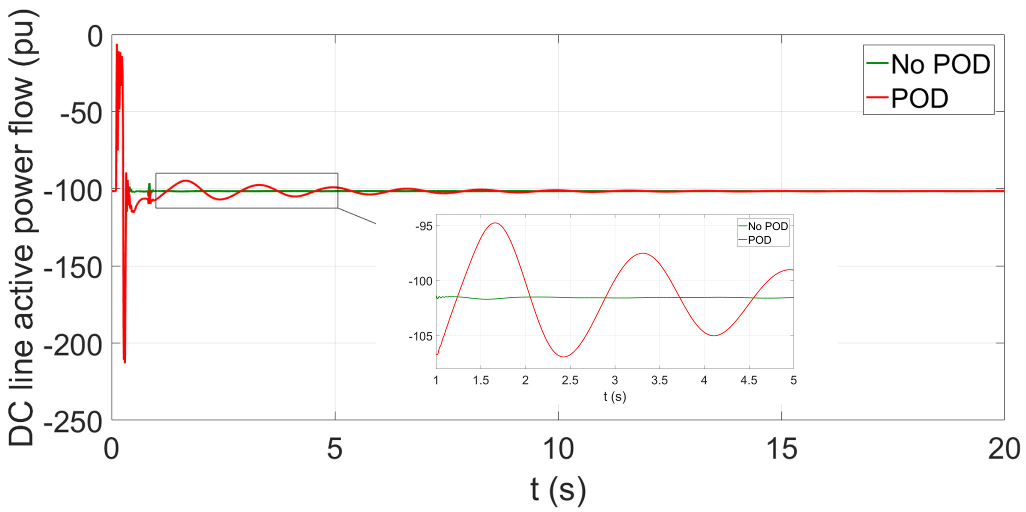

Figure 4.10. Active power flow at the positive DC onshore bus of converter 1 for $k_d = 0.05$

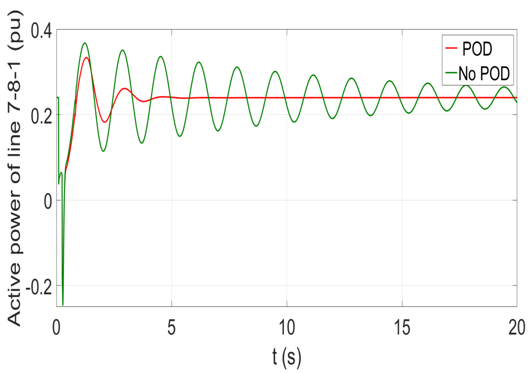

Figure 4.11. Active power flow at line 7-8-1 for $k_d = 0.25$.

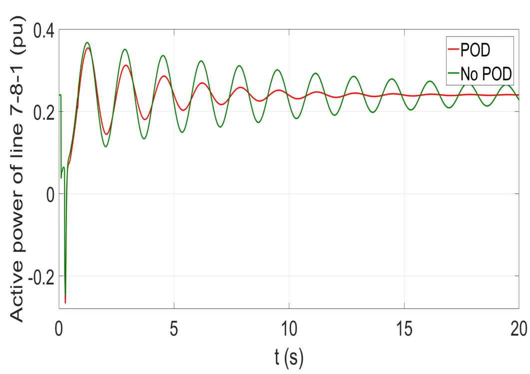

Figure 4.12. Active power flow at line 7-8-1 for $k_d = 0.05$.

interarea mode damping, since the speeds are in phase approximately after 5 s. Similar conclusions can be drawn by observing Figure 4.14, where it is shown that the relative rotor angle of generator 1 to generator 3 restores to its pre–fault value, i.e. 11.26^o, within almost 5s.

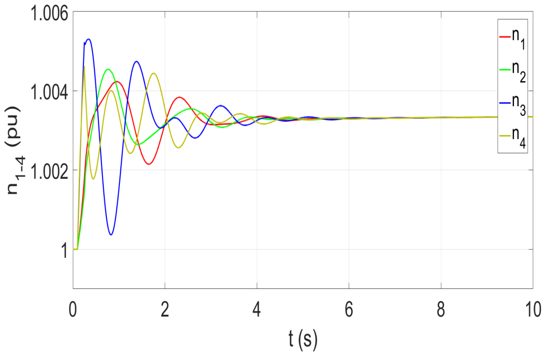

Figure 4.13. Generator speeds of G1–G4 for $k_d = 0.25$.

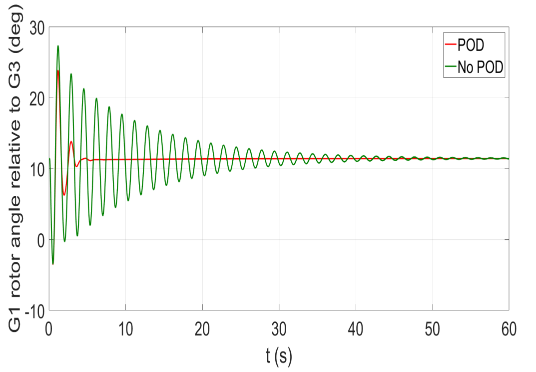

Figure 4.14. G1 rotor angle (relative to G3) with and w/o POD for $k_d = 0.25$.

4.3 Test system 3: Expanded MTDC system

In the context of this section, different simulation scenarios were created by varying the offshore wind power profile in order to investigate the impact of the offshore terminal into the POD control behaviour. The section is divided into two subsections based on the control mode of the two MMC units. Subsection 4.3.1 presents the obtained simulation results with converters 1 and 2 operating in P–Q and V_{DC}–V_{AC} control mode respectively (master–slave mode). Subsequently, the control mode was changed to DC voltage droop, with a single POD controller applied to converter 1, as presented in subsection 4.3.2. For all cases examined, the offshore controller was set to control the AC voltage V_{AC} and the frequency f of the offshore converter AC terminal (OC) respectively (its operation is explained in more details in section A.2 of Appendix). At this point, the topology of the three terminal HVDC system used for the following simulations is repeated below:

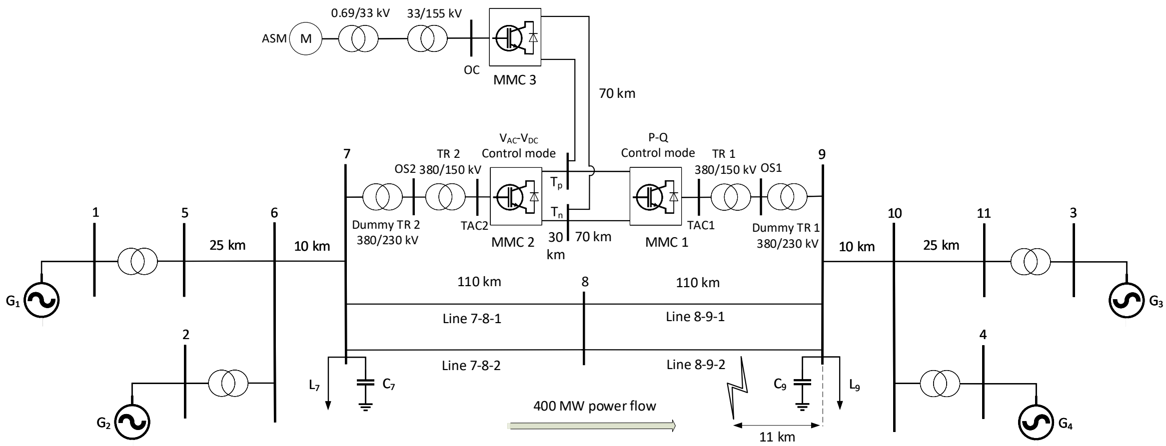

Figure 4.15. Two–area test system incorporating the three terminal HVDC system.

4.3.1 P-Q and V_{DC}–V_{AC} control modes

In this case, converters 1 and 2 were set to P–Q and V_{DC}–V_{AC} control mode respectively. The POD controller was applied to converter 1. Regarding its damping gain value, $k_d = 0.05$ was chosen in order to make the impact of the added offshore terminal more observable since with $k_d = 0.25$ the damping of the oscillations was shown to be very fast, i.e. they were damped within around 5 s.

4.3.1.1 Constant power production

Initially, a constant wind farm active power production was assumed. Modal analysis followed by non–linear time domain simulations was performed for five different values of wind power output. The amount of output power was increased from 0 to 400 MW with steps of 100 MW. At the same time, the amount of the generated active power from generator G1 was decreased in each case with the aim of keeping the power flow through line 7-8-1 (and thus the total exported active power from area 1 to area 2) constant, i.e. almost 95 MW so that the damping of the power oscillations between the different cases can be comparable. The damping ratio without the addition of the POD controller (ζ') as well as with the POD applied (ζ) was calculated. Table 4.1 summarizes the obtained results.

Table 4.1. Power oscillation damping for different constant wind power profiles

Active power (MW)						Damping ratio	
Wind farm	G_1	G_2	G_3	G_4	**Line 7-8-1**	$\zeta'(\%)$	$\zeta(\%)$
Case 1: 0	700	700	711.9	700	95.6	4.75	9.93
Case 2: 100	595	700	710.3	700	96.3	5.5	10.6
Case 3: 200	488	700	712.1	700	95.4	6.39	11.4
Case 4: 300	382	700	714.5	700	94.2	7.4	12.3
Case 5: 400	280	700	714.4	700	94.2	8.45	13.24

The addition of the wind farm means that some amount of active power previously produced by generator G1 is now substituted by the wind production. Thus, the decreased production of the generator leads to increased damping performance, since the lower level of produced active power from G1 facilitates the damping of its electromechanical oscillations. Moreover, comparing the damping ratios ζ' and ζ for the five cases under study, it can be seen that the obtained damping ratio is increased by almost 5% when the POD controller is incorporated into the system.

Figure 4.16 compares the damping provided in the active power flow of line 7-8-1 for three different values of wind power production P_w, while Figure 4.17 presents the corresponding POD active power output for each of the three cases. As it was also concluded from the results obtained by the modal analysis, the highest damping ratio value is obtained for case 5, where it can be seen that the magnitude of the power oscillations in Line 7-8-1 is the lowest, since the production from generator G1 is the lowest one, i.e. 280 MW.

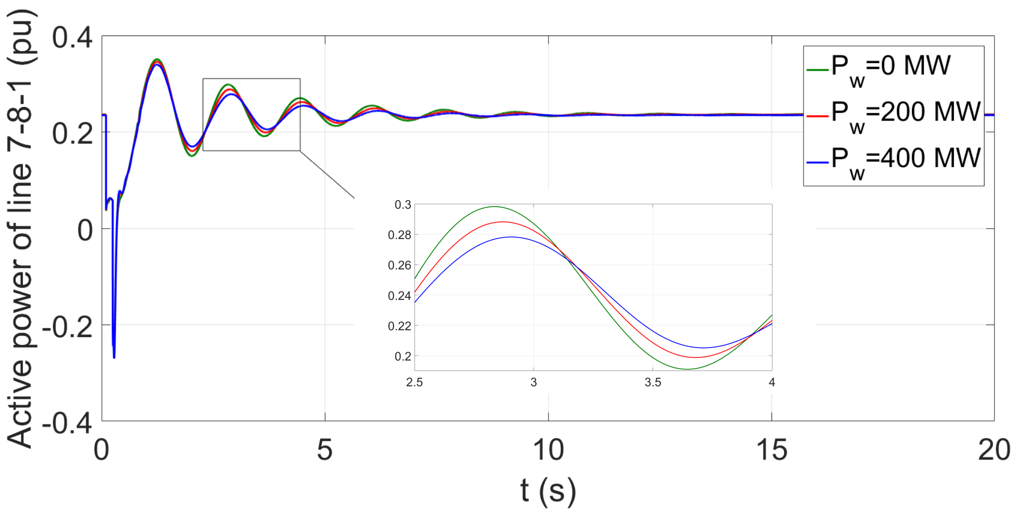

Figure 4.16. Active power of line 7-8-1 for three different wind power profiles

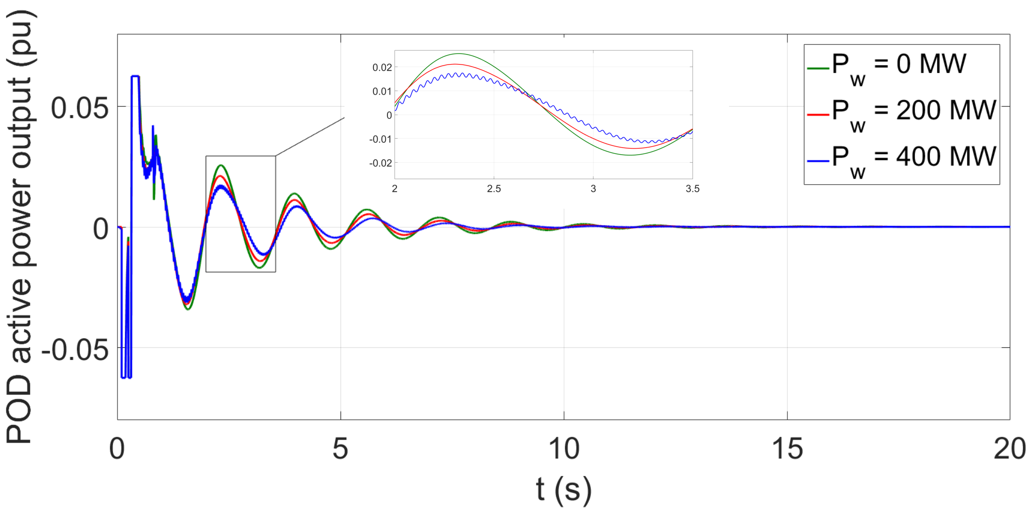

Figure 4.17. Active power output of the POD controller for three different wind power profiles

4.3.1.2 Increasing power production

The influence of ramping up the wind power production on the damping performance is investigated within this subsection. Since in this case the wind power output is not constant in the entire range of simulations, the modal analysis technique cannot be utilized in order to measure the damping ratio since the operating point of the system is constantly changing. Alternatively, the latter can be estimated from the waveform graphs, as will be shown below. The wind farm output power was increased from 20 to 405 MW for all three cases under study considering different ramp up rates for each case, as can be seen in Figure 4.18.

The initial operating point for the generators of the system G_1–G_4 is depicted in Table 4.2. Different time instants were selected for the introduction of the three–phase fault at each case (Figure 4.18) so that the oscillations are introduced at the same level of active power flow at line 7-8-1 for all three cases, i.e. $P_{7-8-1,ft} = 0.271\,\text{pu} = 110\,\text{MW}$. Thus, it

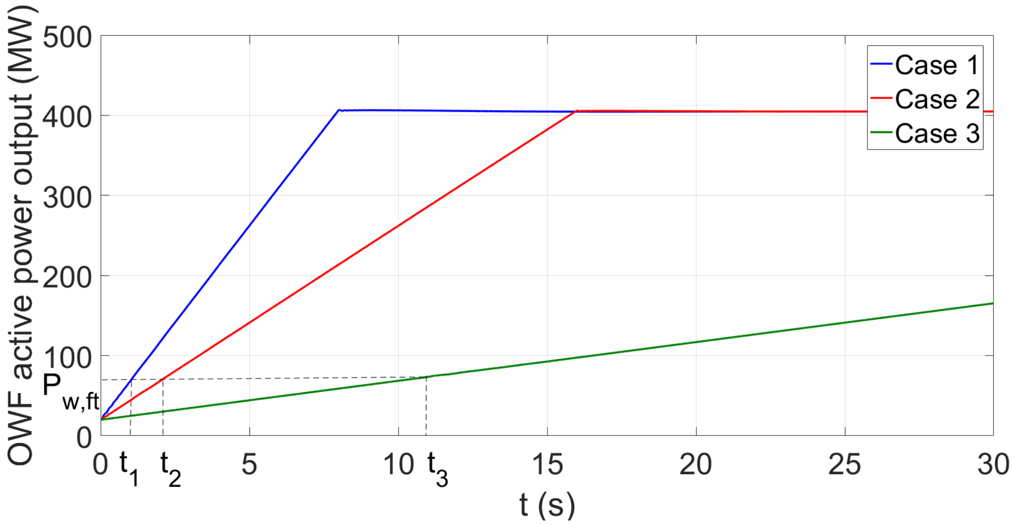

Figure 4.18. Wind farm active power output for cases 1–3.

was made possible to draw conclusions regarding the impact of the different ramp up rate. The fault was self–cleared after 150 ms.

Table 4.2. Initial operating point for the system's generators

Active power (MW)					
Wind farm	G_1	G_2	G_3	G_4	**Line 7-8-1**
20	680	700	710.5	700	96.3

Table 4.3 summarizes the damping ratio results for three wind power profiles with different ramp up rate. It is worth of mentioning that the selected cases under study represent three extreme cases rather than realistic wind power profiles since the ramp up rates are very big. However, this approach allows for shorter simulation time without loss of generality regarding the effect of the increasing wind production on the damping of the electromechanical oscillations.

Table 4.3. Power oscillation damping for the increasing wind power output profiles

Wind power ramp up rate (MW/s)		**Fault time (s)**	**damping ratio ζ(%)**
Case 1	48.125	1	11.8
Case 2	24.06	2.3	10.46
Case 3	4.75	11	10.06

Figure 4.19 presents the active power waveform of line 7-8-1 for case 1. In order to calculate the damping ratio, Equations 4.6 and 4.7 were utilized:

$$\sigma = \ln(\frac{dp_1}{dp_2}) \tag{4.6}$$

$$\zeta = \frac{1}{\sqrt{1 + (\frac{2\pi}{\sigma})^2}} \tag{4.7}$$

where dp_1 and dp_2 are represented by the black line segments of Figure 4.19 and their values can be calculated from the graph. More specifically, the line segment dp_i is calculated as the difference between the i^{th} peak value of the oscillatory active power waveform and the active power waveform without the presence of the fault. Furthermore, the damped frequency can be calculated according to Equation 4.8:

$$f_d = \frac{1}{T_d} \tag{4.8}$$

where T_d is the period of oscillations. For all three cases the frequency of oscillations is around 0.6 Hz.

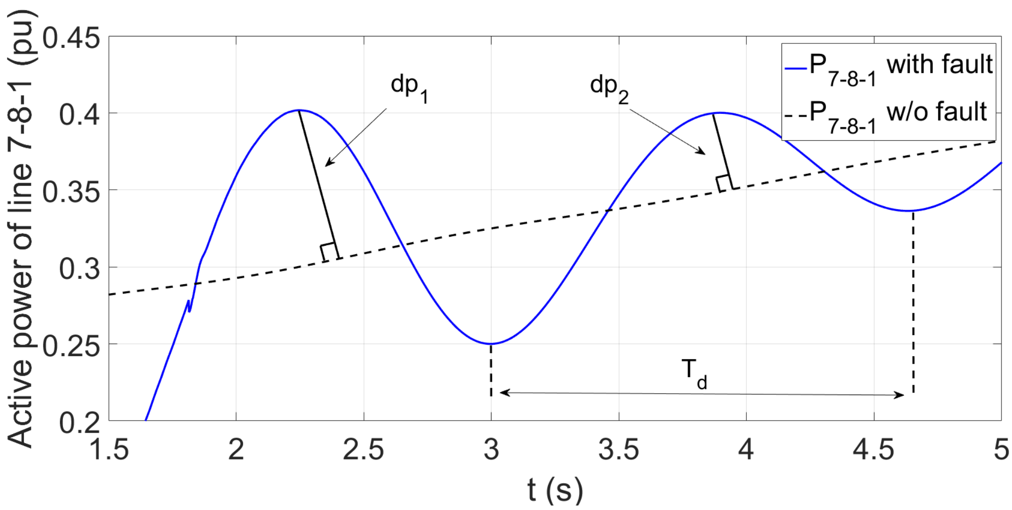

Figure 4.19. Damping in the active power oscillations at line 7-8-1 for case 1.

The damping ratio for cases 2 and 3 can be calculated in a similar way. Figure 4.20 presents a comparison of the damping performance for the three different wind power profiles while Figure 4.21 presents the output of the POD controller. Although straightforward conclusions cannot be drawn from the graph since the improvement in damping is not clearly observable, the results of Table 4.3 show that as long as the slope of the wind power ouput is increasing, the amount of damping of the electromechanical oscillations is also increased.

Furthermore, Figure 4.22 presents the DC voltage at the terminals of MMC 2 for each case. It can be seen that there is an overvoltage of almost 10% during the fault duration, whereas the voltage experiences an instantaneous voltage dip of 15% after the release of the fault. The DC voltage then experiences a 2% overvoltage for cases 1 and 2 before settling to its reference.

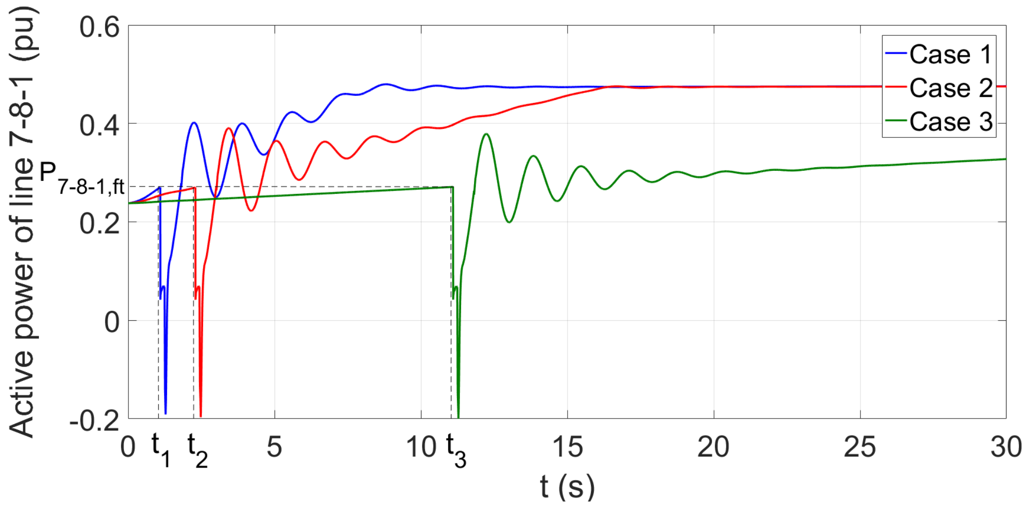

Figure 4.20. Comparison of the damping in the active power oscillations at line 7-8-1 for cases 1–3.

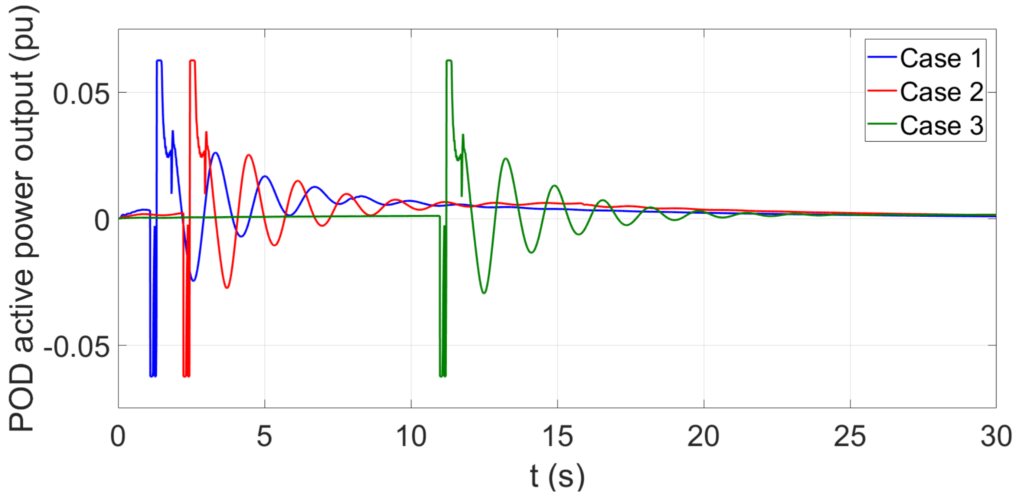

Figure 4.21. POD output for cases 1–3.

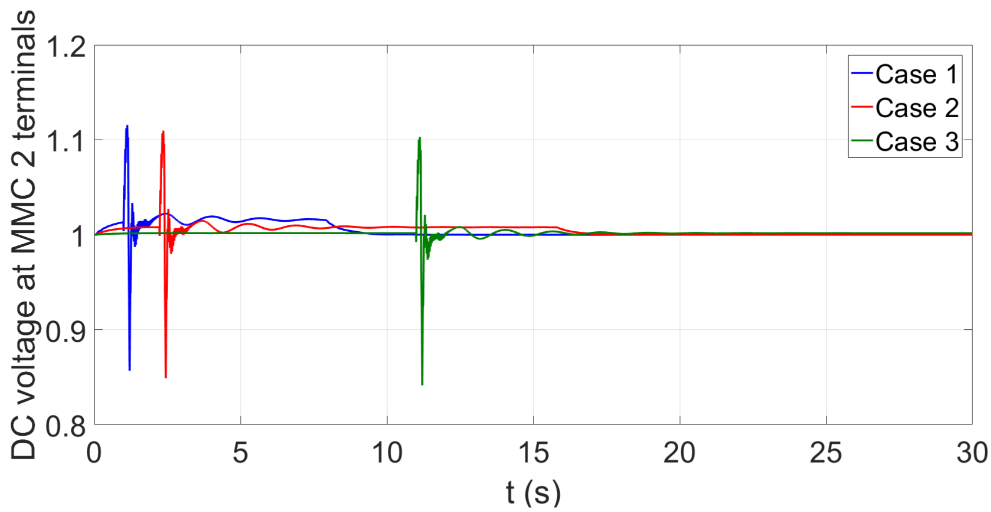

Figure 4.22. DC voltage magnitude at MMC 2 terminals for cases 1–3.

4.3.1.3 Decreasing power production

In this case, the wind power production was ramped down from 400 to 20 MW. Similar to the case of the increasing production, three wind power profiles with different ramp down rates were simulated (Figure 4.23).

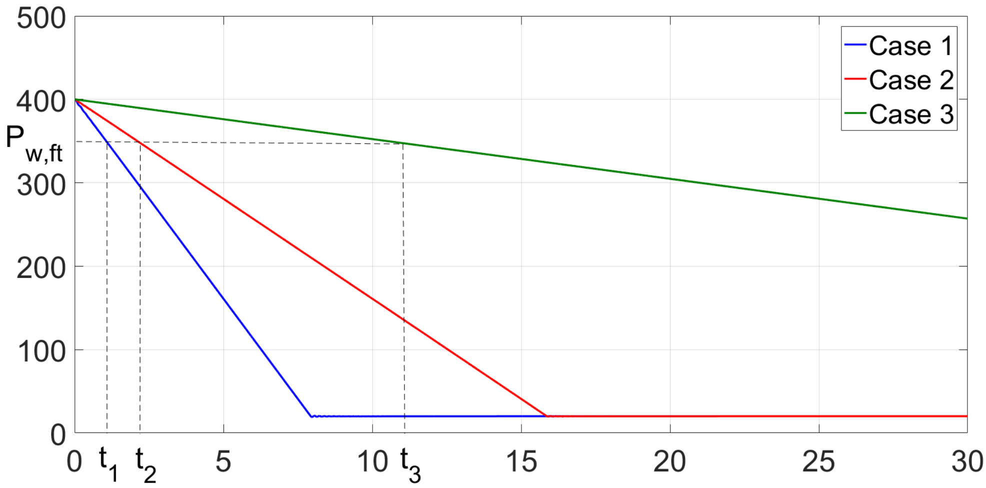

Figure 4.23. Wind farm active power output for cases 1–3.

The initial active power production of the generators is depicted in Table 4.4. For each case, the three–phase fault was introduced at the time instant in which the level of power flow at line 7-8-1 is equal to 0.203 pu, i.e. 82 MW. Table 4.5 summarizes the damping ratio results whereas the active power flows of line 7-8-1 are plotted in Figure 4.24 for each of the three cases. Based on the obtained results, it can be concluded that slower decrease rates of the wind production lead to increased damping.

Table 4.4. Initial operating point for the system's generators

Active power (MW)					
Wind farm	G_1	G_2	G_3	G_4	**Line 7-8-1**
400	280	700	712	700	94.2

Table 4.5. Power oscillation damping for the decreasing wind power output profiles

Wind power ramp down rate (MW/s)		**Fault time (s)**	**damping ratio ζ(%)**
Case 1	47.5	1.1	12.11
Case 2	23.81	2.24	12.46
Case 3	4.75	11	13.67

Additionally, comparing the results for the damping ratios between Tables 4.3 and 4.5, it can be observed that increased damping performance is obtained in the second case, i.e. for decreasing wind power profiles. A comparison between Figures 4.18 and 4.23 can provide an explanation for this result. In particular, in case of the decreasing wind power profile, the contribution of the wind farm $P_{w,ft}$ is bigger (and thus the production of generators is smaller) when the fault occurs, thus leading to improved damping performance.

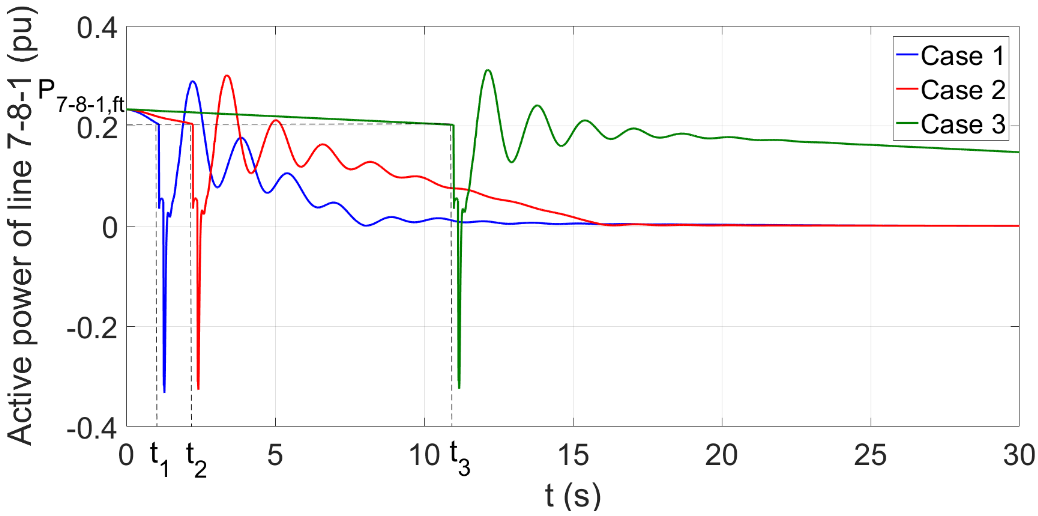

Figure 4.24. Comparison of the damping in the active power oscillations at line 7-8-1 for cases 1–3.

4.3.1.4 Wind farm outage

Finally, a wind outage event was simulated in order to test the performance of the POD controller. The fault event occured at $t = 1\,\text{s}$ for two different wind power profiles, as depicted in Table 4.6.

Table 4.6. Power oscillation damping for two wind farm outage events

Active power (MW)						damping ratio
Wind farm	G_1	G_2	G_3	G_4	**Line 7-8-1**	$\zeta(\%)$
Case 1: from 100 to 0	595	700	712	700	96.3	9.47
Case 2: from 400 to 0	280	700	705.5	700	94.2	0.89

The resulting active power flow at line 7-8-1 can be seen in Figure 4.25 for both cases. In case 1, the POD controller provides adequate damping in the interarea oscillations caused by the outage event since the obtained damping ratio value is $\zeta = 9.47\%$, close to the one obtained for zero wind power production (Table 4.1). However, in case 2 where the drop in the wind power output is higher, the dampring ratio is considerably decreased to $\zeta = 0.89\%$.

Figures 4.26, 4.27 compare the active power response of the four generators G1–G4 to the outage event. For case 2, the generators have to compensate for much higher loss of power compared to case 1, thus increasing their production with higher rate. This introduces oscillations of higher amplitude and the system presents more oscillatory behaviour until the generators settle to their new operating point.

4.3.2 DC voltage droop control mode

The POD performance was examined with the MMCs operating in DC voltage droop control mode and the POD controller being applied in MMC1, as previously. To this end,

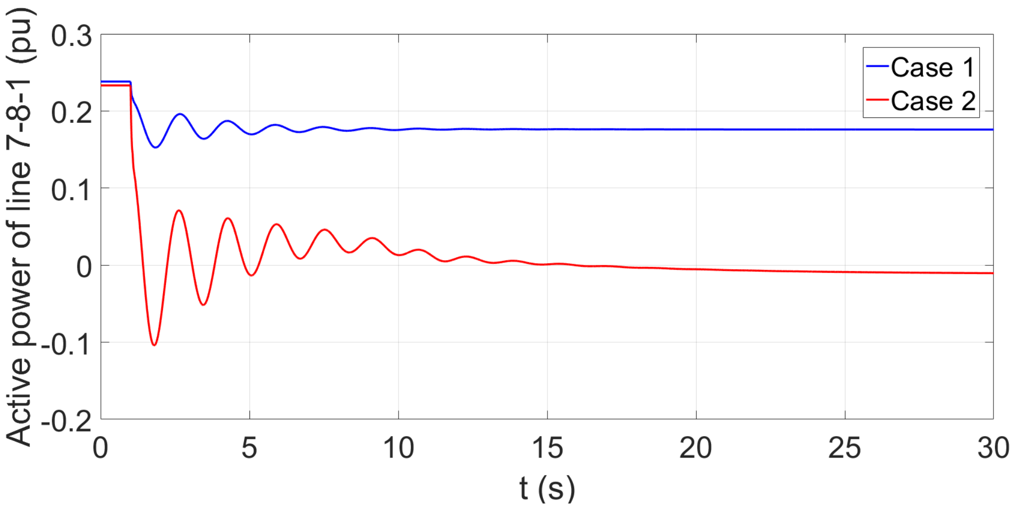

Figure 4.25. Damping in the active power oscillations at line 7-8-1 for the two wind farm outage events.

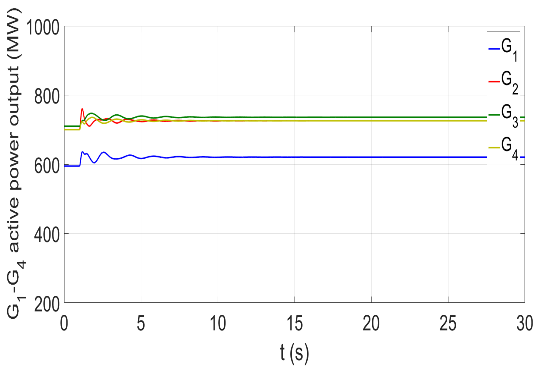

Figure 4.26. Generated active power of G1–G4 for case 1.

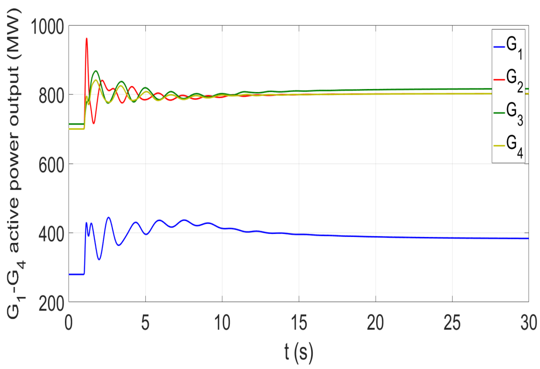

Figure 4.27. Generated active power of G1–G4 for case 2.

the control loops for the two converters were modified as shown in the block diagram of Figure 4.28 which can be expressed by the following formulas:

$$V_{DC1} = V_{DC1,ref} - k_{dr1} \cdot (P_{AC1,ref} - P_{AC1} + \Delta P) \tag{4.9}$$

$$V_{DC2} = V_{DC2,ref} - k_{dr2} \cdot (P_{AC2,ref} - P_{AC2}) \tag{4.10}$$

where ΔP is the output of the POD controller which is applied only in one side, i.e. in MMC1, as stated above. Equations 4.9 and 4.10 are the droop control formulas and state that the converter DC voltage is modified based on the deviation of the active power from its reference. Figure 4.29 presents the droop curve and the curves related to the system limits, briefly explained below [7]:

- DC voltage: The upper limit of the DC voltage is determined by the insulation level of the switching components or the connected DC equipment. The lower limit depends on a limitation of the modulation index, the converter topology and the converter control implementation.

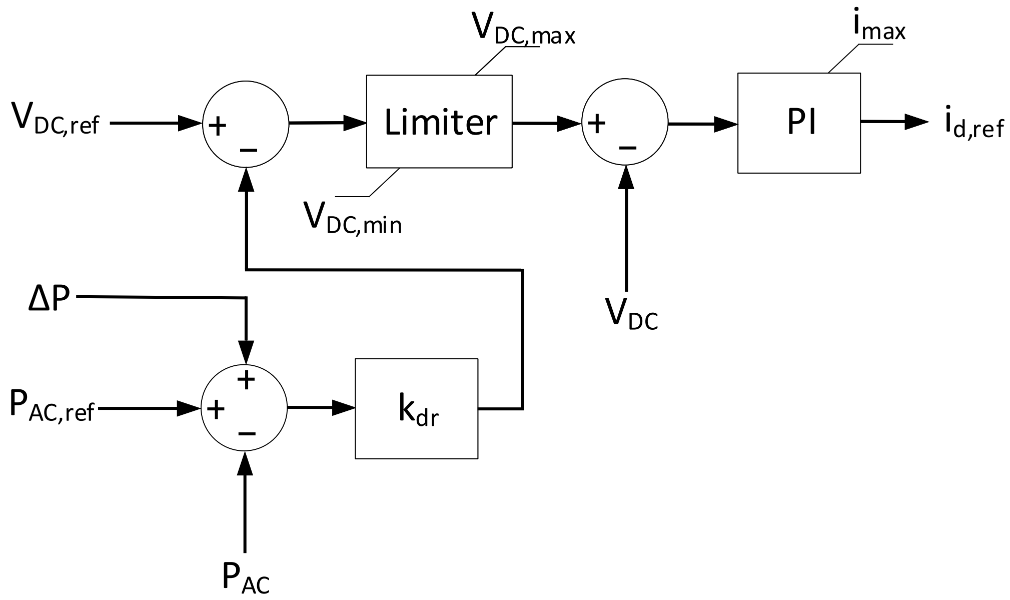

Figure 4.28. DC voltage droop control.

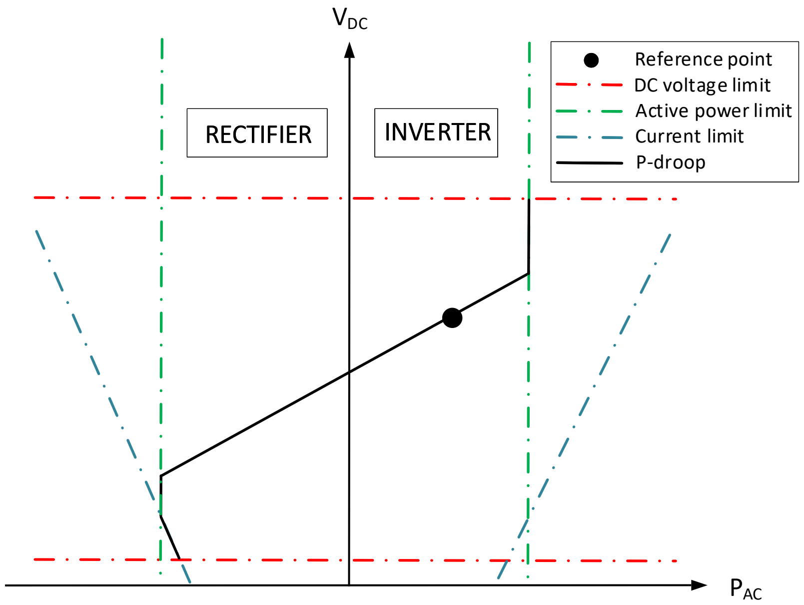

Figure 4.29. $P_{AC} - V_{DC}$ curve for DC voltage droop control.

- Active power: It is limited by the semiconductor current limit which limits the power (for a constant AC voltage).
- DC current: Its limit is based on the current rating of the connected DC components.

Table 4.7 presents the limits of the onshore converters MMC1 and MMC2 related to the maximum and minimum DC voltage, the maximum AC current, the maximum AC voltage (TAC1 and TAC2 terminals at Figure 4.15) and the maximum AC active power which is derived as the product of i_{max} and v_{max}. Regarding the offshore converter MMC3, its limits related to the DC voltage, AC current and AC voltage (OC terminal at Figure 4.15) are given in Table 4.8.

Table 4.7. Limits of the onshore converters

Variables(pu)	**MMC1**	**MMC2**
$v_{DC,max}$	1.05	1.05
$v_{DC,min}$	0.95	0.95
$i_{AC,max}$	1.1	1.1
$v_{AC,max}$	1.15	1.15
$p_{AC,max}$	1.265	1.265

Table 4.8. Limits of the offshore converter

Variables(pu)	**MMC3**
$v_{DC,max}$	1.05
$v_{DC,min}$	0.95
$i_{AC,max}$	0.7
$i_{AC,min}$	-0.7
$v_{AC,max}$	1.1
$v_{AC,min}$	-0.1

The POD performance was initially tested by applying an increasing wind power profile and afterwards a constant wind power profile was considered. The ramp up as well as the constant wind power profiles are the same as in case 2 from Table 4.3 and 4.1 respectively, in which the system was operated in master–slave mode. The damping ratio values for these cases have been calculated previously and they are given in Table 4.9.

Table 4.9. Power oscillation damping for increasing and constant wind power profiles when the converters operate in master–slave mode

Active power (MW)						**damping ratio**
Wind farm	G_1	G_2	G_3	G_4	**Line 7-8-1**	$\zeta(\%)$
Case 1: from 20 to 400	680	700	712.1	710.5	96.3	10.46
Case 2: 100	595	700	710.3	700	96.3	10.6

Regarding the increasing wind farm profile, two different scenarios were studied. In scenario A, converter 1 operated as inverter and converter 2 was in rectifier mode when the fault occured. In scenario B, the output of the wind farm was modified such that both converters operate as inverters in the fault time. More specifically, the wind farm output power was ramped up to 400 MW for both scenarios and the initial operating point for the generators of the system is given in Table 4.10. The POD capability was finally tested for the constant wind power production of $P_w = 100\,\mathrm{MW}$ (Scenario C). Then, the calculated damping ratio values for Scenario A were compared to the damping ratio obtained in case 1 (10.46%), whereas the POD performance in Scenario C was compared to case 2 (10.6%).

Table 4.10. Initial operating point of the system generators for DC voltage droop control mode and three different wind profiles.

Active power (MW)					
Wind farm	G_1	G_2	G_3	G_4	**Line 7-8-1**
Scenario A: 20	680	700	710.5	700	96.3
Scenario B: 200	488	700	710.5	700	95.4
Scenario C: 100	595	700	710.3	700	96.3

4.3.2.1 MMC 1 in inverter mode and MMC 2 in rectifier mode

Initially, the wind farm output was ramped up from 20 to 400 MW with a ramp up rate equal to 24 MW/s, as depicted in Figure 4.30 :

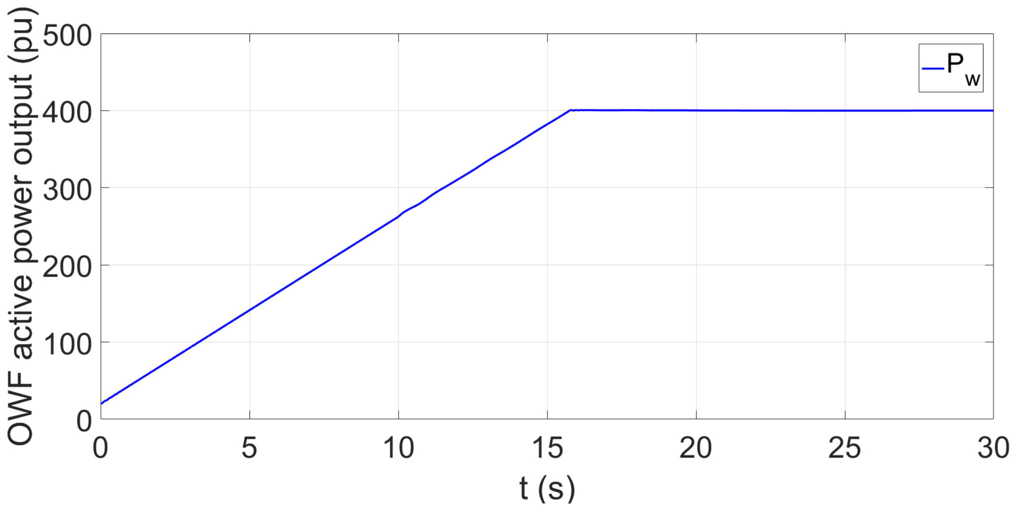

Figure 4.30. Wind farm active power output for scenario A.

By varying the droop gains for the two converters, five different cases were simulated as can be seen in Table 4.11. Again, the fault time instant is chosen in such a way that the active power flow through line 7-8-1 is the same for all cases under study when the fault occurs, i.e. 0.24 pu or 96 MW.

Table 4.11. Cases under study for scenario A.

Cases under study	Fault time(s)	k_{dr1}	k_{dr2}
Case A1	10	0.05	0.05
Case A2	2	0.1	0.05
Case A3	1	0.05	0.1
Case A4	1	0.02	0.07
Case A5	1	0.1	0.01

Figures 4.31–4.34 present the AC side active power flow as well as the DC voltage at the DC terminals of MMC1 and MMC2 for case A1. It can be seen that as long as the wind power output is increased, the active power flow through MMC1 is also increased from 0.5 pu or 200 MW to 0.995 pu or 382 MW while the DC voltage also rises to 1.018 pu,

following the droop curve of Figure 4.35. For MMC2 which operates in rectifier mode, the active power flow is gradually decreased leading to the increase of the DC voltage. The droop characteristic curves for the two converters are given in Figures 4.35 and 4.36. The damping ratio was calculated equal to 5.06%.

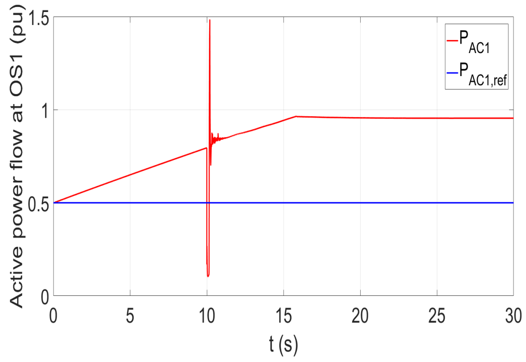

Figure 4.31. Measured active power at OS1 for case A1.

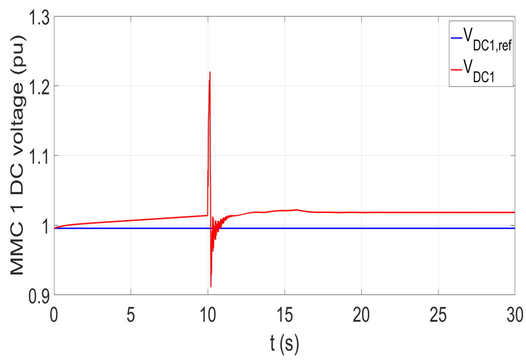

Figure 4.32. Measured DC voltage at MMC1 DC terminals for case A1.

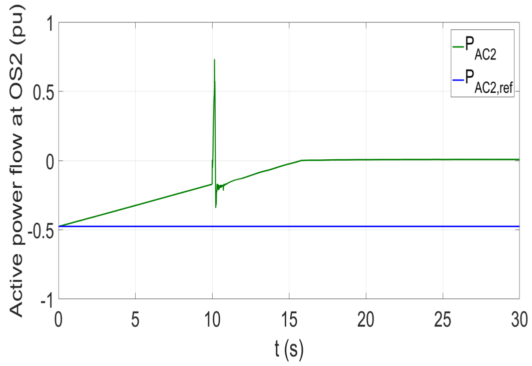

Figure 4.33. Measured active power at OS2 for case A1.

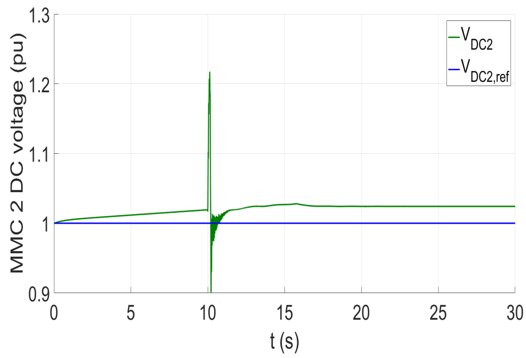

Figure 4.34. Measured DC voltage at MMC2 DC terminals for case A1.

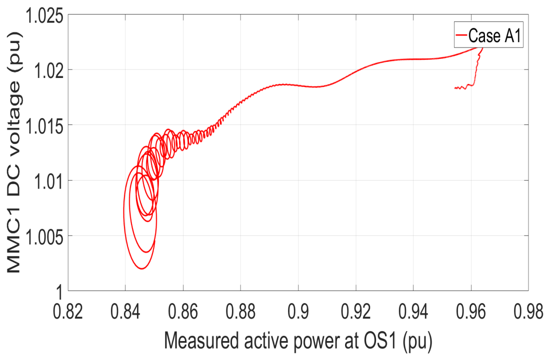

Figure 4.35. P–V_{dc} droop curve of MMC1 for case A1.

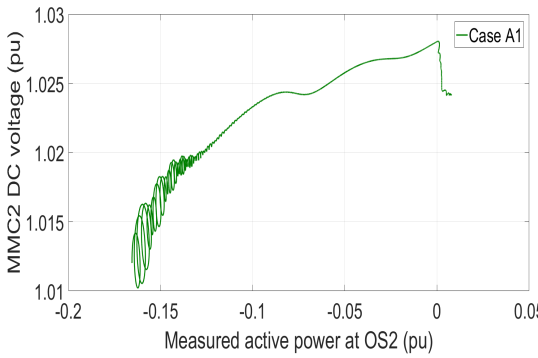

Figure 4.36. P–V_{dc} droop curve of MMC2 for case A1.

Subsequently, the droop gain of MMC1 was increased to $k_{dr1} = 0.1$ while the droop gain of MMC2 was kept constant at $k_{dr2} = 0.05$. In this case, the resulting active power flows and DC voltages are plotted in Figures 4.37–4.40 for the two converters. It can be observed that the active power sharing has changed due to the higher value chosen for the droop gain k_{dr1}, thus leading to a decreased active power flow through converter 1. The droop characteristic curves for the two converters are given in Figures 4.41 and 4.42. In this case, the increased value for the droop gain k_{dr1} resulted in increased damping ratio value which was calculated equal to 6.29%.

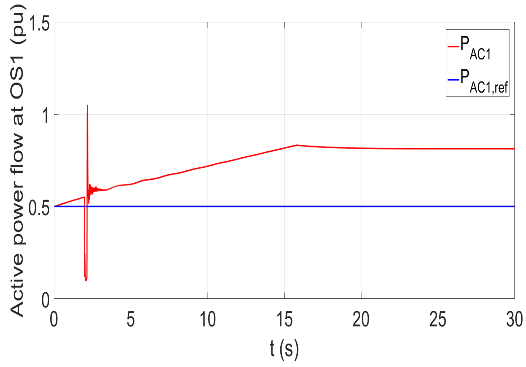

Figure 4.37. Measured active power at OS1 for case A2.

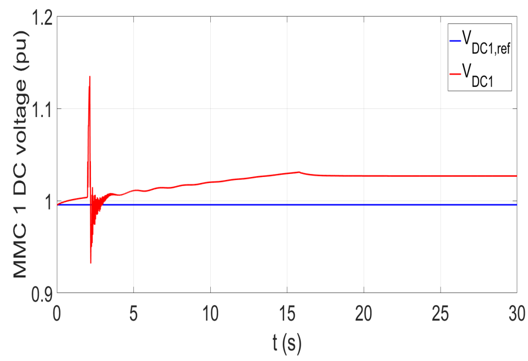

Figure 4.38. Measured DC voltage at MMC1 DC terminals for case A2.

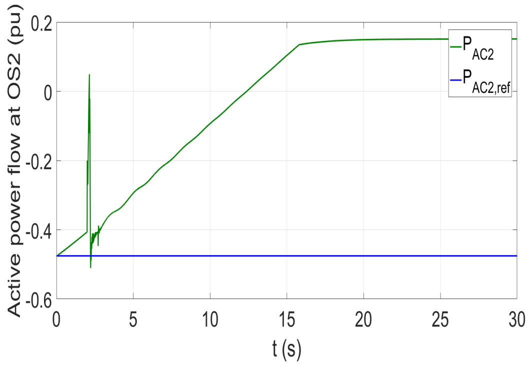

Figure 4.39. Measured active power at OS2 for case A2.

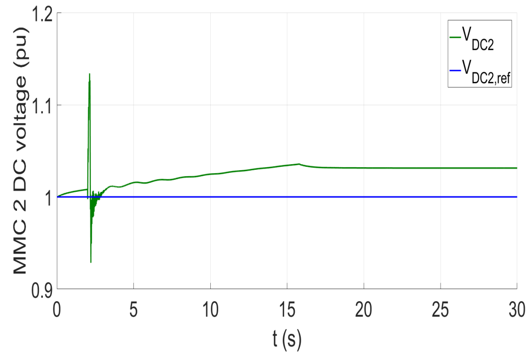

Figure 4.40. Measured DC voltage at MMC2 DC terminals for case A2.

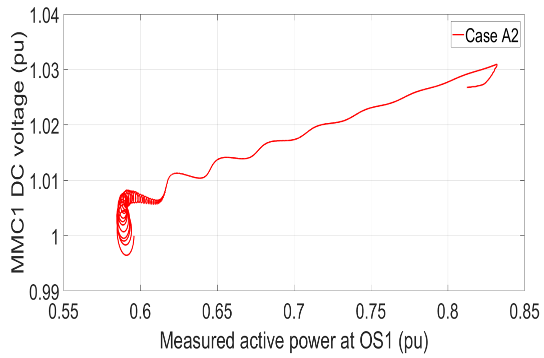

Figure 4.41. P–V_{dc} droop curve of MMC1 for case A2.

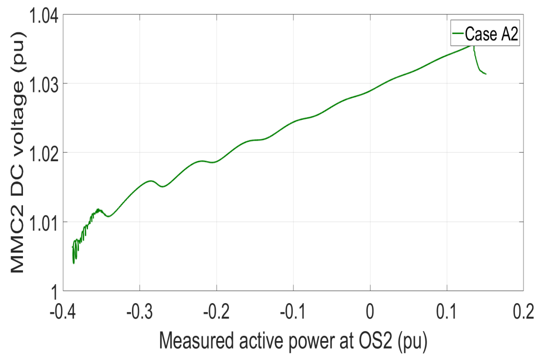

Figure 4.42. P–V_{dc} droop curve of MMC2 for case A2.

In the third case under study, the droop gain value of MMC2 was chosen bigger than MMC1, i.e. $k_{dr1} = 0.05$ and $k_{dr2} = 0.1$, resulting in much higher power flow through MMC1 compared to MMC2, as can be seen in Figures 4.43–4.46. The droop characteristic curves for the two converters are given in Figures 4.47 and 4.48. In this case the worst damping performance was obtained compared to cases A1 and A2 since the damping ratio value was calculated equal to $\zeta = 4.77\%$.

At this point, the active power flows of line 7-8-1 for cases A1–A3 are given in Figure 4.49

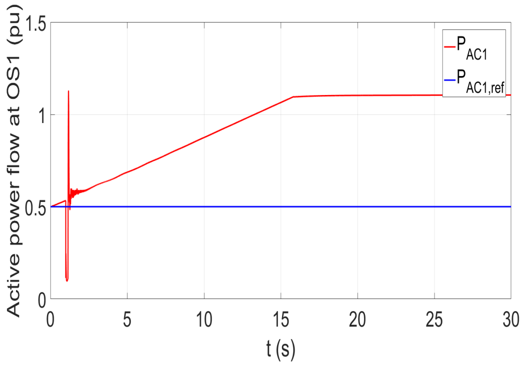

Figure 4.43. Measured active power at OS1 for case A3.

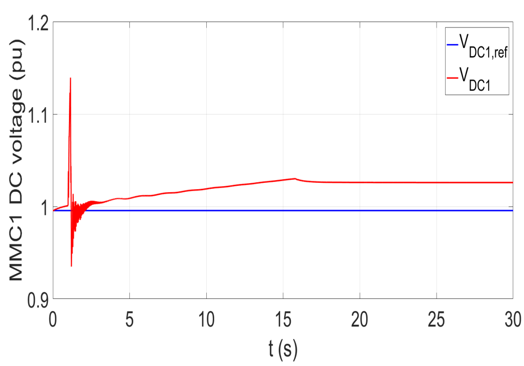

Figure 4.44. Measured DC voltage at MMC1 DC terminals for case A3.

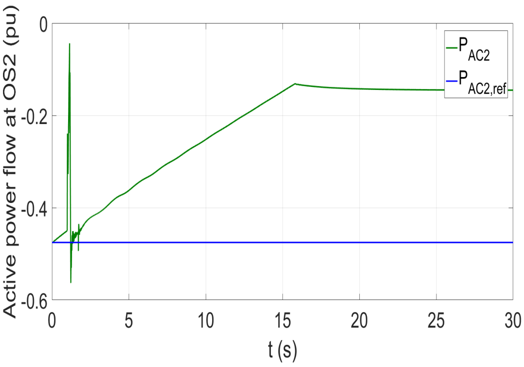

Figure 4.45. Measured active power at OS2 for case A3.

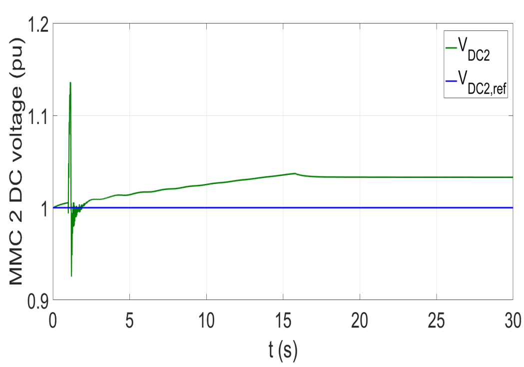

Figure 4.46. Measured DC voltage at MMC2 DC terminals for case A3.

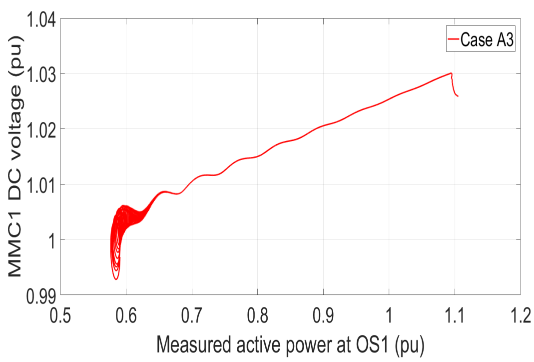

Figure 4.47. P–V_{dc} droop curve of MMC1 for case A3.

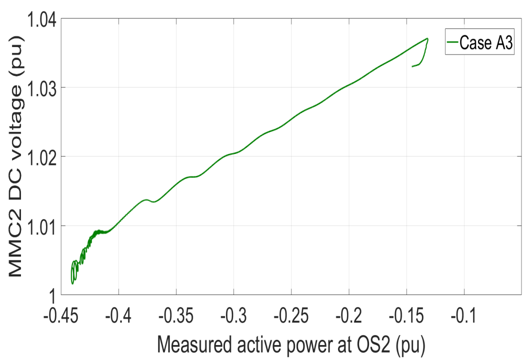

Figure 4.48. P–V_{dc} droop curve of MMC2 for case A3.

and the resulting damping ratios are listed in Table 4.12 from the lowest to the highest value. Comparing the damping ratio results obtained from cases A1–A3, the following conclusions can be drawn: The highest damping ratio is obtained in case A2, i.e. when the droop gain of converter 1 is bigger than the droop gain of converter 2. Furthermore, the damping ratio is improved as long as k_{dr1} is getting bigger for constant k_{dr2} (from case A1 to A2), whereas it is deteriorated as long as k_{dr2} is increased for constant k_{dr1} (from case A1 to A3). To further validate these conclusions, two more cases were considered. In case A4, both droop gains were decreased by the same amount compared to case A3 and the damping ratio was deteriorated by 0.66%, showing that the decreased k_{dr1} affected the damping ratio value more than the reduction in k_{dr2}, leading to an overall decreased damping performance. In case A5, k_{dr1} was kept constant and k_{dr2} was reduced compared to case A2. The reduction in k_{dr2} had positive effect in the damping of the power oscillations since the damping ratio was increased almost by 2%, i.e. $\zeta = 8.18\%$.

The effect of changing the value of k_{dr1} on the damping performance can be explained based on Figure 4.28, where it can be seen that the droop gain of converter 1 is multiplied with the output of the POD controller ΔP. This means that the POD output is lowered for lower values of k_{dr1}, thus leading to decreased damping performance. On the contrary, as long as the damping gain is getting bigger, the overall gain of the POD is also getting bigger, thus improving the damping of the oscillations.

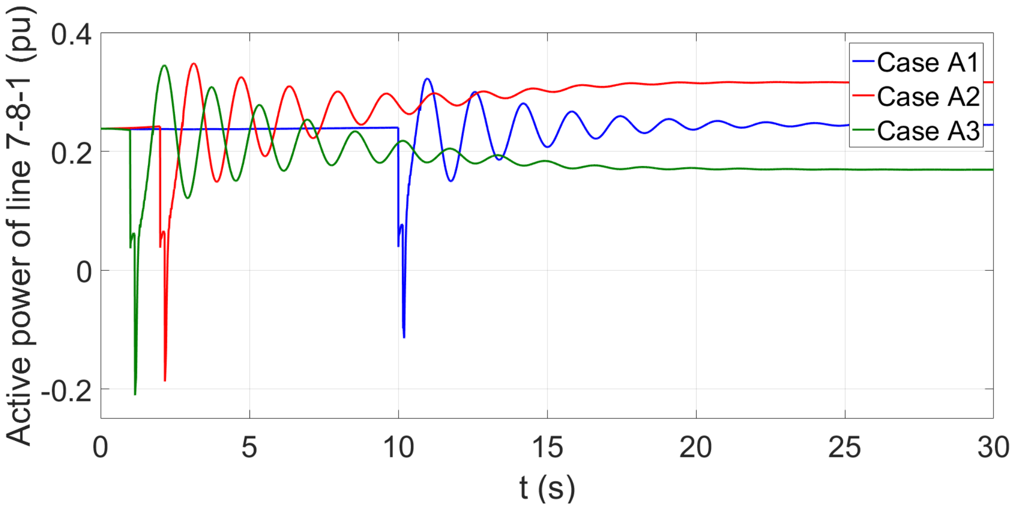

Figure 4.49. Active power flow through line 7-8-1 for cases A1–A3.

Finally, a comparison between the results obtained in this section and case 1 of Table 4.9 shows that the amount of damping is decreased when the control mode is switched from master–slave to DC voltage droop control mode.

Table 4.12. Power oscillation damping ratio for the cases under study.

Cases under study	Fault time(s)	k_{dr1}	k_{dr2}	$\zeta(\%)$
Case A4	1	0.02	0.07	4.11%
Case A3	1	0.05	0.1	4.77%
Case A1	10	0.05	0.05	5.06%
Case A2	2	0.1	0.05	6.29%
Case A5	1	0.1	0.01	8.18%

4.3.2.2 MMC 1 and MMC 2 in inverter mode

The wind farm output was ramped up from 200 to 400 MW, as depicted in Figure 4.50. Thus both converters operated as inverters from the beginning. The resulting damping ratios can be seen in Table 4.13, where the droop gains have the same values as in cases A1-A3. In this case , only the DC voltage and the active power for case B2 are plotted (Figures 4.51–4.54). It can be observed that both converters operate in inverter mode since the active power flow is positive at OS1 and OS2. The increase of active power leads to the increase of the DC voltage, following the droop control characteristic of Figure 4.29.

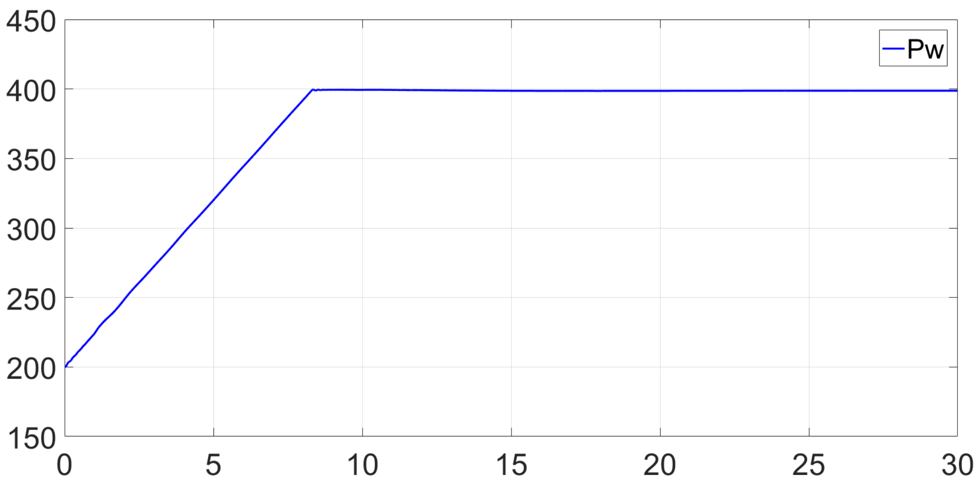

Figure 4.50. Wind farm active power output for scenario B.

Table 4.13. Power oscillation damping ratio for five different cases for scenario B.

Cases under study	k_{dr1}	k_{dr2}	$\zeta(\%)$
Case B3	0.05	0.1	6.61%
Case B1	0.05	0.05	7.65%
Case B2	0.1	0.05	8.67%

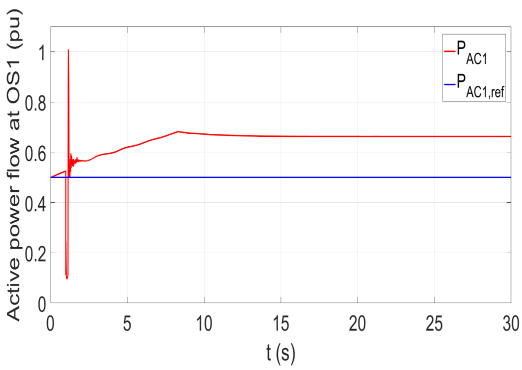

Figure 4.51. Measured active power at OS1 for case B2.

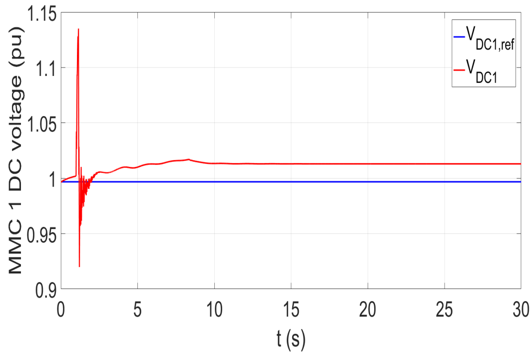

Figure 4.52. Measured DC voltage at MMC1 DC terminals for case B2.

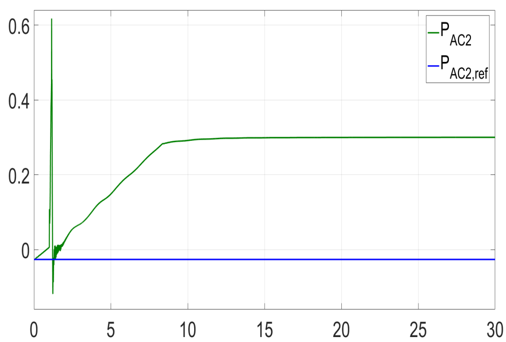

Figure 4.53. Measured active power at OS2 for case B2.

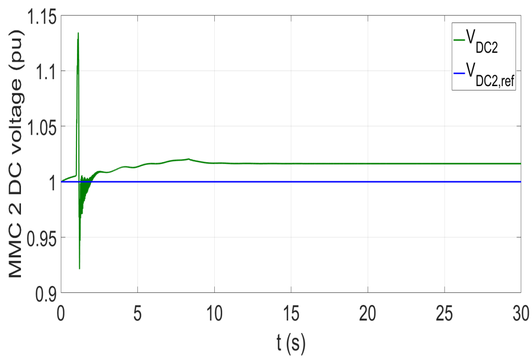

Figure 4.54. Measured DC voltage at MMC2 DC terminals for case B2.

Regarding the damping performance based on the droop gain relationship between the two converters, similar conclusions to scenario A can be drawn, i.e. the highest damping ratio is obtained for $k_{dr1} > k_{dr2}$, i.e. case B2. Moreover, comparing the damping ratios of Tables 4.12 and 4.13, it can be seen that they are increased by almost 2% for scenario B. This is an intuitive result, being into agreement with the conclusion reached in the previous section where the converters operated in master–slave mode. More specifically, it was shown that some amount of the active power of line 7-8-1 is now provided by the wind farm with the production of G1 and G2 being reduced and the latter has positive effect in the damping performance since it facilitates the damping of the electromechanical oscillations. Similarly, in scenario B, since converter 2 is in inverter mode, some amount of the power produced by the wind farm flows through line 7-8-1, with G1 and G2 thus reducing their production. Therefore, the damping ratio is increased compared to scenario A, where converter 2 operates as rectifier when the fault occurs, thus all the power through the AC intertie line is provided by G1 and G2.

4.3.2.3 Constant wind power production

The POD capability was tested under constant wind power output equal to $P_w = 100\,\text{MW}$. Five cases were examined with the droop gains having the same values as in cases A1–A5. The calculated damping ratio values can be seen in Table 4.14.

Table 4.14. Power oscillation damping ratio for five pairs of droop gain values when P_w=100 MW.

Cases under study	k_{dr1}	k_{dr2}	ΔP	$\Delta P'$	$\zeta(\%)$
Case C4	0.02	0.07	0.031	0.001	5.61
Case C3	0.05	0.1	0.031	0.001	5.85
Case C1	0.05	0.05	0.03	0.002	5.88
Case C2	0.1	0.05	0.029	0.003	6.27
Case C5	0.1	0.01	0.029	0.003	6.33

It can be observed that for all five cases there is a reduction in the damping ratio compared to the one obtained with master–slave control, i.e. $\zeta = 10.6\%$ (Table 4.9). This is because only a part of the POD output ΔP is added to the active power of converter 1 due to the droop control operation in contrast to the master–slave mode, where the total ΔP is added to the active power. This can be seen in Figures 4.55–4.58.

More specifically, Figure 4.55 presents the POD output for master–slave operation. From $t_1 = 1.973\,\text{s}$ to $t_2 = 2.321\,\text{s}$, it can be found that $\Delta P = 0.023\,\text{pu}$. Figure 4.56 presents the DC voltage of MMC1 versus the measured active power at Onshore Slack 1, where only the values from t_1 to t_2 have been plotted. By calculating the change in active power of MMC1 as the difference $\Delta P' = P_1(t_2) - P_1(t_1)$, $\Delta P' = \Delta P$ is obtained, meaning that the whole amount of the POD output is utilized for the damping of the oscillations. On the contrary, when the converters operate under DC voltage droop control mode, e.g. considering case C1, $\Delta P = 0.03\,\text{pu}$ while $\Delta P' = 0.001\,\text{pu}$, as Figures 4.57, 4.58 depict. This means that a very small amount of the POD output is utilized for the damping of the oscillations, thus leading to reduced damping, i.e. 5.88%.

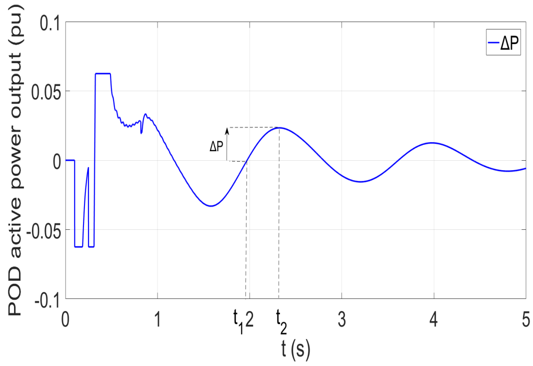

Figure 4.55. POD active power output for $P_w = 100\,\mathrm{MW}$ and operation in master–slave control mode.

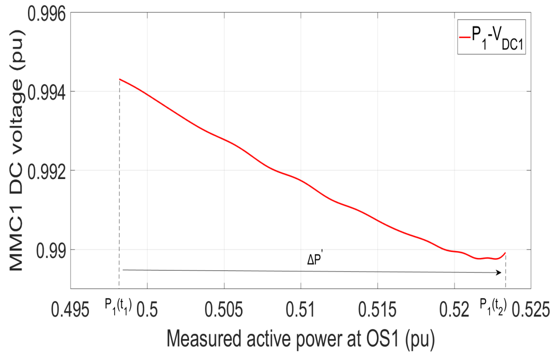

Figure 4.56. MMC1 P–V_{DC} curve for $P_w = 100\,\mathrm{MW}$ and operation in master–slave control mode.

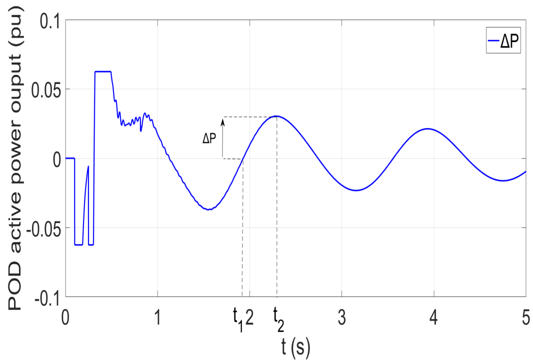

Figure 4.57. POD active power output for $P_w = 100\,\mathrm{MW}$ and operation in DC voltage droop control mode.

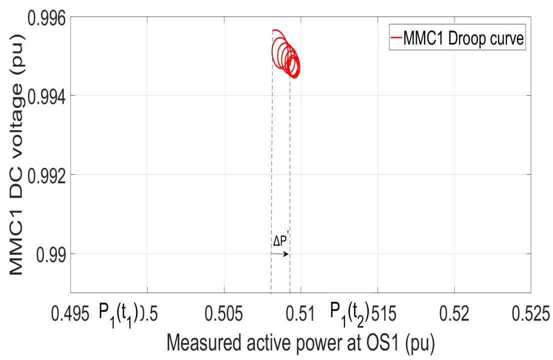

Figure 4.58. MMC1 droop curve for $P_w = 100\,\mathrm{MW}$ and operation in DC voltage droop control mode.

4.3.2.4 Compensation for the reduction in $\Delta P'$ for constant wind power production

In order to compensate the reduction caused by the droop gain, a gain k_c can be added such that when multiplied with the POD output, the whole ΔP is utilized for the damping of the electromechanical oscillations. The modified control block diagram is given in Figure 4.59.

In order to compensate for the reduction caused in case C1, the value of k_c was gradually increased and it was found that by choosing $k_c = 10.1$, $\Delta P' = \Delta P = 0.023\,\mathrm{pu}$ is obtained (Figure 4.60, 4.61). Therefore, by proper choice of the gain k_c, all the amount of the POD active power output was added to the active power of MMC1, thus being utilized for the damping of the electromechanical oscillations. This occurs similar to the case when the system operates in master–slave control mode.

However, even after the compensation, although the damping ratio is improved for the droop control, it is still lower compared to the one obtained for the system operating under master–slave operation. Figure 4.62 compares the active power measured at bus OS1 with and without the addition of the compensating gain k_c. It can be clearly observed that by adding the latter, a significantly larger $\Delta P'$ is obtained which, added to the active power,

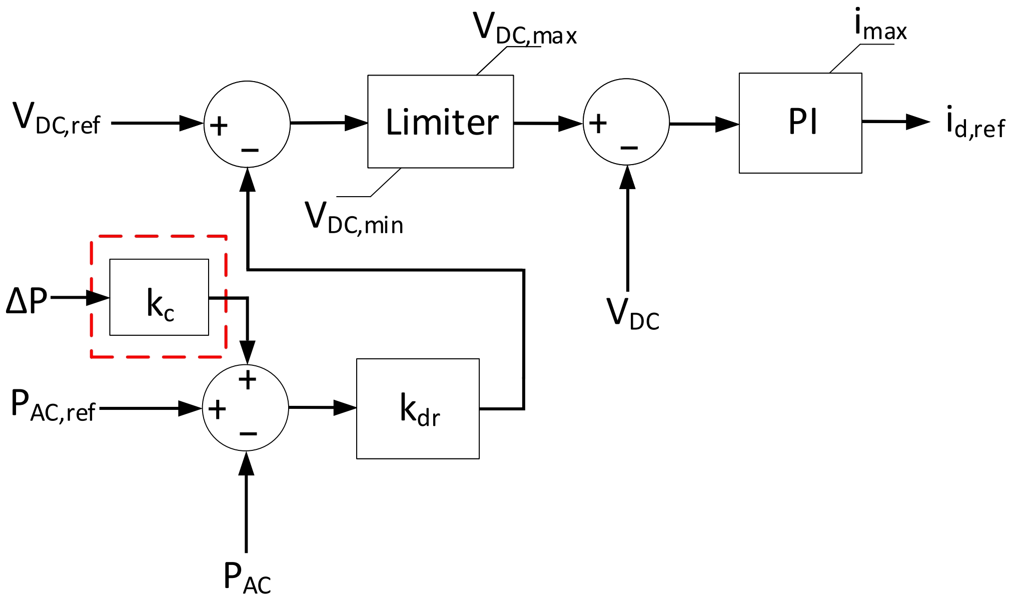

Figure 4.59. DC voltage droop control with the compensating gain k_c added.

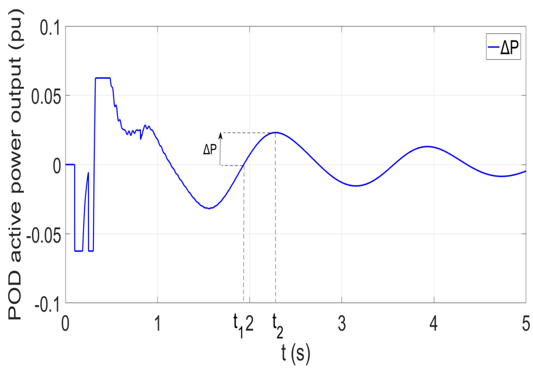

Figure 4.60. POD active power output for $P_w = 100\,\text{MW}$.

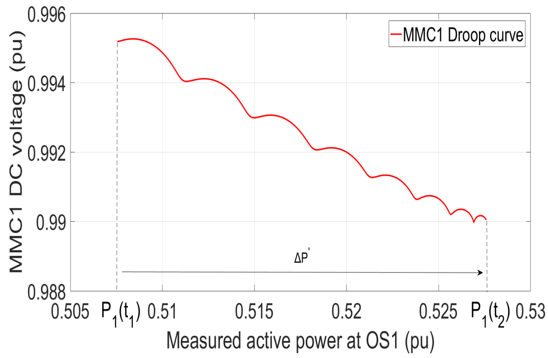

Figure 4.61. MMC1 droop curve for $P_w = 100\,\text{MW}$.

results in increased damping.

For the rest four cases, the compensating gain was selected based on an iterative process until $\Delta P' = \Delta P$. The damping ratios were calculated and the results are summarized in Table 4.15. A considerable improvement in the damping performance can be observed by comparing the damping ratio values to those of Table 4.14. Moreover, the resulting damping ratios are 0.6–0.8% lower compared to the one obtained for operation in master–slave control mode (Table 4.9). Thus, it was concluded that for constant wind production, the POD presents similar damping performance for both master–slave and compensated droop control modes.

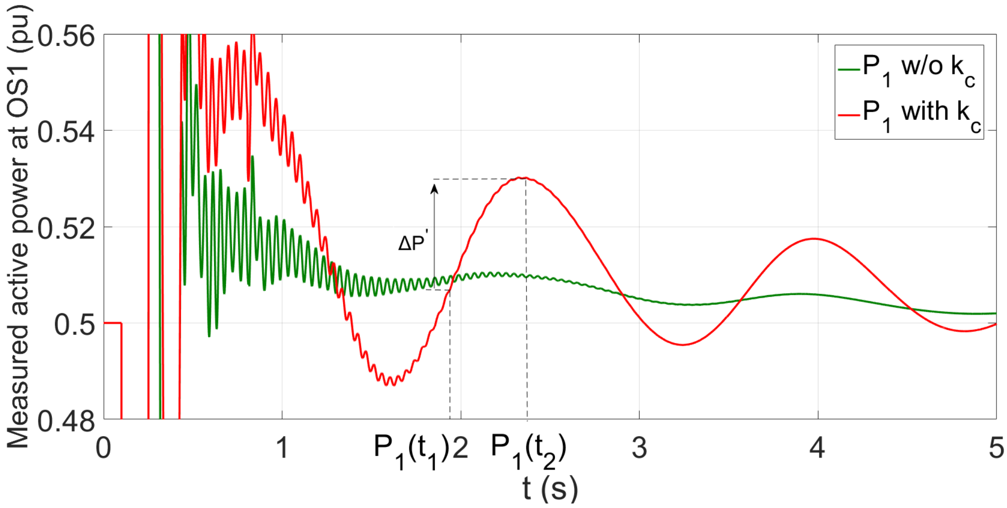

Figure 4.62. Measured active power at OS1 with and without the addition of k_c.

Table 4.15. Power oscillation damping ratio for five pairs of droop gain values when P_w=100 MW.

Cases under study	k_{dr1}	k_{dr2}	k_c	ΔP	$\Delta P'$	$\zeta(\%)$
Case C4	0.02	0.07	24.5	0.023	0.023	9.76
Case C3	0.05	0.1	11	0.023	0.023	9.86
Case C1	0.05	0.05	10.1	0.023	0.023	9.85
Case C2	0.1	0.05	5.6	0.023	0.023	10
Case C5	0.1	0.01	5.1	0.023	0.023	9.88

4.3.2.5 Compensation for the reduction in $\Delta P'$ for increasing wind power production

Regarding the case of the increasing wind power profile, the damping ratio values are repeated in Table 4.16, including the amounts of ΔP and $\Delta P'$:

Table 4.16. Power oscillation damping ratio for five pairs of droop gain values when the wind output ramps up from 20 to 400 MW.

Cases under study	k_{dr1}	k_{dr2}	ΔP	$\Delta P'$	$\zeta(\%)$
Case A4	0.02	0.07	0.033	0.014	4.11
Case A3	0.05	0.1	0.031	0.014	4.77
Case A1	0.05	0.05	0.027	0.09	5.06
Case A2	0.1	0.05	0.03	0.01	6.29
Case A5	0.1	0.01	0.031	0.008	8.18

The same procedure as before was followed with the aim of fully utilizing the output of the POD controller. Figures 4.63, 4.64 present the waveform of the POD output as well as the droop curve of MMC1 after the compensation for case A1. A choice of $k_c = 6.2$ leads to $\Delta P' = \Delta P = 0.023$ pu which is added to the active power at OS1 as Figure 4.65 depicts. The corresponding compensating gain value was found for each of the rest four cases and the results are given in Table 4.17. It can be seen that the addition of the compensating gain has positive effect on the damping ratio. However, compared to master–slave control, the POD controller performance is worse for operation in DC voltage droop control mode, even after the compensation, except case 5 in which k_{dr1} and k_{dr2} have their maximum and minimum values respectively.

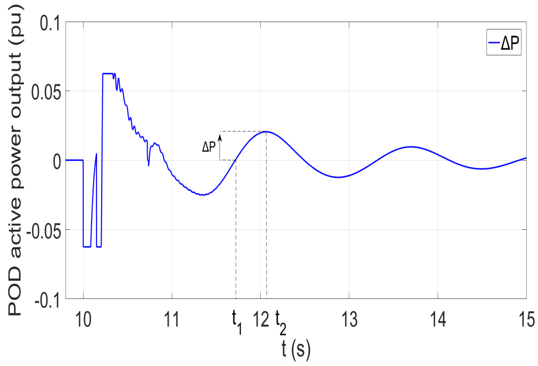

Figure 4.63. POD active power output for increasing wind power profile.

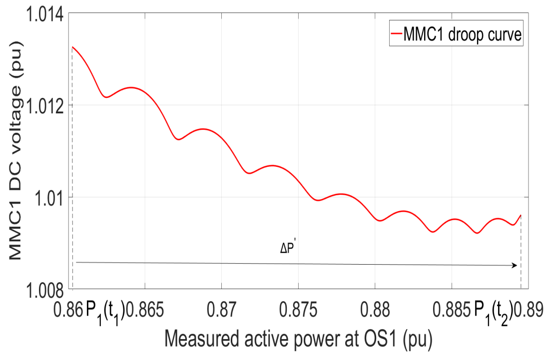

Figure 4.64. MMC1 droop curve for increasing wind power profile.

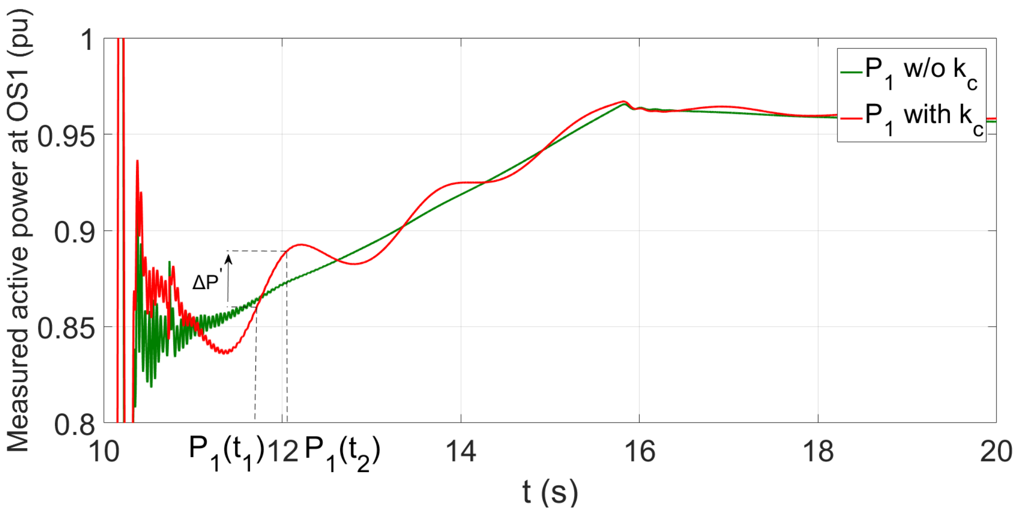

Figure 4.65. Measured active power at OS1 with and without the addition of k_c.

Table 4.17. Power oscillation damping ratio for five pairs of droop gain values when the wind output ramps up from 20 to 400 MW after compensation.

Cases under study	k_{dr1}	k_{dr2}	k_c	ΔP	$\Delta P'$	$\zeta(\%)$
Case A4	0.02	0.07	12.5	0.028	0.028	5.89
Case A3	0.05	0.1	6.2	0.028	0.028	6.45
Case A1	0.05	0.05	6.2	0.023	0.023	7.75
Case A2	0.1	0.05	4.2	0.025	0.025	8.95
Case A5	0.1	0.01	4.2	0.025	0.025	13.09

5 Conclusion

5.1 Summary of the main findings

In the context of this thesis, the focus was placed on the damping of the interarea oscillations which appear in power systems between groups of generators in one area swinging against a group of generators in another area. To this end, a simplified two–area test system was used to introduce such oscillations by applying a three–phase symmetrical fault. An HVDC link was utilized with the aim of damping them instead of making use of the conventional PSS units.

More specifically, a POD controller based on the structure of a PSS was applied in the converter controlling the active power, thus modifying its active power reference. This resulted in the direct control of active power flow over the DC link and, through this, the damping control provision on the inter-area mode. The controller was properly tuned with the use of the residue based method in order to provide adequate damping performance. It was shown that the addition of the POD controller can provide adequate damping for the two–area system connected with the PtP HVDC system (test system 2), since the damping ratio value was calculated equal to 33.2% for a choice of the damping gain $k_d = 0.25$, ensuring secure system operation.

Subsequently, the PtP system was expanded by the addition of a wind farm. In order to make its impact on the power oscillation damping capability more observable, a lower value for the POD gain was chosen, i.e. $k_d = 0.05$, resulting in a damping ratio equal to 9.93% for test system 2. For the three–terminal system, the system behaviour was examined with the two onshore converters initially operating in master–slave mode. Different wind power profiles were considered including constant, increasing and decreasing wind power output. By examining all three cases, it was shown that the designed POD controller was effective since it provided a damping ratio more than 10%. In addition, the damping of the electromechanical oscillations was shown to be improved for lower production from the traditional generators. A wind farm outage was also simulated, showing that sudden outage of the wind farm can potentially threaten the system stability since the damping ratio is decreased significantly for large loss of generated wind power.

Afterwards, the mode was switched to DC voltage droop control. The POD performance was tested for a constant and an increasing wind power profile by considering five different pairs of droop gains for each case. It was shown that as long as the droop gains of converters 1 and 2 are getting higher and lower respectively, the damping ratio is improved. More specifically, higher values of k_{dr1} make the droop curve steeper, resembling more to the constant active power control mode and thus utilizing larger amount of the POD output

ΔP. Additionally, lower values of k_{dr2} also lead to improved damping performance since in this case the active power flow through converter 2 is increased thus leading to decreased production from the traditional generators when MMC2 operates in inverter mode.

Compared to the master slave mode, lower damping ratio values were obtained for the droop control mode since only a part of the POD output is added to the active power of converter 1. To this end, the output of the POD controller was multiplied with a compensating gain k_c which was chosen appropriately for each pair of droop gains so that the utilization of ΔP is maximized. For constant wind power profile, the obtained damping ratio for operation in droop control mode was found to be 0.6 to 0.8% lower than in master slave–mode. Regarding the case of increasing wind power profile, the performance was still better for the master–slave control mode, with the difference in the POD damping capability between the two control modes becoming bigger.

5.2 Future work

Among the issues under investigation, the main ones are presented below:

- A more systematic way for the tuning of the POD controller in case of operation in DC voltage control mode can be investigated, depending on the droop gain relationship of the two converters.
- The POD performance can be assessed considering a ring topology for the MTDC system.
- A more realistic power system consisting of a bigger number of generators and buses can be modelled instead of the simplified two–area test system studied in this thesis. In such a system more aspects have to be taken into consideration, e.g. the proper choice of the input signal for the POD controller.
- POD controllers could be installed in both sides in case of operation in DC voltage control mode, offering the potential for improved damping performance.

PowerFactory data and modelling A

A.1 Parameters for the test systems

Within this section the parameters for the three test systems briefly described in Chapter 3 are given in detail in Tables A.1, A.2 and A.3.

Table A.1. Two–area test system parameters

Parameters	Symbol	Value
Generators of Area 1 and 2		
d–axis synchronous reactance	x_d	1.8 pu
q–axis synchronous reactance	x_q	1.7 pu
Stator leakage reactance	x_l	0.2 pu
d–axis transient reactance	$x_{d'}$	0.3 pu
q–axis transient reactance	$x_{q'}$	0.55 pu
d–axis subtransient reactance	$x_{d''}$	0.25 pu
Stator resistance	r_a	0.0025 pu
d–axis transient time constant	$T_{d,0'}$	8 s
q–axis transient time constant	$T_{q,0'}$	0.4 s
d–axis subtransient time constant	$T_{d,0''}$	0.03 s
q–axis subtransient time constant	$T_{q,0''}$	0.05 s
Inertia constant for G_1, G_2	H_1, H_2	6.5 s
Inertia constant for G_3, G_4	H_3, H_4	6.175 s
Damping torque coefficient	K_D	0 pu torque/pu speed deviation
Generator step–up transformers		
Rated power	S_r	900 MVA
Nominal frequency	f_n	50 Hz
Rated voltage on HV side	V_{rh}	230 kV
Rated voltage on LV side	V_{rl}	20 kV
Transmission system		
Nominal voltage	V_r	230 kV
Line resistance	r_{line}	0.0001 pu/km
Line reactance	$l_{L,line}$	0.001 pu/km
Line susceptance	$b_{C,line}$	0.001 75 pu/km
BUS 7 load	$P_{L,7}, Q_{L,7}$	967 MW, 100 MVAr
BUS 7 shunt capacitor	$Q_{C,7}$	200 MVAr
BUS 9 load	$P_{L,9}, Q_{L,9}$	1767 MW, 100 MVAr
BUS 9 shunt capacitor	$Q_{C,9}$	350 MVAr
Fault resistance	R_{fault}	0.1 Ohm
Power system stabilizers		
Stabilizer gain	k_{pss}	20 pu
Washout integrate time constant	T_W	10 s
Fisrt lead/lag derivative time constant	$T_{lead,1}$	0.05 s
Fisrt lead/lag delay time constant	$T_{lag,1}$	0.02 s
Second lead/lag derivative time constant	$T_{lead,2}$	3 s
Second lead/lag delay time constant	$T_{lag,2}$	5.4 s
AC excitation systems		
Exciter gain	k_a	200 pu
Speed governing systems		
Speed governing gain	k_g	15 pu

Table A.2. PtP HVDC test system parameters

Parameters	Symbol	Value
External grids		
Acceleration time constant	T_a	999 999 s
Short–circuit power	$S_{k''}$	10 000 MVA
Short–circuit current	$I_{k''}$	15.193 43 kA
c-factor	c	1.1
R/X ratio	R/X	0.1
Impedance ratio	X_0/X_1 R_0/X_0	1 0.1
Voltage setpoint	v_{sp}	1 pu
Reference angle	δ_{os}	0^o
Converter Transformers		
Rated power	S_r	450 MVA
Nominal frequency	f_n	50 Hz
Rated voltage on HV side	V_{rh}	380 kV
Rated voltage on LV side	V_{rl}	110 kV
Resistance (distributed at the LV side)	r_1	0.000 555 56 pu
Reactance (distributed at the LV side)	x_1	0.109 998 6 pu
Dummy Transformers		
Rated power	S_r	450 MVA
Nominal frequency	f_n	50 Hz
Rated voltage on HV side	V_{rh}	380 kV
Rated voltage on LV side	V_{rl}	230 kV
Resistance (equally distributed at both sides)	r_1	0 pu
Reactance (equally distributed at both sides)	x_1	0.001 pu
Modular multilevel converters		
Rated AC voltage	$V_{AC,r}$	110 kV
Rated DC voltage	$V_{DC,r}$	300 kV
Rated power	$S_{,r}$	450 MVA
Copper losses	P_{cu}	400 kW
No–load losses	P_{nl}	3000 kW
Arm resistance	R_{arm}	0.006 Ohm
Arm reactance	X_{arm}	60 mH
Submodule capacitance	C_{sm}	10 000 uF
Number of submodules per arm	n_a	200
DC cables		
Rated voltage	$V_{r,cable}$	150 kV
Rated current	$I_{r,cable}$	1.4 kA
Resistance	R_{cable}	0.01 Ohm/km
Inductance	L_{cable}	1.273 24 mH/km
Capacitance	C_{cable}	0.01 uF/km
Length	l_{cable}	100 km

Table A.3. Offshore terminal parameters

Parameters	Symbol	Value
Asynchronous Machine		
Rated apparent power	S_r	5.556 MVA
Rated mechanical power	$P_{m,r}$	4.87 MW
Rated power factor	pf_r	0.8952
Efficiency at nominal operation	n_r	97.9%
Nominal speed	$n_{rmp,r}$	1485.153 rpm
Number of pole pairs	2	–
Asynchronous Machine Transformer		
Rated power	S_r	5.6 MVA
Nominal frequency	f_n	50 Hz
Rated voltage on HV side	V_{rh}	33 kV
Rated voltage on LV side	V_{rl}	0.69 kV
Resistance (equally distributed at both sides)	r_1	0.001 pu
Reactance (equally distributed at both sides)	x_1	0.06 pu
Offshore Dummy Transformer		
Rated power	S_r	450 MVA
Nominal frequency	f_n	50 Hz
Rated voltage on HV side	V_{rh}	155 kV
Rated voltage on LV side	V_{rl}	33 kV
Resistance (equally distributed at both sides)	r_1	0 pu
Reactance (equally distributed at both sides)	x_1	0.001 pu
Offshore Modular multilevel converter		
Rated AC voltage	$V_{AC,r}$	155 kV
Rated DC voltage	$V_{DC,r}$	300 kV
Rated power	$S_{,r}$	450 MVA
Short–circuit impedance	Z_{sc}	10%
Copper losses	P_{cu}	400 kW
No–load losses	P_{nl}	3000 kW
Arm resistance	R_{arm}	0.006 Ohm
Arm reactance	X_{arm}	60 mH
Submodule capacitance	C_{sm}	10 000 uF
Number of submodules per arm	n_a	200
DC cables		
Rated voltage	$V_{r,cable}$	150 kV
Rated current	$I_{r,cable}$	1.4 kA
Resistance	R_{cable}	0.01 Ohm/km
Inductance	L_{cable}	1.273 24 mH/km
Capacitance	C_{cable}	0.01 uF/km
Length	l_{cable}	70 km

A.2 Wind farm ramp function

As it has already been mentioned, the wind farm was modelled with the use of 100 asynchronous machines (ASM) in parallel, aggregated into an ASM model. In order to create the different wind power output profiles, the mechanical input power of the asynchronous machines has to be controlled, thus controlling the electrical output power. The block Ramp function of Figure A.1 was implemented in order to output the suitable mechanical power "pt" (in pu) according to the desired output power profile.

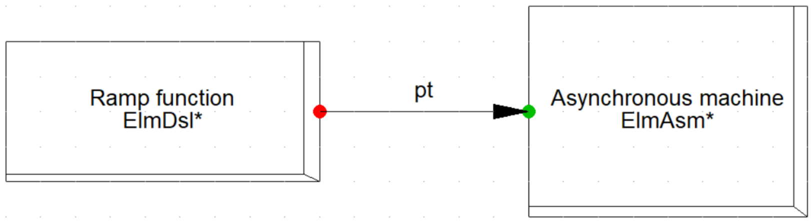

Figure A.1. Implemetation of the mechanical power control for each asynchronous machine in PowerFactory.

Figure A.2 presents the implementation of the ramp function which was done in a simple and straightforward way by using an integrator and modifying the value ot the parameter "slope" for each case . More specifically, in case that a constant wind power output profile is desired, the slope is set to zero. Thus the mechanical power stays constant with its value corresponding to the electrical power value that has been set in the Load Flow Options for each ASM. However,in order to create the increasing and decreasing power profiles, the slope has to be set at a nonzero value, i.e. a positive and negative value respectively.

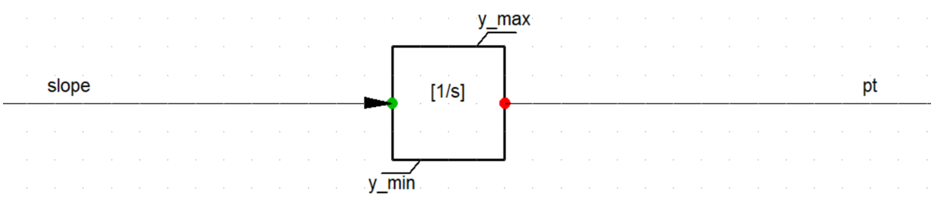

Figure A.2. Ramp function implementation in PowerFactory.

A.3 Offshore controller

Figure A.3 gives an overview of the controller structure for the offshore converter. The structure and the parameters of the "HVDC Connected Offshore Wind Farm" example of PowerFactory are used. The controller has to build the offshore grid voltage, thus it has to keep the frequency and the magnitude of this voltage constant. It takes as inputs the offshore terminal (OC at Figure 3.3) AC voltage and currents, the DC voltage of the positive and negative DC terminal and the q–component of the current i_q. The output of this controller is the modulation index $P_{m,in}$ and the frequency f_0 which are given as inputs to the offshore converter.

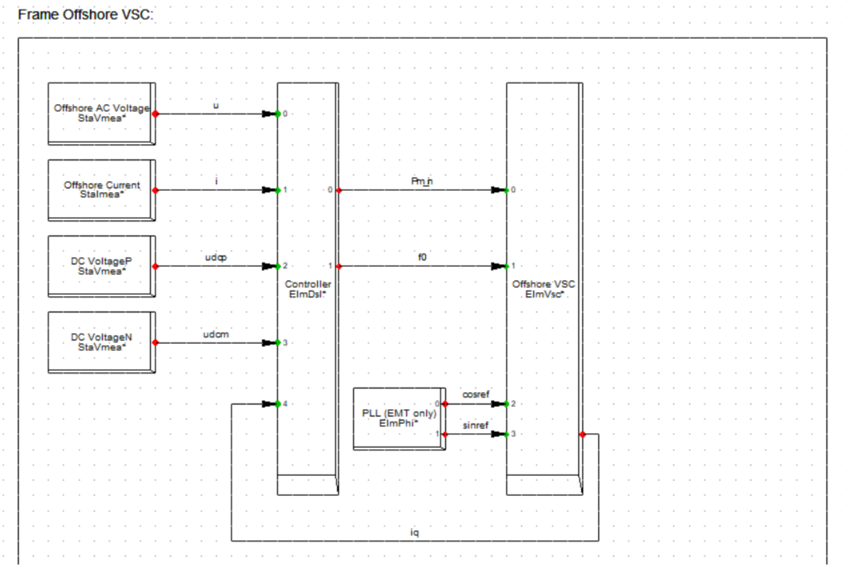

Figure A.3. Control block diagram of the offshore converter control.

As can be seen in Figure A.4, the modulation index is controlled with the use of two cascaded PIs and a feed forward path using the measured DC voltage. The AC voltage deviation is given as an input to the first PI controller which outputs the reactive current component reference. This is compared with the measured one and outputs the reference AC voltage which is divided with the measured DC voltage and multiplied with a constant based on the modulation method. The controller can also increase the frequency of the offshore network if the DC voltage rises, leading to the reduction of the active power produced by the wind farm. This function is disabled by default with the use of very high threshold values for the DC voltage. The chopper resistor keeps the DC voltage below the threshold values.

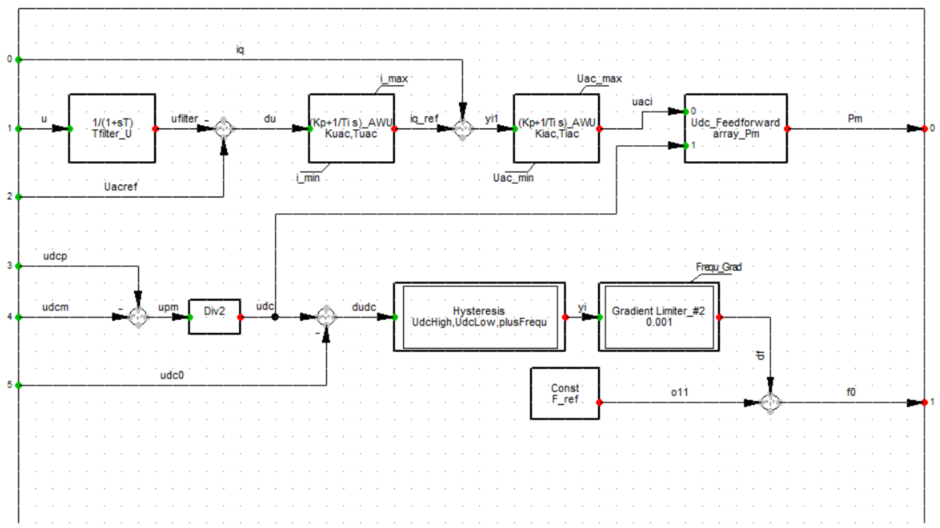

Figure A.4. Offshore controller structure.

Bibliography

[1] Y. Murata, M. Sakamaki, K. Abe, Y. Inoue, S. Mashio, S. Kashiyama, O. Matsunaga, T. Igi, M. Watanabe, S. Asai, and S. Katakai, "Development of high voltage dc-xlpe cable system," pp. 55–62, 04 2013.

[2] N. Ahmed, S. Norrga, H. P. Nee, A. Haider, D. V. Hertem, L. Zhang, and L. Harnefors, "Hvdc supergrids with modular multilevel converters x2014; the power transmission backbone of the future," in *International Multi-Conference on Systems, Sygnals Devices*, March 2012, pp. 1–7.

[3] B. Pal and B. Chaudhuri, *Robust Control in Power Systems*, ser. Power Electronics and Power Systems. Springer US, 2006. [Online]. Available: https://books.google.dk/books?id=UXh1o196-McC

[4] M. Klein, G. J. Rogers, and P. Kundur, "A fundamental study of inter-area oscillations in power systems," *IEEE Transactions on Power Systems*, vol. 6, no. 3, pp. 914–921, Aug 1991.

[5] M. Hadjikypris and V. Terzija, "Active power modulation assisting controller scheme implemented on a vsc-hvdc link establishing effective damping of low frequency power oscillations," in *2014 IEEE International Energy Conference (ENERGYCON)*, May 2014, pp. 295–302.

[6] R. Preece, A. M. Almutairi, O. Marjanovic, and J. V. Milanović, "Damping of inter-area oscillations using wams based supplementary controller installed at vsc based hvdc line," in *2011 IEEE Trondheim PowerTech*, June 2011, pp. 1–8.

[7] K. Lindén, J. Beerten, A. Alvarez, C. Barker, J. Hanson, R. Iravani, A. Isaacs, D. Jovcic, J. Peter Kjaergaard, J. Liang, L. Livermore, A.-K. Marten, M. Mohaddes, P. Rault, T. Vrana, D. Westermann, K. Würflinger, and Y. Yang, "Control methodologies for direct voltage and power flow in a meshed hvdc grid," pp. 72–75, 10 2017.

[8] R. Preece and J. V. Milanović, "Power oscillation damping using vsc-based multi-terminal hvdc grids," *IFAC Proceedings Volumes*, vol. 45, no. 21, pp. 20 – 25, 2012, 8th Power Plant and Power System Control Symposium. [Online]. Available: http://www.sciencedirect.com/science/article/pii/S1474667016319383

[9] R. Irnawan, F. F. da Silva, C. L. Bak, and T. C. Bregnhj, "Evaluation of half-bridge modular multilevel converter model for vsc-hvdc transient stability studies," in *13th IET International Conference on AC and DC Power Transmission (ACDC 2017)*, Feb 2017, pp. 1–6.

[10] K. Sharifabadi, L. Harnefors, H. Nee, S. Norrga, and R. Teodorescu, *Design, Control, and Application of Modular Multilevel Converters for HVDC Transmission*

Systems, ser. Wiley - IEEE. Wiley, 2016. [Online]. Available: https://books.google.dk/books?id=d57LDAAAQBAJ

[11] J. Arrillaga, Y. Liu, and N. Watson, *Flexible Power Transmission: The HVDC Options*. Wiley, 2007. [Online]. Available: https://books.google.dk/books?id=3LZ-284jCf4C

[12] R. E. Ramesh e and S. Harsha J, "Voltage source converter based hvdc transmission," vol. 1, pp. 97–106, 09 2012.

[13] R. Wachal, A. Jindal, S. Dennetiere, H. Saad, O. Rui, S. Cole, M. Barnes, L. Zhang, Z. Song, J. Jardini, J. Carlos Garcia, F. Mosallat, H. Suriyaarachich, P. Le-Huy, A. Totterdell, L. Zeni, S. Kodsi, T. Deepak, P. Thepparat, and Y. Yang, "Guide for the development of models for hvdc converters in a hvdc grid," 12 2014.

[14] V. Sood and H. Patel, "Comparison between direct and vector control strategy for vsc-hvdc system in emtp-rv," in *2010 Joint International Conference on Power Electronics, Drives and Energy Systems 2010 Power India*, Dec 2010, pp. 1–6.

[15] T. M. Haileselassie, "Control of multi--terminal vsc--hvdc systems",master thesis, department of electrical power engineering, norwegian university of science and technology," 2008.

[16] T. W. Shire, "Vsc-hvdc based network reinforcement," 2009.

[17] D. GmbH, "Technical reference documentation–pwm converter, digsilent gmbh," 2017.

[18] ——, "Technical reference documentation–phase measurement device, digsilent gmbh," 2017.

[19] ——, "User manual,digsilent gmbh," 2017.

[20] C. Bajracharya, M. Molinas, J. Suul, and T. M. Undeland, "Understanding of tuning techniques of converter controllers for vsc-hvdc," 06 2008.

[21] L. Harnefors and H. P. Nee, "Model-based current control of ac machines using the internal model control method," *IEEE Transactions on Industry Applications*, vol. 34, no. 1, pp. 133–141, Jan 1998.

[22] P. Kundur, N. Balu, and M. Lauby, *Power system stability and control*, ser. EPRI power system engineering series. McGraw-Hill, 1994. [Online]. Available: https://books.google.dk/books?id=wOlSAAAAMAAJ

[23] W. Mansour, M. Mandour, M. EL-Shimy, and F. Bendary, "Impact of wind power on power system stability and oscillation damping controller design," 04 2015.